

**Control of
Antenna Radiation Characteristics by
Ground Plane Size and Shape**

by

Sima Noghanian

A Thesis
Submitted to the Faculty of Graduate Studies
in Partial Fulfilment of the Requirements
for the Degree of

MASTER OF SCIENCE

Department of Electrical and Computer Engineering
University of Manitoba
Winnipeg, Manitoba

© August, 1996



National Library
of Canada

Acquisitions and
Bibliographic Services Branch

395 Wellington Street
Ottawa, Ontario
K1A 0N4

Bibliothèque nationale
du Canada

Direction des acquisitions et
des services bibliographiques

395, rue Wellington
Ottawa (Ontario)
K1A 0N4

Your file *Votre référence*

Our file *Notre référence*

The author has granted an irrevocable non-exclusive licence allowing the National Library of Canada to reproduce, loan, distribute or sell copies of his/her thesis by any means and in any form or format, making this thesis available to interested persons.

L'auteur a accordé une licence irrévocable et non exclusive permettant à la Bibliothèque nationale du Canada de reproduire, prêter, distribuer ou vendre des copies de sa thèse de quelque manière et sous quelque forme que ce soit pour mettre des exemplaires de cette thèse à la disposition des personnes intéressées.

The author retains ownership of the copyright in his/her thesis. Neither the thesis nor substantial extracts from it may be printed or otherwise reproduced without his/her permission.

L'auteur conserve la propriété du droit d'auteur qui protège sa thèse. Ni la thèse ni des extraits substantiels de celle-ci ne doivent être imprimés ou autrement reproduits sans son autorisation.

ISBN 0-612-16222-2

Canada

Name _____

Dissertation Abstracts International and *Masters Abstracts International* are arranged by broad, general subject categories. Please select the one subject which most nearly describes the content of your dissertation or thesis. Enter the corresponding four-digit code in the spaces provided.

Electronics and Electrical Engineering

SUBJECT TERM

0544

UMI

SUBJECT CODE

Subject Categories

THE HUMANITIES AND SOCIAL SCIENCES

COMMUNICATIONS AND THE ARTS

Architecture 0729
Art History 0377
Cinema 0900
Dance 0378
Fine Arts 0357
Information Science 0723
Journalism 0391
Library Science 0399
Mass Communications 0708
Music 0413
Speech Communication 0459
Theater 0465

EDUCATION

General 0515
Administration 0514
Adult and Continuing 0516
Agricultural 0517
Art 0273
Bilingual and Multicultural 0282
Business 0688
Community College 0275
Curriculum and Instruction 0727
Early Childhood 0518
Elementary 0524
Finance 0277
Guidance and Counseling 0519
Health 0680
Higher 0745
History of 0520
Home Economics 0278
Industrial 0521
Language and Literature 0279
Mathematics 0280
Music 0522
Philosophy of 0998
Physical 0523

Psychology 0525
Reading 0535
Religious 0527
Sciences 0714
Secondary 0533
Social Sciences 0534
Sociology of 0340
Special 0529
Teacher Training 0530
Technology 0710
Tests and Measurements 0288
Vocational 0747

LANGUAGE, LITERATURE AND LINGUISTICS

Language
General 0679
Ancient 0289
Linguistics 0290
Modern 0291
Literature
General 0401
Classical 0294
Comparative 0295
Medieval 0297
Modern 0298
African 0316
American 0591
Asian 0305
Canadian (English) 0352
Canadian (French) 0355
English 0593
Germanic 0311
Latin American 0312
Middle Eastern 0315
Romance 0313
Slavic and East European 0314

PHILOSOPHY, RELIGION AND THEOLOGY

Philosophy 0422
Religion
General 0318
Biblical Studies 0321
Clergy 0319
History of 0320
Philosophy of 0322
Theology 0469

SOCIAL SCIENCES

American Studies 0323
Anthropology
Archaeology 0324
Cultural 0326
Physical 0327
Business Administration
General 0310
Accounting 0272
Banking 0770
Management 0454
Marketing 0338
Canadian Studies 0385
Economics
General 0501
Agricultural 0503
Commerce-Business 0505
Finance 0508
History 0509
Labor 0510
Theory 0511
Folklore 0358
Geography 0366
Gerontology 0351
History
General 0578

Ancient 0579
Medieval 0581
Modern 0582
Black 0328
African 0331
Asia, Australia and Oceania 0332
Canadian 0334
European 0335
Latin American 0336
Middle Eastern 0333
United States 0337
History of Science 0585
Law 0398
Political Science
General 0615
International Law and Relations 0616
Public Administration 0617
Recreation 0814
Social Work 0452
Sociology
General 0626
Criminology and Penology 0627
Demography 0938
Ethnic and Racial Studies 0631
Individual and Family Studies 0628
Industrial and Labor Relations 0629
Public and Social Welfare 0630
Social Structure and Development 0700
Theory and Methods 0344
Transportation 0709
Urban and Regional Planning 0999
Women's Studies 0453

THE SCIENCES AND ENGINEERING

BIOLOGICAL SCIENCES

Agriculture
General 0473
Agronomy 0285
Animal Culture and Nutrition 0475
Animal Pathology 0476
Food Science and Technology 0359
Forestry and Wildlife 0478
Plant Culture 0479
Plant Pathology 0480
Plant Physiology 0817
Range Management 0777
Wood Technology 0746
Biology
General 0306
Anatomy 0287
Biostatistics 0308
Botany 0309
Cell 0379
Ecology 0329
Entomology 0353
Genetics 0369
Limnology 0793
Microbiology 0410
Molecular 0307
Neuroscience 0317
Oceanography 0416
Physiology 0433
Radiation 0821
Veterinary Science 0778
Zoology 0472
Biophysics
General 0786
Medical 0760

EARTH SCIENCES

Biogeochemistry 0425
Geochemistry 0996

Geodesy 0370
Geology 0372
Geophysics 0373
Hydrology 0388
Mineralogy 0411
Paleobotany 0345
Paleoecology 0426
Paleontology 0418
Paleozoology 0985
Palynology 0427
Physical Geography 0368
Physical Oceanography 0415

HEALTH AND ENVIRONMENTAL SCIENCES

Environmental Sciences 0768
Health Sciences
General 0566
Audiology 0300
Chemotherapy 0992
Dentistry 0567
Education 0350
Hospital Management 0769
Human Development 0758
Immunology 0982
Medicine and Surgery 0564
Mental Health 0347
Nursing 0569
Nutrition 0570
Obstetrics and Gynecology 0380
Occupational Health and Therapy 0354
Ophthalmology 0381
Pathology 0571
Pharmacology 0419
Pharmacy 0572
Physical Therapy 0382
Public Health 0573
Radiology 0574
Recreation 0575

Speech Pathology 0460
Toxicology 0383
Home Economics 0386

PHYSICAL SCIENCES

Pure Sciences
Chemistry
General 0485
Agricultural 0749
Analytical 0486
Biochemistry 0487
Inorganic 0488
Nuclear 0738
Organic 0490
Pharmaceutical 0491
Physical 0494
Polymer 0495
Radiation 0754
Mathematics 0405
Physics
General 0605
Acoustics 0986
Astronomy and Astrophysics 0606
Atmospheric Science 0608
Atomic 0748
Electronics and Electricity 0607
Elementary Particles and High Energy 0798
Fluid and Plasma 0759
Molecular 0609
Nuclear 0610
Optics 0752
Radiation 0756
Solid State 0611
Statistics 0463
Applied Sciences
Applied Mechanics 0346
Computer Science 0984

Engineering
General 0537
Aerospace 0538
Agricultural 0539
Automotive 0540
Biomedical 0541
Chemical 0542
Civil 0543
Electronics and Electrical 0544
Heat and Thermodynamics 0348
Hydraulic 0545
Industrial 0546
Marine 0547
Materials Science 0794
Mechanical 0548
Metallurgy 0743
Mining 0551
Nuclear 0552
Packaging 0549
Petroleum 0765
Sanitary and Municipal 0554
System Science 0790
Geotechnology 0428
Operations Research 0796
Plastics Technology 0795
Textile Technology 0994

PSYCHOLOGY

General 0621
Behavioral 0384
Clinical 0622
Developmental 0620
Experimental 0623
Industrial 0624
Personality 0625
Physiological 0989
Psychobiology 0349
Psychometrics 0632
Social 0451

**THE UNIVERSITY OF MANITOBA
FACULTY OF GRADUATE STUDIES
COPYRIGHT PERMISSION**

**CONTROL OF ANTENNA RADIATION CHARACTERISTICS BY
GROUND PLANE SIZE AND SHAPE**

BY

SIMA NOGHANIAN

**A Thesis/Practicum submitted to the Faculty of Graduate Studies of the University of Manitoba in partial
fulfillment of the requirements for the degree of**

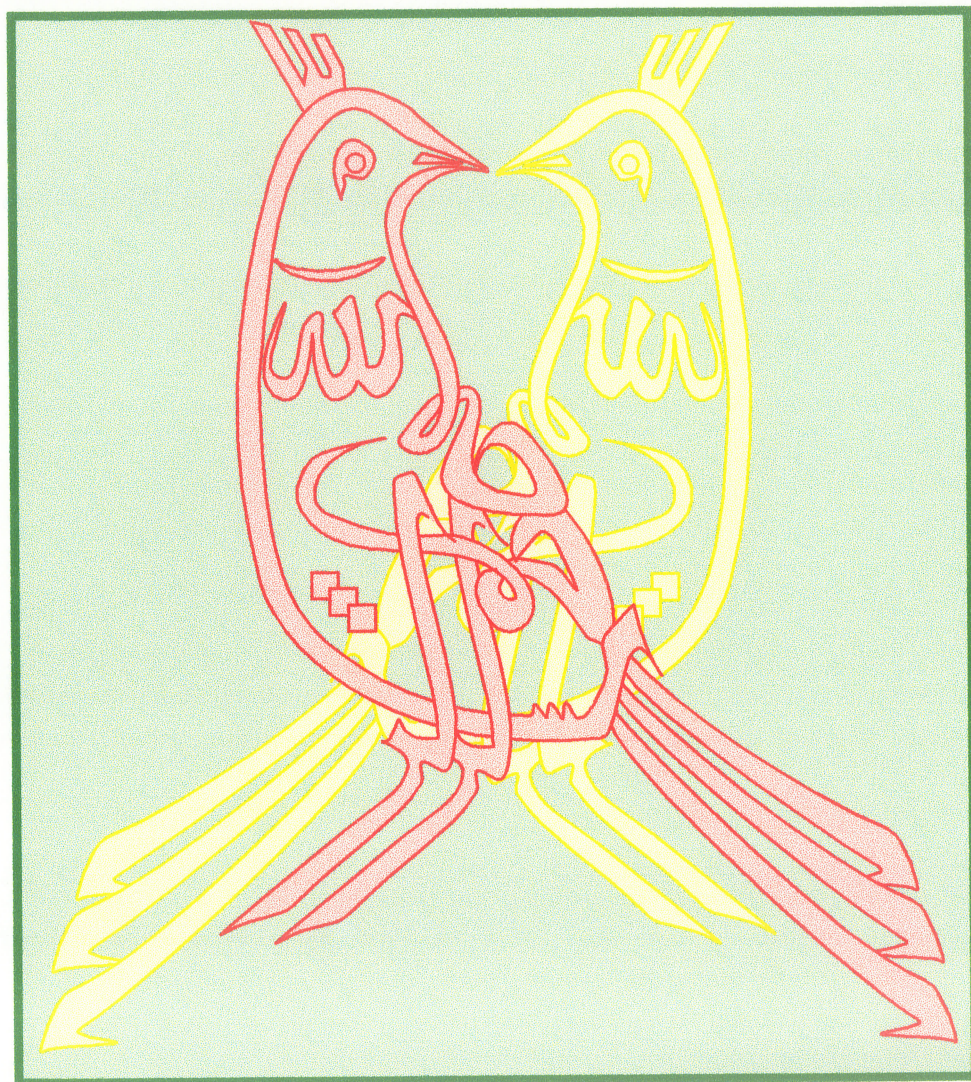
MASTER OF SCIENCE

Sima Noghanian

© 1996

**Permission has been granted to the LIBRARY OF THE UNIVERSITY OF MANITOBA to lend or sell copies
of this thesis/practicum, to the NATIONAL LIBRARY OF CANADA to microfilm this thesis/practicum and
to lend or sell copies of the film, and to UNIVERSITY MICROFILMS INC. to publish an abstract of this
thesis/practicum..**

**This reproduction or copy of this thesis has been made available by authority of the copyright owner solely
for the purpose of private study and research, and may only be reproduced and copied as permitted by
copyright laws or with express written authorization from the copyright owner.**



Abstract

The effects of various physical and electrical parameters of circular microstrip antennas on their radiation characteristics are investigated. These parameters include the ground plane size, substrate permittivity, ground plane and substrate thicknesses and ground plane shape. The first four modes were studied. A numerical method based on the method of moment was utilized. To avoid excessive computation, circular patch was chosen which allows the use of the moment method for Bodies of Revolution. Experimental results showed good agreement with simulation results.

It was found that the gain can be controlled mostly by the ground plane radius. In fact the gain is more affected by the ground plane radius than the substrate permittivity. Also the ground plane shape can be modified to shape the radiation patterns. The other antenna dimensions such as the ground plane thickness and substrate thickness also have important effects on the antenna performance. By choosing the right sizes, better gain and circular polarization can be achieved.

A preliminary study on the radiation characteristics of dielectric resonator antennas was carried out. The antennas with large dielectric resonator height, in comparison to its radius, show good performance, which can be a subject of future study.

Acknowledgements

I wish to express my sincere appreciation and gratitude to professor L. Shafai for his wise supervision, valuable guidance, patience and advice. His encouragement, kindness and moral support have been a continual source of inspiration. Indeed, my gratitude to him can not be expressed in a few words.

Special thanks to Mr. B. Tabachnick, who patiently performed experimental measurements. The financial support provided by the National Science and Engineering Research Council of Canada, through a grant to professor L. Shafai is also gratefully acknowledged.

Extended thanks to my family, especially my mother for her patience and sacrifice during my educational life. I wish to express my deep appreciation and indebtedness to my best friend, my husband, for his kindness, encouragement and support. This work is dedicated to him.

I am also indebted to my beloved motherland, Iran, and her loving people. Finally and most of all, I am grateful to Almighty God, who guided me to the best way of life.

Table of Contents

Abstract	i
Acknowledgements	ii
Table of Contents	iii
List of Figures	vi
List of Tables	x
Chapter 1 Introduction	1
1.1. Preface.....	2
1.2. Background.....	3
1.3. Objective of This Study	4
1.4. Simulation Tool.....	5
Chapter 2 Microstrip Antenna Overview	6
2.1. Introduction.....	7
2.2. Microstrip Antenna Structure	7
2.3. Analytical Method: the Simple Cavity Model.....	11
2.3.1. Fields.....	13
2.3.2. Far Fields	14
2.3.3. Resonant Frequency.....	16
2.4. Numerical Method: Method of Moments	17
2.4.1. Bodies of Revolution	20

Chapter 3 Effects of the Ground Plane Radius 24

3.1. Introduction.....	25
3.2. Simulation Method	27
3.2.1. Antenna Geometry	27
3.2.2. Excitation	28
3.2.3. Gain Calculation	28
3.3. Effects on the Gain.....	29
3.3.1. Simulation Results	29
3.3.2. Experimental Results	36
3.4. Effects on the Radiation Pattern	38
3.4.1. TM_{11} Mode	38
3.4.2. TM_{21} Mode	39
3.4.3. TM_{31} Mode	47
3.4.4. TM_{41} Mode	51
3.4.5. Experimental Results	55
3.5. Effects on Circular Polarization.....	58
3.5.1. Axial Ratio and Polarization Ratio	58
3.5.2. Simulation Results	61
3.6. Summary	66

Chapter 4 Effects of the Ground Plane Shape 67

4.1. Introduction.....	68
4.2. Cavity Antenna	68
4.3. Shaping the Ground Plane	78
4.4. Summary	83

Chapter 5 Effects of the Ground Plane and Substrate Thicknesses 84

5.1. Introduction.....	85
5.2. Effects on the Gain.....	85

5.3. Effects on the Radiation Patterns	88
5.4. Effects on Circular Polarization	96
5.5. Summary	100
Chapter 6 Effects of Finite Ground Plane on the Dielectric Resonator	
Antenna	101
6.1. Introduction	102
6.2. Dielectric Resonator Antenna Structure	103
6.3. Analytical Method	105
6.4. Numerical Method	108
6.5. Simulatoin Results	109
6.6. Summary	118
Chapter 7 Conclusion	119
7.1. Summary	120
7.2. Future Work	122
Appendix A Patch Size Calculation	123
Appendix B Gain and Axial Ratio Calculation	125
Appendix C Dielectric Resonator Antenna Radiation Pattern Calculation	131
References	142

List of Figures

Fig. 2.1	Circular microstrip patch antenna.....	8
Fig. 2.2	Some configurations of often used microstrip patches	8
Fig. 2.3	Radiation mechanism of a rectangular microstrip antenna.....	10
Fig. 2.4	Cavity model of microstrip antenna.....	12
Fig. 2.5	Bessel functions of order 0-4	14
Fig. 2.6	Coordinate and aperture surface for calculating far fields	15
Fig. 2.7	The general form of problem	17
Fig. 2.8	Geometry of body of revolution	21
Fig. 3.1	Effect of the ground plane radius on the radiation patterns of TM_{11} mode.....	25
Fig. 3.2	Effect of the ground plane radius on the radiation patterns of TM_{21} mode.....	26
Fig. 3.3	Circular microstrip patch antenna with finite ground plane.....	27
Fig. 3.4	Gain variation for TM_{11} mode	30
Fig. 3.5	Gain variation for TM_{21} mode	30
Fig. 3.6	Gain variation for TM_{31} mode	31
Fig. 3.7	Gain variation for TM_{41} mode.....	31
Fig. 3.8	Local maximum for TM_{31} mode (for $\epsilon_r=2.5$)	35
Fig. 3.9	Local maximum for TM_{41} mode (for $\epsilon_r=4.0$)	35
Fig. 3.10	Return loss measurement	37
Fig. 3.11	Comparison between simulation and experimental results for directivity	38
Fig. 3.12	Radiation patterns for TM_{11} mode, $\epsilon_r=2.5$	40
Fig. 3.13	Angle for antenna peak gain for TM_{11} mode.....	41
Fig. 3.14	Half power beamwidth for TM_{11} mode	42
Fig. 3.15	Backlobe level for TM_{11} mode	43
Fig. 3.16	E and H-plane patterns peak difference for TM_{11} mode	43
Fig. 3.17	Radiation patterns for TM_{21} mode, $\epsilon_r=4.0$	44
Fig. 3.18	Angle for antenna peak gain for TM_{21} mode	45

Fig. 3.19	Half power beamwidth for TM_{21} mode	46
Fig. 3.20	E and H-plane patterns peak difference for TM_{21} mode	47
Fig. 3.21	Radiation patterns for TM_{31} mode, $\epsilon_r=6.0$	48
Fig. 3.22	Angle for antenna peak gain for TM_{31} mode	49
Fig. 3.23	Half power beamwidth for TM_{31} mode	50
Fig. 3.24	E and H-plane patterns peak difference for TM_{31} mode	51
Fig. 3.25	Radiation patterns for TM_{41} mode, $\epsilon_r=2.5$	52
Fig. 3.26	Angle for antenna peak gain for TM_{41} mode	53
Fig. 3.27	Half power beamwidth for TM_{41} mode	54
Fig. 3.28	E and H-plane patterns peak difference for TM_{41} mode	55
Fig. 3.29	Radiation pattern measurement for $g=0.6\lambda_0$	56
Fig. 3.30	Radiating pattern measurement for $g=1.1\lambda_0$	57
Fig. 3.31	Polarization ellipse	59
Fig. 3.32	Relationship between axial ratio and polarization ratio	60
Fig. 3.33	Axial ratio for TM_{11} mode, $\epsilon_r=2.5$	62
Fig. 3.34	Axial ratio for TM_{11} mode, $\epsilon_r=4.0$	62
Fig. 3.35	Axial ratio for TM_{11} mode, $\epsilon_r=6.0$	63
Fig. 3.36	Axial ratio for TM_{21} mode, $\epsilon_r=2.5$	63
Fig. 3.37	Axial ratio for TM_{21} mode, $\epsilon_r=4.0$	64
Fig. 3.38	Axial ratio for TM_{21} mode, $\epsilon_r=6.0$	64
Fig. 3.39	Axial ratio for TM_{31} mode, $\epsilon_r=2.5$	65
Fig. 3.40	Axial ratio for TM_{41} mode, $\epsilon_r=2.5$	65
Fig. 4.1	Geometry of microstrip antenna with cavity shape ground plane	68
Fig. 4.2	Radiation patterns for antennas with $g=0.4\lambda_0$, rim dimensions are $r=0.4\lambda_0$, $d=0.02\lambda_0$	69
Fig. 4.3	Radiation patterns for antennas with $g=0.6\lambda_0$, rim dimensions are $r=0.4\lambda_0$, $d=0.1\lambda_0$	70
Fig. 4.4	Gain variation for antennas with cavity shape ground plane	70
Fig. 4.5	Radiation patterns for antenna with $g=0.6\lambda_0$, $r=0.4\lambda_0$, and $d=0.02\lambda_0$	72
Fig. 4.6	Radiation patterns for antenna with $g=0.6\lambda_0$, $r=0.4\lambda_0$, and $d=0.10\lambda_0$	

72
Fig. 4.7	Configuration of antenna with chock.....73
Fig. 4.8	Radiation patterns for antenna with chock, $g=0.6\lambda_0$, $r=0.4\lambda_0$, and $d=0.10\lambda_0$74
Fig. 4.9	E-plane beamwidth75
Fig. 4.10	H-plane beamwidth.....75
Fig. 4.11	Backlobe level.....76
Fig. 4.12	Axial ratio for $g=0.4\lambda_0$, $d=0.05\lambda_0$76
Fig. 4.13	Axial ratio for $g=0.6\lambda_0$, $d=0.05\lambda_0$77
Fig. 4.14	Axial ratio for $g=0.8\lambda_0$, $d=0.05\lambda_0$77
Fig. 4.15	Microstrip antenna with shaped ground plane, ($h=0.04\lambda_0$)78
Fig. 4.16	Radiation pattern variations for the antennas shown in Figs. 4.15-b to 4.15-d80
Fig. 4.17	Radiation pattern variations for the antennas shown in Figs.4.15-d to 4.15-f.....81
Fig. 4.18	Radiation pattern variations for the antennas shown in Figs.4.15-f and 4.15-g82
Fig. 4.19	Radiation patterns for the antenna shown in Fig. 4.15-g83
Fig. 5.1	Antennas gain.....87
Fig. 5.2	E-plane half power beamwidth91
Fig. 5.3	H-plane half power beamwidth.....92
Fig. 5.4	E and H-plane peak difference93
Fig. 5.5	Backlobe level.....94
Fig. 5.6	Radiation patterns for an antenna with $g=0.25\lambda_0$ and $h=0.06\lambda_0$95
Fig. 5.7	Axial ratio for $g=0.18\lambda_0$97
Fig. 5.8	Axial ratio for $g=0.20\lambda_0$98
Fig. 5.9	Axial ratio for $g=0.25\lambda_0$99
Fig. 6.1	Cylindrical dielectric resonator antenna geometry104
Fig. 6.2	Radiation patterns for the antenna with $a/d=1.67$, $\epsilon_r=8.9$, TM_{110} mode110
Fig. 6.3	Radiation patterns for the antenna with $a/d=0.5$, $\epsilon_r=8.9$, TM_{110} mode ...

	110
Fig. 6.4	Radiation patterns for the antenna with $a/d=0.3$, $\epsilon_r=8.9$, TM_{110} mode	111
Fig. 6.5	Radiation patterns for the antenna with $a/d=0.15$, $\epsilon_r=8.9$, TM_{110} mode	111
Fig. 6.6	Variation of the gain for dielectric resonator antennas	112
Fig. 6.7	Backlobe level variation with the ground plane radius.....	113
Fig. 6.8	E-plane half power beamwidth	114
Fig. 6.9	H-plane half power beamwidth.....	114
Fig. 6.10	E and H-plane patterns peak difference	115
Fig. 6.11	Axial ratio for the antennas with $g=0.3\lambda_0$	116
Fig. 6.12	Axial ratio for the antennas with $g=1.1\lambda_0$	116
Fig. 6.13	Radiation patterns for the antennas with $g=0.3\lambda_0$	117
Fig. 6.14	Radiation patterns for the antennas with $g=1.1\lambda_0$	117
Fig. 6.15	Axial ratio for $a/d=0.5$, $g=0.3\lambda_0$ and different ground plane thicknesses	118

List of Tables

Table (2-1)	Zeros of derivative of Bessel functions	14
Table (3-1)	Gain of TM ₁₁ mode with finite and infinite ground planes.....	25
Table (3-2)	Gain for TM ₂₁ mode with finite and infinite ground planes	26
Table (3-3)	Patch radius (a)/ λ_0 for $h=0.01\lambda_0$	27
Table (3-4)	Ratio of feed location to patch size (ρ_f/a) for different modes ...	28
Table (3-5)	Gain for TM ₁₁ mode (dBi).....	32
Table (3-6)	Gain for TM ₂₁ mode (dBi).....	32
Table (3-7)	Gain for TM ₃₁ mode (dBi).....	33
Table (3-8)	Gain for TM ₄₁ mode (dBi).....	33
Table (3-9)	Minimum and optimum ground plane radii	34
Table (3-10)	Antenna parameters	36
Table (3-11)	Experimental and simulation results for gain measurement	37
Table (3-12)	Representation of polarization states	59
Table (4-1)	Maximum gain improvement in terms of ground plane radius...	71
Table (4-2)	Variation of axial ratio with rim dimensions.....	74
Table (4-3)	Radiation pattern parameters for the antennas shown in Fig. 4.15	79
Table (5-1)	Patch sizes for TM ₁₁ mode and $\epsilon_r=2.5$	85
Table (5-2)	Gain variation with ground plane and substrate thicknesses (dBi).	86
Table (5-3)	Ground plane thicknesses which maximize the gain	86
Table (5-4)	Radiation pattern parameters	88
Table (5-5)	Variation of radiation pattern parameters with ground plane and substrate thicknesses	90
Table (6-1)	Antenna dimensions for TM ₁₁₀ mode, $\epsilon_t=8.9$, $t=0.1\lambda_0$ and $g=3.01\lambda_0$	109
Table (6-2)	Antenna dimensions for TM ₁₁₀ mode, $\epsilon_t=4.5$ and $t=0.01\lambda_0$	112

Chapter 1

Introduction

1.1. Preface	2
1.2. Background.....	3
1.3. Objective of This Study	4
1.4. Simulation Tool.....	5

1.1. Preface

The invention of microstrip antennas goes back to early 1950's [1]. Twenty years later the first practical development experiments of microstrip antennas were done [2] [3]. Because of their many advantages such as light weight, low cost, thin profile, simple geometry, compatibility with integrated circuits and conformability in mounting on the host body, they have become one of the most popular antenna types.

These advantages have led to various types of applications. Some notable applications are satellite communication, mobile radio, radar, missile telemetry, biomedical radiators and reflector feeds. Due to the growing demand for these antennas, a great deal of efforts have been made to reduce their disadvantages, namely narrow bandwidth, high loss, and practical gain limit. However, in spite of these innovations and progresses, the demand for lower-cost, less-weight and lower-profile antennas is increasing. This, in turns, means that more precise mathematical models which can predict the innovative structures and consider practical aspects, are needed.

One of the important parameters of microstrip antennas which has been neglected in most investigations is the finite ground plane size. For practical applications having an infinite ground plane is impossible, and besides the ground plane parameters such as its dimensions and shape can be used to achieve a better performance.

This study is an attempt to investigate the effects of various geometrical parameters of the ground plane of microstrip antenna on its radiation characteristics. A numerical method based on the moment method is utilized and for the sake of simplicity a circular configuration is selected.

1.2. Background

The circular microstrip antennas have been investigated extensively. Various methods for the analysis of a disk antenna are available [4], but most of them are based on the assumption of infinite ground plane. In the past decade, however, some research has been done to investigate the effects of finite ground plane size on the performance of these antennas.

Huang [5] used the uniform geometrical theory of diffraction (GTD) for calculation of the edge diffracted field from the ground plane of rectangular microstrip antennas. He used the slot theory and modal expansion to approximate the incident field and GTD to approximate the radiated field. The slot theory can only be employed for rectangular patch and copolar calculation. The combination of GTD and other theories such as modal expansion theory can be used for other shapes of microstrip patch antennas. This method is not applicable when the product of substrate thickness (in wavelength) and dielectric constant is much greater than 0.1. Also it is required that the distance between ground plane edge and the edge of radiating patch be more than a quarter wavelength.

Barroso and Giarola [6] studied the effect of truncation of dielectric layer of a circular microstrip antenna, using the cavity model with magnetic side walls. They assumed that the ground plane is infinite and the position of truncation of dielectric occurs in the far field region.

Kishk and Shafai [7] used the method of moment to predict the effect of finite ground plane, substrate thickness and substrate permittivity on the radiation pattern. They showed that the ground plane size can be used to improve the pattern symmetry. It was the first time that higher order modes were also studied.

Recently, Bhattacharyya introduced an analytical technique to determine the effect of finite

ground plane on the radiation characteristics [8], efficiency [9] and impedance [10]. His work is based on the determination of currents on the ground plane and on the upper surface of the patch. He obtained the fields by using the cavity model. Then he used these fields to calculate equivalent electric and magnetic current sources on the aperture. Because he limited his analysis to a thin dielectric layer, he neglected the contribution of electric current source to the near field. The other assumption he made was the validity of image theory for near fields.

Finally, Vaudon et al. [11] [12] proposed an asymptotic method for predication of the E and H-plane radiation patterns of rectangular microstrip antennas with finite ground planes. Their theoretical study is made in two dimensions, but the physical problem is in three dimensions. This method is simple for computation, but does not offer improved accuracy over the previously mentioned methods. In fact, its accuracy decreases rapidly for off axis angles $\theta > 60^\circ$ and is limited to small ground plane sizes. They also considered the application of finite ground planes to the design of circularly polarized antennas.

1.3. Objective of This Study

The purpose of this research is to investigate the effects of physical and electrical parameters of microstrip antennas and their radiation characteristics. A moment method is used for this study that computes the surface field distribution and currents accurately and without any approximations. The method, however, is inefficient and regains excessive computer time and memory. To improve the efficiency, circular microstrip antennas are investigated, where the moment method of Bodies of Revolution can be used. In this method, the unknown currents are expanded in terms of Fourier series of the azimuthal coordinates, which represent the physical modes of a circular microstrip antenna. Since microstrip antennas are highly resonant structures, in practice, only a

small number of modes need to be considered. A numerical investigation of circular microstrip antennas then becomes quite efficient.

Kishk and Shafai [7] have shown that by a proper selection of the antenna parameters, radiation patterns with nearly equal E and H-plane patterns can be obtained that provide circularly polarized patch antennas with extremely low axial ratios. In this study, in addition to investigation of circular polarization, the use of the antenna parameters to optimize the gain and control the far field patterns are investigated for the first four modes. To confirm the numerical results, adequate experiments are also conducted and compared. Since all antenna losses are neglected, the gain values provided in this study represents the antenna directivity.

1.4.Simulation Tool

All the simulations in this study are performed using “Multi Body Electromagnetic Scattering (MBES)” package. This package is based on the method of moment for bodies of revolution. A brief review of this method is given in the next chapter. This method was proposed by Kishk [13]. For more details see the reference [13].

Microstrip Antenna Overview

2.1. Introduction	7
2.2. Microstrip Antenna Structure	7
2.3. Analytical Method: the Simple Cavity Model	11
2.4. Numerical Method: Method of Moments	17

2.1. Introduction

The popularity of the microstrip antennas stems from the fact that the structure is “planar” in configuration and enjoys all the advantages of printed circuit technology [4]. Microstrip antennas have many attractive features which make them suitable for many practical designs. They have been used in many applications such as satellite communication, radar, missile telemetry and much more. Some of their notable advantages are:

- Having light weight and low volume
- Low fabrication cost
- Compatibility with integrated circuits
- Low scattering cross section
- Possibility of mounting on different bodies (missiles, radars,...)

This chapter gives a review of microstrip antennas and the mathematical methods which have been used to investigate their performance.

2.2. Microstrip Antenna Structure

Microstrip antennas can be divided into three categories:

- Microstrip patch antennas
- Microstrip travelling-wave antennas
- Microstrip slot antennas

Microstrip patch antenna in its simplest form consists of a radiating patch, on one side of a dielectric substrate which has a ground plane on the other side. This configuration has been shown in Fig. 2.1. The patch can have any shape (Fig. 2.2).

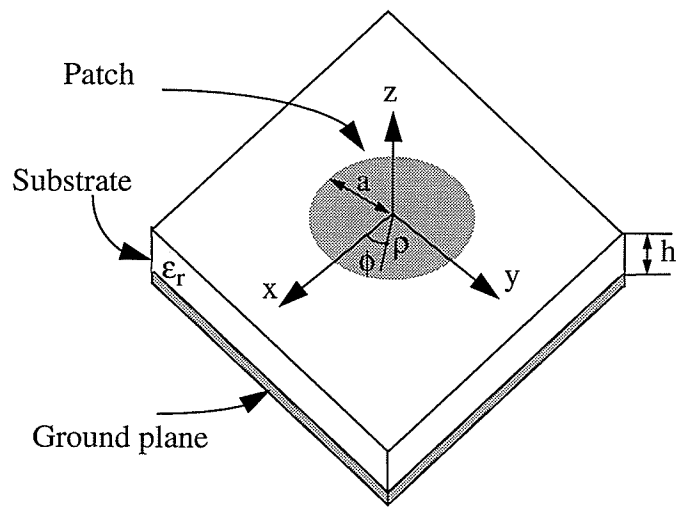


Fig. 2.1. Circular microstrip patch antenna

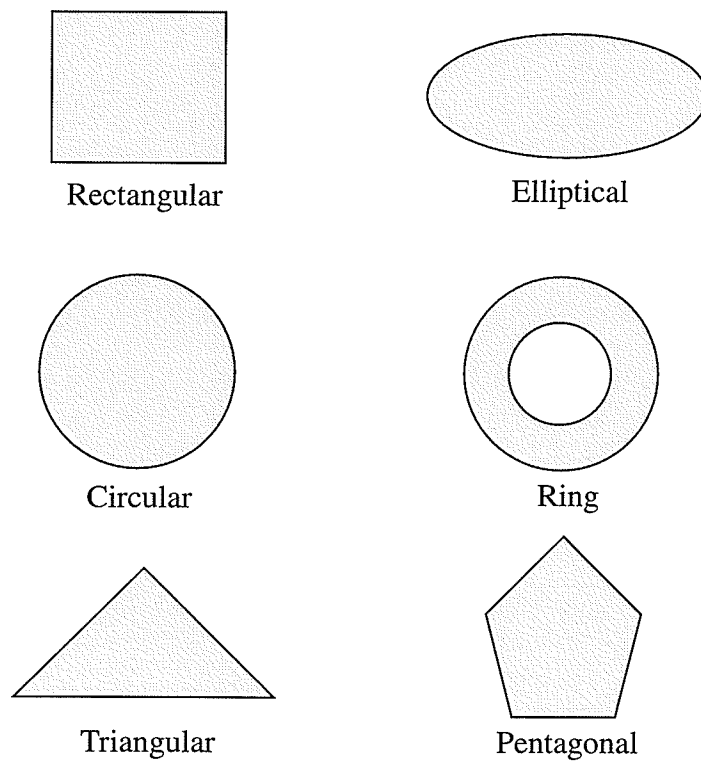


Fig. 2.2. Some configurations of often used microstrip patches

Among these patches, the circular and rectangular patches are the most important ones. Fig. 2.1 shows a circular patch which is the configuration used in the present study.

Radiation from microstrip antenna occurs from the fringing fields between the edge of the microstrip antenna conductor and the ground plane. This can be understood by considering the simple case of rectangular microstrip patch with length of half a wavelength (Fig. 2.3). The fringing field at each end can be resolved into normal and tangential components with respect to the ground plane. At the edge, the electric field is almost normal. These normal components are out of phase. Because the equivalent magnetic current is:

$$\vec{M} = \vec{E} \times \hat{n} \approx \begin{cases} \pm E_z \hat{x} & \text{x-sides} \\ -E_z \hat{y} & \text{y-sides} \end{cases} \quad (2-1)$$

where \hat{n} is the unit vector normal to the sides, \hat{x} and \hat{y} respectively are unit vectors in the x and y directions. The electric field and thus the magnetic current change the sign along the x axis, but it is constant along the y axis (at the edges). Therefore, the x-sides do not radiate efficiently and essentially all the radiation field is from the y-sides. As a result, the patch may be represented by two slots, $\lambda/2$ apart, excited in phase and radiating in the half space above the ground plane.

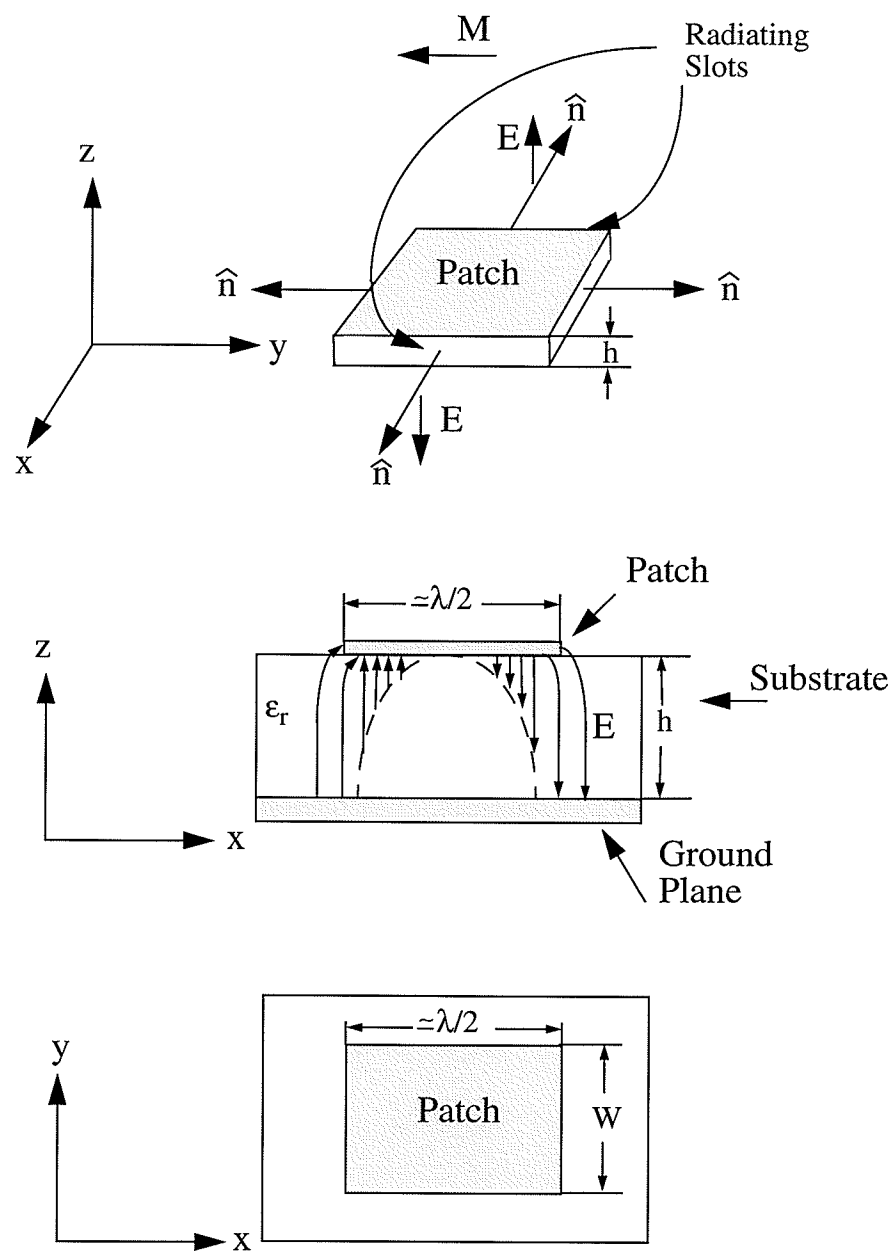


Fig. 2.3. Radiation mechanism of a rectangular microstrip antenna

Microstrip patch antenna may be fed by a microstrip line or coaxial line. Impedance matching is usually required between the feed line and antenna. It may be achieved by properly selecting the location of the feed line. The location of the feed line also determines which mode is excited [4].

2.3. Analytical Method: the Simple Cavity Model

Various methods for analysis of a disk microstrip antennas are available in the literature. Some of them are:

- Simple cavity model
- Cavity model with source
- Modal expansion model
- Wire grid model
- Green's function method

The cavity model is the simplest method used for predicting adequately the radiation characteristics of circular shape microstrip antennas [4]. In this study the cavity model has been used to determine the patch size in terms of frequency, so this method will be reviewed in this chapter.

In this method it is assumed that the substrate thickness (h) is much less than the free space wavelength λ_0 . The dielectric field within the substrate has essentially only a z component, and magnetic field has essentially x and y components (TM mode).

The microstrip disk can be modelled by a cylindrical cavity, bounded at its top and bottom by electric walls and on its sides by magnetic walls (Fig. 2.4), so the problem will be a cavity problem. Magnetic walls form an aperture ring with the width of h .

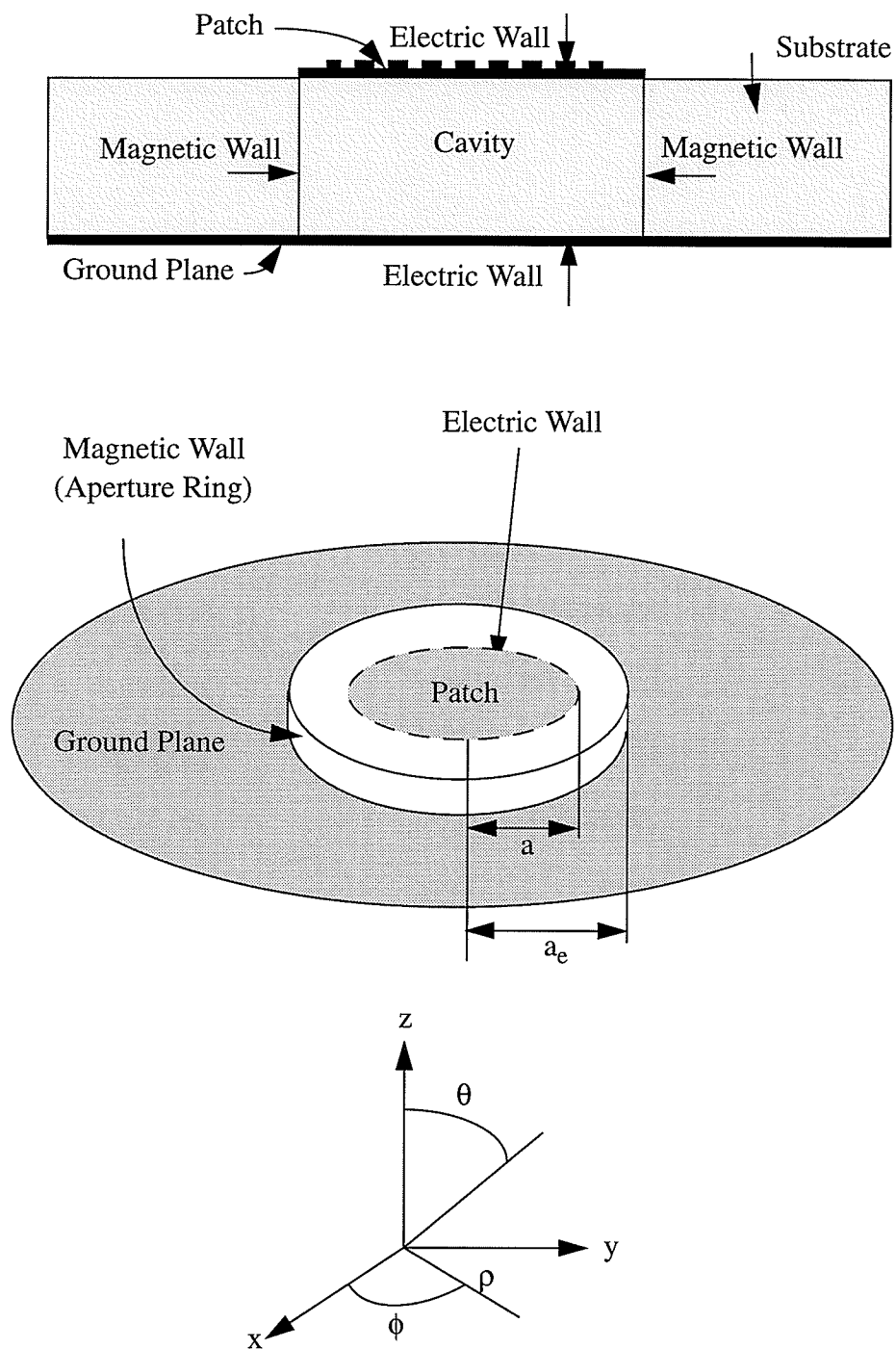


Fig. 2.4. Cavity model of microstrip antenna

2.3.1. Fields

Electric fields must satisfy the wave equation subject to magnetic wall boundary conditions at the patch edge.

$$\begin{cases} (\nabla^2 + k^2) \vec{E} = 0 & k = \omega\sqrt{\mu\epsilon} \\ \left. \frac{\partial \vec{E}}{\partial \rho} \right|_{\rho=a_e} = 0 \end{cases} \quad (2-2)$$

where ρ is the radial distance from origin and a is the patch radius and a_e is an effective radius, where the patch resonates, ($a_e > a$), a_e is larger than a , due to fringing field (Fig. 2.4). Thus the solution of the wave equation in cylindrical coordinates is:

$$E_z = E_0 J_n(k\rho) \cos n\phi \quad (2-3)$$

where $J_n(k\rho)$ are Bessel functions of order n . The magnetic components become:

$$\begin{aligned} H_\rho &= \frac{j}{\omega\mu} \frac{1}{\rho} \frac{\partial E_z}{\partial \phi} = -\frac{jn}{\omega\mu\rho} E_0 J_n(k\rho) \sin n\phi \\ H_\phi &= -\frac{j}{\omega\mu} \frac{1}{\rho} \frac{\partial E_z}{\partial \rho} = -\frac{jk}{\omega\mu} E_0 J'_n(k\rho) \cos n\phi \end{aligned} \quad (2-4)$$

where the prime sign signifies differentiation with respect to the argument. Boundary conditions requires that:

$$\begin{aligned} J'_n(ka_e) &= 0 \\ ka_e &= k_{nm} \end{aligned} \quad (2-5)$$

where k_{nm} is the m th zero of the derivative of Bessel function of order n . These zeros, for some lower order modes, are listed in Table (2-1). Thus for mode configuration a radius may be found that results in a resonance corresponding to zeros of the derivative of the Bessel function. Fig. 2.5 shows the Bessel functions of order 1-4.

Table (2-1) Zeros of derivative of Bessel functions

m	n=0	n=1	n=2	n=3	n=4
1	0	1.841	3.054	4.201	5.317
2	3.832	5.331	6.706	8.015	9.282

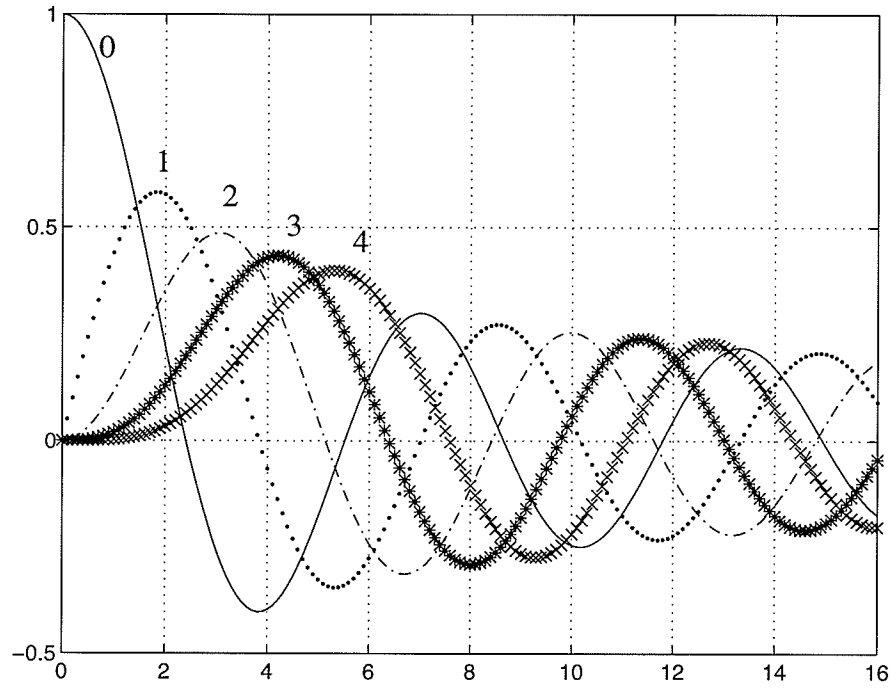


Fig. 2.5. Bessel functions of order 0-4

2.3.2. Far Fields

The far field of a disk antenna can be calculated from the potential functions. Using a vector magnetic potential and the image theory, with assumption of constant E_z (i.e. $h/\lambda_0 \ll 1$), the ground plane can be replaced by an equivalent magnetic current:

$$\begin{aligned}\vec{M} &= 2\vec{E} \times \hat{n} = 2E_z \hat{\phi} \\ \vec{E} &= E_z \hat{z}\end{aligned}\tag{2-6}$$

where \hat{n} is the unit vector normal to the magnetic walls (aperture surface), $\hat{\phi}$ and \hat{z} are respectively the unit vectors in the ϕ and z directions, and E_z is given by (2-3).

By integrating equation (2-6) over the aperture ring surface, the vector electric potential can be calculated. Then the far field in spherical coordinates may be found from this vector electric potential.

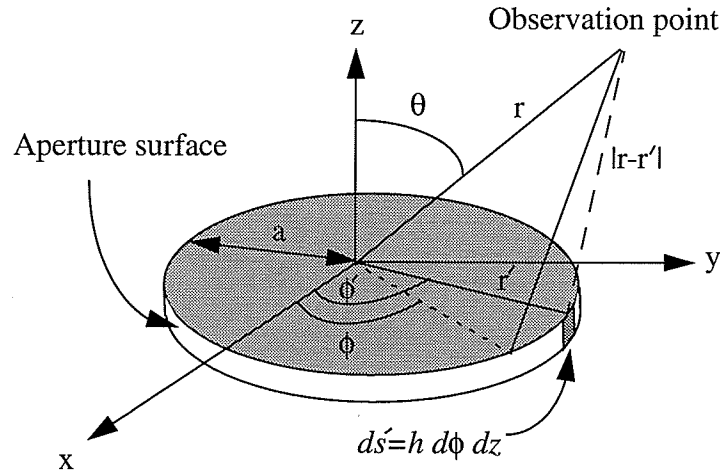


Fig. 2.6. Coordinate and aperture surface for calculating far fields

$$\vec{F} = \frac{\epsilon_0}{4\pi} \iint_{s'} \vec{M}(r') \frac{e^{-jk_0|\vec{r}-\vec{r}'|}}{|\vec{r}-\vec{r}'|} ds' \quad (2-7)$$

$$ds' = h d\phi dz \quad \begin{array}{l} 0 < \phi < 2\pi \\ 0 < z < h \end{array}$$

where s' is the aperture surface with a width of h , and \vec{r} and \vec{r}' are position vectors of field and source points, respectively, i.e. from origin to observation point and source point. Magnetic current must be transferred from the cylindrical coordinates to spherical coordinates. Far field in free space can be calculated from the following equations [14].

$$\begin{cases}
H(r) = -\frac{j}{\omega\mu\epsilon} \nabla(\nabla \cdot \vec{F}) - j\omega\vec{F} \\
E(r) = -\frac{1}{\epsilon} \nabla \times \vec{F}
\end{cases} \quad (2-8)$$

$$\begin{cases}
H(r) \approx -j\omega\vec{F} \\
E(r) \approx \eta_0 H(r)
\end{cases} \quad r \rightarrow \infty$$

where η_0 is the impedance of free space. Results for electric field components at the far field points are given by (2-9).

$$\begin{cases}
E_\theta = j^n \frac{Vak_0}{2} \frac{e^{-jk_0r}}{r} \cos n\phi [J_{n+1}(k_0 a \sin \theta) - J_{n-1}(k_0 a \sin \theta)] \\
E_\phi = j^n \frac{Vak_0}{2} \frac{e^{-jk_0r}}{r} \cos \theta \sin n\phi [J_{n+1}(k_0 a \sin \theta) + J_{n-1}(k_0 a \sin \theta)]
\end{cases} \quad r \rightarrow \infty \quad (2-9)$$

$V = hE_0 J_n(ka)$ V Edge voltage at $\phi = 0$

2.3.3. Resonant Frequency

The resonant frequency for the TM_{nm} mode are the solutions of (2-5), from which f_r may be evaluated.

$$f_r = \frac{k_{nm}c}{2\pi a_e \sqrt{\epsilon_r}} \quad (2-10)$$

$$a_e = a \left[1 + \frac{2h}{\pi a \epsilon_r} \left(\ln \frac{\pi a}{2h} + 1.7726 \right)^{\frac{1}{2}} \right]$$

where a is the physical radius of conducting patch, k_{nm} is the m th zero of the derivative of Bessel function of order n , c is the velocity of light in free space, h is the dielectric thickness, and ϵ_r is the relative permittivity of the dielectric substrate. a_e (shown in Fig. 2.4) is an effective radius and is slightly larger than the physical radius of the patch (a). It is defined to take into account the fringing field. From this set of equations, by knowing h/λ_0 and ϵ_r , a/λ_0 for the desired mode can be cal-

culated.

2.4. Numerical Method: Method of Moments

In the present study the method proposed by Kishk is used. The detail of this method is given in reference [13] and a brief review is given here.

Microstrip antennas are made of conductors and dielectrics. A general problem of this type is shown in Fig. 2.7. The surfaces S_{ce} , S_{cd} and S_{de} refer to the boundaries between the conductor and exterior, conductor and dielectric, and dielectric and exterior regions, respectively. Also (\vec{E}^d, \vec{H}^d) and (\vec{E}^e, \vec{H}^e) refer to the field vectors within the dielectric and the exterior regions. V^d is a finite volume filled with homogenous material of permittivity ϵ_d and permeability μ_d and bounded by two surfaces S_{de} and S_{cd} . V^e represents the exterior region, with permittivity ϵ_e and permeability μ_e , which is bounded by two surfaces S_{de} and S_{ce} . The sources are provided by impressed electric and magnetic currents $(\vec{J}^{ie}, \vec{M}^{ie})$ in V^e and $(\vec{J}^{id}, \vec{M}^{id})$ in V^d .

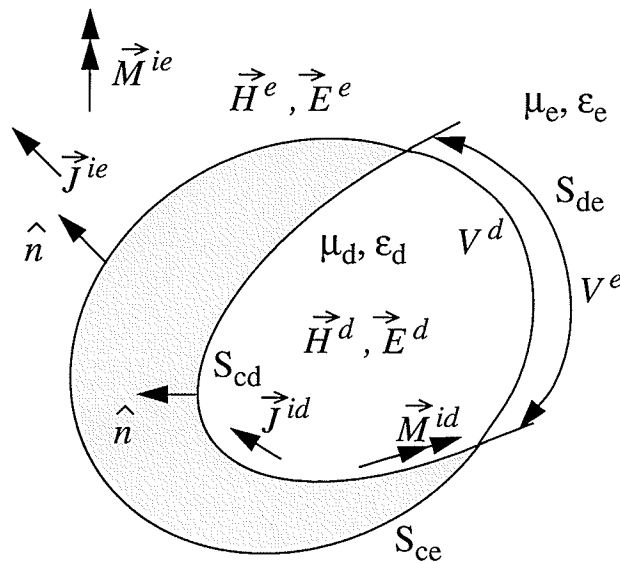


Fig. 2.7. The general form of problem

The boundary conditions are given by (2-11).

$$\left\{ \begin{array}{ll} \hat{n} \times \vec{E}^d = 0 & \text{on } S_{cd} \\ \hat{n} \times \vec{E}^e = 0 & \text{on } S_{ce} \\ \hat{n} \times \vec{E}^d = \hat{n} \times \vec{E}^e \\ \hat{n} \times \vec{H}^d = \hat{n} \times \vec{H}^e \end{array} \right\} \quad \text{on } S_{de} \quad (2-11)$$

where \hat{n} is outward normal on each surface considered. Surface equivalent currents are:

$$\left\{ \begin{array}{ll} \vec{J}_{cd} = \hat{n} \times \vec{H}^d & \text{on } S_{cd} \\ \vec{J}_{ce} = \hat{n} \times \vec{H}^e & \text{on } S_{ce} \\ \vec{J}_{de} = \hat{n} \times \vec{H}^e \\ \vec{M} = -\hat{n} \times \vec{E}^e \end{array} \right\} \quad \text{on } S_{de} \quad (2-12)$$

The currents \vec{J}_{cd} , \vec{J}_{ce} and \vec{J}_{de} are equivalent electric currents on each surface and \vec{M} is the magnetic current on the interface between the dielectric and the exterior region. From the above equations and definitions the following set of equations can be written:

$$\left\{ \begin{array}{ll} \hat{n} \times \vec{E}^d(\vec{J}_{cd} + \vec{J}_{de}, \vec{M}) = \hat{n} \times \vec{E}^d(\vec{J}^{id}, \vec{M}^{id}) & \text{just outside } S_{cd} \\ \hat{n} \times \vec{E}^d(\vec{J}_{cd} + \vec{J}_{de}, \vec{M}) = \hat{n} \times \vec{E}^d(\vec{J}^{id}, \vec{M}^{id}) & \text{just outside } S_{de} \\ -\hat{n} \times \vec{E}^e(\vec{J}_{ce} + \vec{J}_{de}, \vec{M}) = \hat{n} \times \vec{E}^e(\vec{J}^{ie}, \vec{M}^{ie}) & \text{just inside } S_{ce} \\ -\hat{n} \times \vec{E}^e(\vec{J}_{ce} + \vec{J}_{de}, \vec{M}) = \hat{n} \times \vec{E}^e(\vec{J}^{ie}, \vec{M}^{ie}) & \text{just inside } S_{de} \end{array} \right. \quad (2-13)$$

$$\left\{ \begin{array}{ll} \hat{n} \times \vec{H}^d(\vec{J}_{cd} + \vec{J}_{de}, \vec{M}) = \hat{n} \times \vec{H}^d(\vec{J}^{id}, \vec{M}^{id}) & \text{just outside } S_{cd} \\ \hat{n} \times \vec{H}^d(\vec{J}_{cd} + \vec{J}_{de}, \vec{M}) = \hat{n} \times \vec{H}^d(\vec{J}^{id}, \vec{M}^{id}) & \text{just outside } S_{de} \\ -\hat{n} \times \vec{H}^e(\vec{J}_{ce} + \vec{J}_{de}, \vec{M}) = \hat{n} \times \vec{H}^e(\vec{J}^{ie}, \vec{M}^{ie}) & \text{just inside } S_{ce} \\ -\hat{n} \times \vec{H}^e(\vec{J}_{ce} + \vec{J}_{de}, \vec{M}) = \hat{n} \times \vec{H}^e(\vec{J}^{ie}, \vec{M}^{ie}) & \text{just inside } S_{de} \end{array} \right.$$

where $\vec{E}^e(\vec{J}, \vec{M})$ and $\vec{E}^d(\vec{J}, \vec{M})$ are the electric fields due to currents \vec{J} and \vec{M} , radiating in media characterized by ϵ_e, μ_e and ϵ_d, μ_d , respectively. $\vec{H}^e(\vec{J}, \vec{M})$ and $\vec{H}^d(\vec{J}, \vec{M})$ are associated magnetic fields. The basic equations for these fields can be written as:

$$\begin{aligned}\vec{E}^q(\vec{J}, \vec{M}) &= -j\omega\vec{A}^q - \nabla\Phi^q - \frac{1}{\epsilon_q}\nabla\times\vec{F}^q \\ \vec{H}^q(\vec{J}, \vec{M}) &= -j\omega\vec{F}^q - \nabla\Psi^q + \frac{1}{\mu_q}\nabla\times\vec{A}^q\end{aligned}\quad (2-14)$$

where

$$\begin{aligned}\vec{A}^q &= \mu_q \int_S \vec{J} G^q ds \\ \vec{F}^q &= \epsilon_q \int_S \vec{M} G^q ds \\ \Phi^q &= \frac{1}{\epsilon_q} \int_S \sigma G^q ds \\ \Psi^q &= \frac{1}{\mu_q} \int_S m G^q ds \\ \sigma &= -\frac{1}{j\omega} \nabla_s \cdot \vec{J} \\ m &= -\frac{1}{j\omega} \nabla_s \cdot \vec{M}\end{aligned}\quad (2-15)$$

The function G^q is the scalar Green's function, which is given by:

$$G^q = \frac{e^{-jk_q R}}{4\pi R} \quad (2-16)$$

where $R = |\vec{r} - \vec{r}'|$ is the distance between the field point (\vec{r}) and the source point (\vec{r}') on the surface, $k_q = \omega\sqrt{\mu_q\epsilon_q}$ is the propagating constant and q represents e or d .

There are eight equations with four unknown field vectors. Various combinations of these equations can be selected. The most popular ones are the E-field, H-field and C-field formulations.

The E-field is a set of the first four equations in (2-13). They are uniquely determined if and only if the region inside S_{ce} and S_{de} when filled with ϵ_e and μ_e , and enclosed by a perfect conductor is not a resonant cavity. Since all four equations are satisfied by an object surface, the formulation is called E-field formulation.

The H-field formulation consists of the second four equations in (2-13). This set of equations determines currents uniquely, if and only if the region inside S_{ce} and S_{de} , filled with ϵ_e and μ_e , and enclosed by conductor, is not a resonant cavity.

C-field is a linear combination of the two set of equations used for E and H-field formulations.

2.4.1. Bodies of Revolution

The above formulation can be applied to rotationally symmetric bodies like a microstrip disk antenna with circular ground plane. The reduction of integral equations to matrix equations involving unknown surface currents follows the procedure well known for Bodies of Revolution. On the object's surface two orthogonal tangent vectors, t and ϕ , are selected such that t is along the generating curve and ϕ is along the azimuthal angle, as shown in Fig. 2.8.

Both electric and magnetic surface currents exist and are represented as:

$$\begin{cases} \vec{J}(\vec{r}) = \hat{u}_t I^t(t, \phi) + \hat{u}_\phi I^\phi(t, \phi) \\ \vec{M}(\vec{r}) = \hat{u}_t M^t(t, \phi) + \hat{u}_\phi M^\phi(t, \phi) \end{cases} \quad (2-17)$$

The electric current exists on both conducting and dielectric surfaces, but magnetic current exists only on the dielectrics. If the total generating curve of all bodies is sub-divided into N_c segments, and that of dielectrics into N_d segments, the surface currents can be represented as follows.

$$\begin{cases} \vec{J}(\vec{r}) = \sum_{n=M_1}^{M_2} \sum_{j=1}^{N_c} I_{nj}^t J_{nj}^t(t, \phi) \hat{u}_t + I_{nj}^\phi J_{nj}^\phi(t, \phi) \hat{u}_\phi \\ \vec{M}(\vec{r}) = \sum_{n=M_1}^{M_2} \sum_{j=N_c+1}^{N_c+N_d} K_{nj}^t M_{nj}^t(t, \phi) \hat{u}_t + K_{nj}^\phi M_{nj}^\phi(t, \phi) \hat{u}_\phi \end{cases} \quad (2-18)$$

where J_{nj}^t , J_{nj}^ϕ , K_{nj}^t , and K_{nj}^ϕ are expansions functions. Along the t vector, expansion functions are selected as a discrete set of overlapping triangle functions, and along the ϕ vector Fourier-type basis functions are chosen:

$$J_{nj}^t = J_{nj}^\phi = K_{nj}^t = K_{nj}^\phi = f_j(t) e^{jn\phi} \quad (2-19)$$

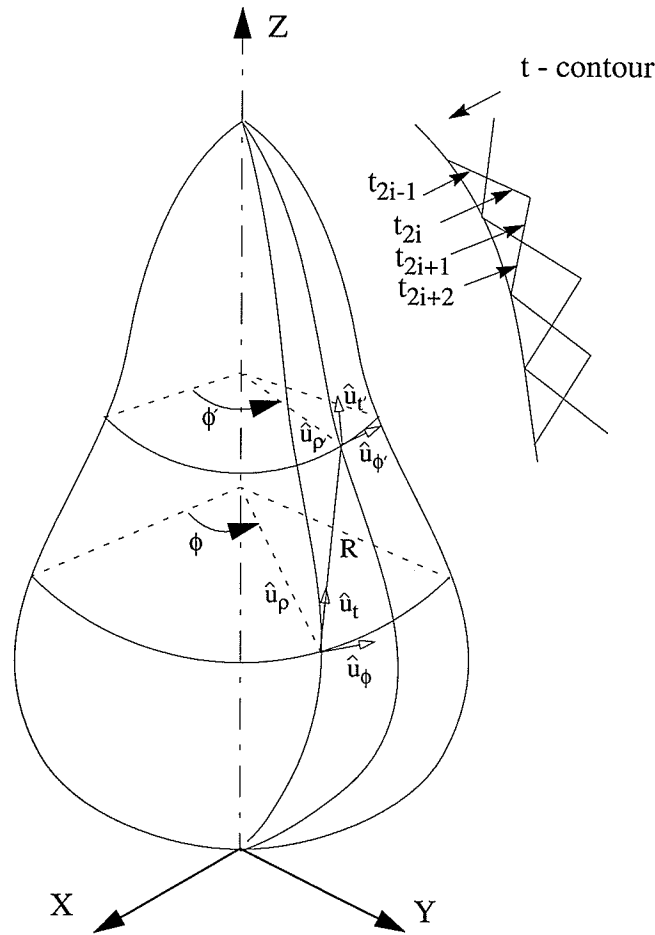


Fig. 2.8. Geometry of body of revolution

The azimuthal modes in the range M_1 to M_2 are used to represent the surface currents. The coefficients I_{nj}^t , I_{nj}^ϕ , M_{nj}^t and M_{nj}^ϕ are current coefficients to be determined. Substituting (2-18) into the set of equations, such as E-field or H-field equations, results in a matrix equation. The resulting inner product is then integrated over the surface with testing functions defined by:

$$\begin{aligned}\vec{W}_{li}^t &= \hat{u}_i f_i(t) e^{-jl\phi} \\ \vec{W}_{li}^\phi &= \hat{u}_\phi f_i(t) e^{-jl\phi}\end{aligned}\quad (2-20)$$

The result would be in the general matrix equation form as follows.

$$\begin{bmatrix} \overline{T}_n \end{bmatrix} \begin{bmatrix} \overline{I}_n \end{bmatrix} = \begin{bmatrix} \overline{V}_n \end{bmatrix} \quad n = 0, \pm 1, \pm 2, \dots \quad (2-21)$$

where \overline{T}_n is a square matrix representing in impedance and the admittance sub-matrices, \overline{I}_n is a column matrix for the unknown expansion coefficients of \vec{J} and \vec{M} , and \overline{V}_n is the excitation column matrix.

The excitation matrix for an electric dipole can be determined from the potential vectors given by:

$$\begin{cases} \vec{E}^{inc, q} = -j\omega \vec{A}^q - \nabla \Phi^q \\ \vec{H}^{inc, q} = -\frac{1}{\mu_q} \nabla \times \vec{A}^q \end{cases} \quad (2-22)$$

where

$$\begin{cases} \vec{A}^q = \frac{-jk_q \mu_q}{4\pi r} \vec{I} l h_0^{(2)} \left(k_q |\vec{r} - \vec{r}'| \right) \\ \Phi^q = \frac{\eta_q}{4\pi r} \vec{I} l \cdot \nabla h_0^{(2)} \left(k_q |\vec{r} - \vec{r}'| \right) \end{cases} \quad (2-23)$$

and $h_0^{(2)}$ is the spherical Hankel function of the second kind and zero order and $\vec{I} l$ is the dipole moment with an arbitrary orientation. The inner products of \vec{E}^{inc} and \vec{H}^{inc} with testing functions

provide the elements of the excitation matrix $\left[\overline{V}_n \right]$ for each formulation.

After filling the impedance matrices $\left[\overline{T}_n \right]$ and excitation matrices $\left[\overline{V}_n \right]$ of equation (2-21), this equation can be solved for unknown coefficients. From these coefficients electric and magnetic currents (\vec{J} and \vec{M}) are determined by using equation (2-18). After determining the induced currents, \vec{J} and \vec{M} , on the surface, electric and magnetic vector potentials (\vec{F} and \vec{A}) can be calculated using following equations.

$$\begin{aligned}\vec{F} &= \frac{\epsilon_0}{4\pi} \iint_{s'} \vec{M}(r') \frac{e^{-jk_0|\vec{r}-\vec{r}'|}}{|\vec{r}-\vec{r}'|} ds' \\ \vec{A} &= \frac{\mu_0}{4\pi} \iint_{s'} \vec{J}(r') \frac{e^{-jk_0|\vec{r}-\vec{r}'|}}{|\vec{r}-\vec{r}'|} ds'\end{aligned}\quad (2-24)$$

where s' is the surface of the bodies, and \vec{r} and \vec{r}' are position vectors, respectively, from origin to observation point and source point.

Once the vector potentials calculated, the far field components E_ϕ and E_θ can be calculated [14].

$$\begin{aligned}E_\phi &= -j\omega\vec{A}_\phi + j\omega\eta_0\vec{F}_\phi \\ E_\theta &= -j\omega\vec{A}_\theta - j\omega\eta_0\vec{F}_\theta\end{aligned}\quad (2-25)$$

where \vec{A}_ϕ and \vec{A}_θ are components of magnetic vector potential in the ϕ and θ directions, respectively. Similarly \vec{F}_ϕ and \vec{F}_θ are components of electric vector potential in the ϕ and θ directions, respectively. η_0 is the impedance of free space.

Effects of the Ground Plane Radius

3.1. Introduction	25
3.2. Simulation Method	27
3.3. Effects on the Gain	29
3.4. Effects on the Radiation Pattern	38
3.5. Effects on Circular Polarization	58
3.6. Summary	66

3.1. Introduction

The analysis of microstrip antenna is normally difficult to handle. In most cases, analyses have been approximate and assumed an infinite ground plane. This assumption enables using microstrip Green's function. In practice, however, the ground plane is finite. The size of ground plane affects the radiation patterns and thus, the gain, beamwidth and cross-polarization. To show importance of these effects, some samples of radiated fields are given in Figs. 3.1 and 3.2. The corresponding gains are listed in Tables (3-1) and (3-2). They indicate that antenna gain peaks for a certain ground plane size.

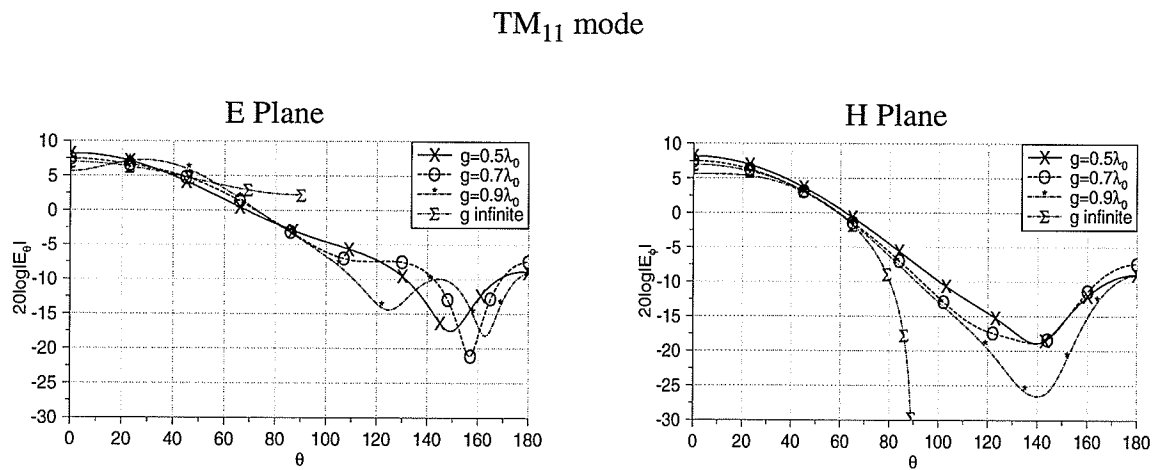


Fig. 3.1. Effect of the ground plane radius on the radiation patterns of TM_{11} mode

Table (3-1) Gain of TM_{11} mode with finite and infinite ground planes

Ground plane size (g)/ λ_0	Gain(dBi)
0.3	7.025
0.5	8.338
0.7	7.460
Infinity	6.965

TM_{21} mode

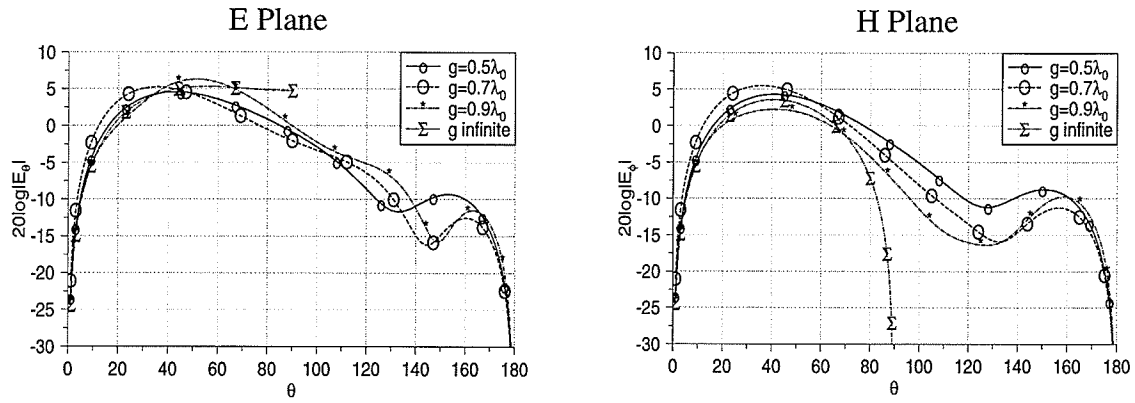


Fig. 3.2. Effect of the ground plane radius on the radiation patterns of TM_{21} mode

Table (3-2) Gain for TM_{21} mode with finite and infinite ground planes

Ground plane size (g)/ λ_0	Gain(dBi)
0.5	4.566
0.7	5.460
0.9	6.285
Infinity	5.300

In this chapter the effects of the ground plane radius on the gain, radiation patterns and circular polarization of circular microstrip antennas, for different modes and substrate permittivities are discussed.

3.2. Simulation Method

3.2.1. Antenna Geometry

Fig. 3.3 shows the geometry of the problem. Using cavity model, the patch radius (a) is calculated such that the desired mode is excited. A program in C language was written to calculate the patch size. Its source is given in Appendix A. Table (3-3) shows the patch size for different modes and substrate permittivities.

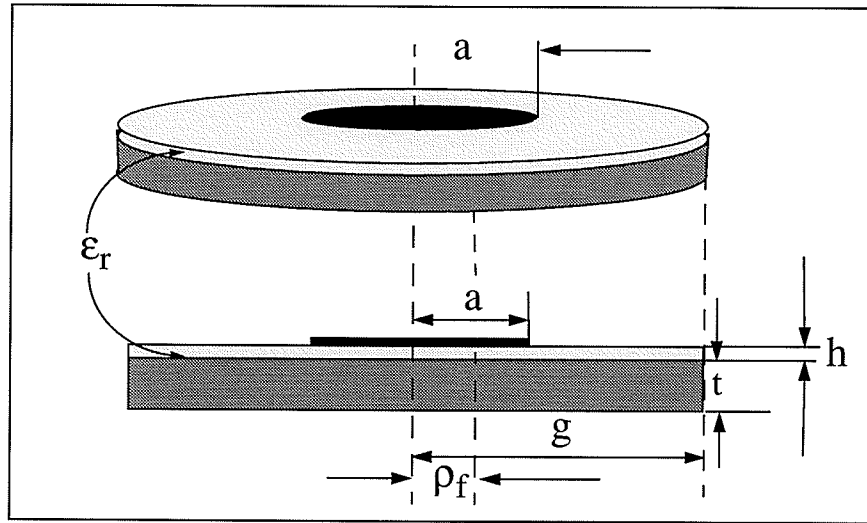


Fig. 3.3. Circular microstrip patch antenna with finite ground plane

Table (3-3) Patch radius $(a)/\lambda_0$ for $h=0.01\lambda_0$

ϵ_r	2.5	4.0	6.0
TM ₁₁	0.1789	0.1427	0.1172
TM ₂₁	0.3003	0.2388	0.1957
TM ₃₁	0.4154	0.3298	0.2700
TM ₄₁	0.5273	0.4183	0.3424

The substrate thickness (h) controls the antenna bandwidth, however, it increases the cost and weight and is desired to be small. For this study $h=0.01\lambda_0$ was chosen. The ground plane radius (g) and substrate permittivity (ϵ_r) have been changed to investigate the effects of them on the performance of antenna. The ground plane thickness (t) was chosen to be $0.1\lambda_0$, but simulation showed that this parameter does not have any important effect on the results.

3.2.2. Excitation

The excitation is simulated by an electric dipole immersed in the dielectric substrate. Its location is selected to provide a good impedance match. According to Antoskiewicz and Shafai [15], feed location for 50Ω impedance match is given by Table (3-4).

Table (3-4) Ratio of feed location to patch size (ρ_f/a) for different modes

Mode	ρ_f/a
TM ₁₁	0.25
TM ₂₁	0.50
TM ₃₁	0.60
TM ₄₁	0.65

For the first mode only one dipole was used. Its location was $x=\rho_f$, $y=0$, $z=t+h/2$. For the higher order modes two dipoles were used, one at each side of patch centre, i.e. $x = \pm\rho_f$, $y=0$, $z=t+h/2$. For an even mode excitation they were in-phase and for an odd mode excitation they were out of phase.

3.2.3. Gain Calculation

The directivity of an antenna is defined as the ratio of the power density in the main beam to

the average power density.

$$D = \frac{\text{Power radiated per unit solid angle}}{\text{Average power radiated per unit solid angle}} = \frac{dP_r/d\Omega}{P_r/4\pi} \quad (3-1)$$

where $dP_r/d\Omega$ is the intensity of radiation, and is obtained by multiplying the Poynting vector flux density by r^2 . P_r is the total radiated power. The total radiated power can be computed by integrating the Poynting vector power flux through a closed spherical surface surrounding the antenna. Gain was calculated using equation (3-2). The program written for the directive gain calculation is given in Appendix B.

$$D(\theta_0, \phi_0) = \frac{4\pi |E(\theta_0, \phi_0)|^2}{\int_0^\pi \int_0^{2\pi} |E(\theta, \phi)|^2 \sin \theta d\theta d\phi} \quad (3-2)$$

$$G_{max} = \eta \frac{4\pi |E_{max}|^2}{\int_0^\pi \int_0^{2\pi} |E(\theta, \phi)|^2 \sin \theta d\theta d\phi}$$

3.3. Effects on the Gain

3.3.1. Simulation Results

The antenna gain is one of its main radiation parameters. For microstrip antennas it is often assumed that a larger ground plane should give a larger gain. This study shows that this assumption is not correct. Figs. 3.4 to 3.7 and Tables (3-5) to (3-8) show the variation of gain of different modes with the ground plane radius. They show that the gain is small initially and increases rapidly after a certain minimum radius. The dependence of the gain on the ground plane radius is periodic. For each mode there is a ground plane radius which maximizes the gain, independently of the substrate permittivity. Table (3-9) shows the minimum and optimum ground plane radii for

each mode.

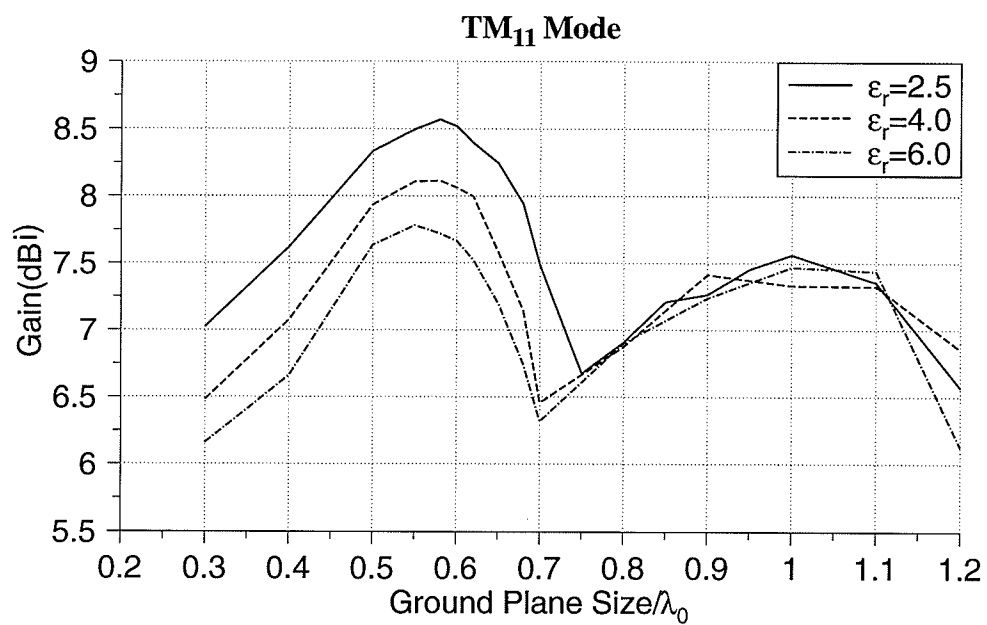


Fig. 3.4. Gain variation for TM₁₁ mode

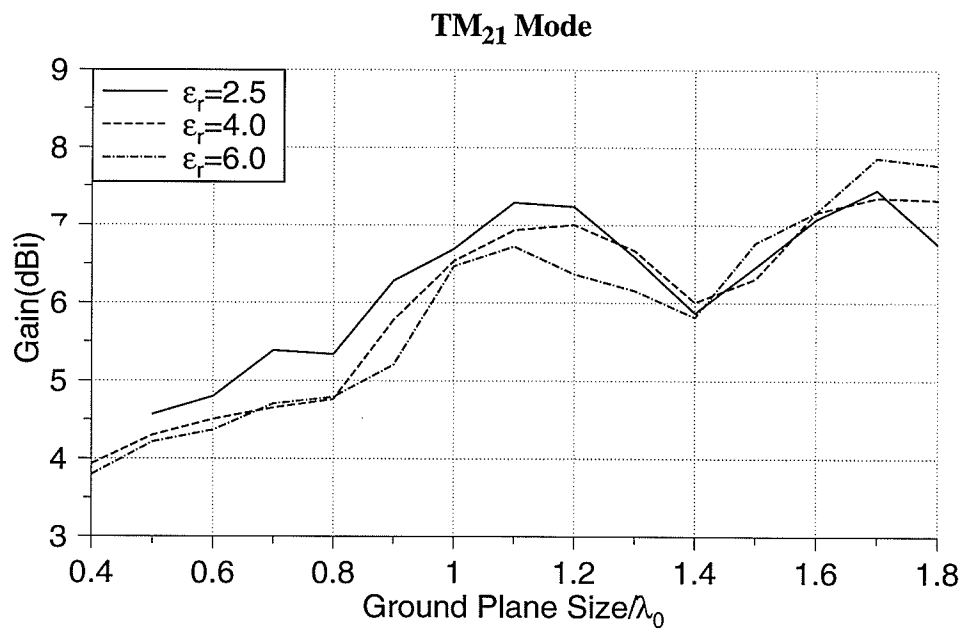


Fig. 3.5. Gain variation for TM₂₁ mode

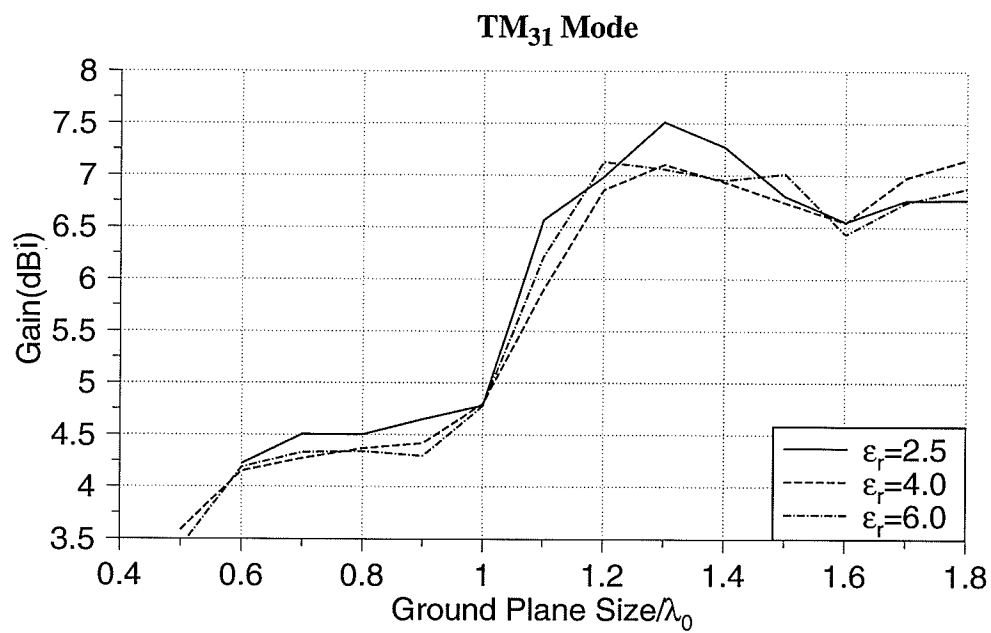


Fig. 3.6. Gain variation for TM₃₁ mode

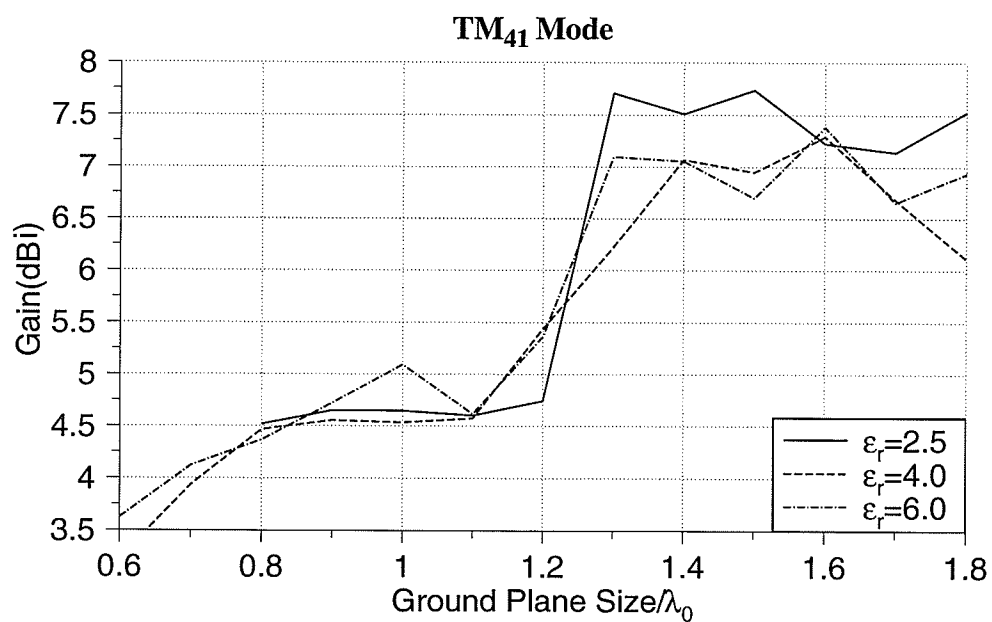


Fig. 3.7. Gain variation for TM₄₁ mode

Table (3-5) Gain for TM_{11} mode (dBi)

g/λ_0	$\epsilon_r=2.5$	$\epsilon_r=4.0$	$\epsilon_r=6.0$
0.3	7.0249	6.4831	6.1609
0.4	7.6194	7.0747	6.6613
0.5	8.3378	7.9375	7.6362
0.6	8.5193	8.0638	7.6657
0.7	7.4879	6.4580	6.3206
0.8	6.9071	6.8767	6.9026
0.9	7.2657	7.4147	7.2416
1.0	7.3585	7.3342	7.4721
1.1	6.5707	7.3278	7.4406
1.2		6.8548	6.1271

Table (3-6) Gain for TM_{21} mode (dBi)

g/λ_0	$\epsilon_r=2.5$	$\epsilon_r=4.0$	$\epsilon_r=6.0$
0.5	4.5662	4.3002	4.2148
0.6	4.7968	4.5065	4.3682
0.7	5.3858	4.6531	4.7019
0.8	5.3384	4.7618	4.7912
0.9	6.2854	5.7772	5.2019
1.0	6.6924	6.5417	6.4731
1.1	7.2916	6.9351	6.7268
1.2	7.2361	7.0041	6.3698
1.3	6.5899	6.6722	6.1560
1.4	5.8683	6.0077	5.8159
1.5	6.4622	6.3111	6.7740
1.6	7.0785	7.1631	7.1706
1.7	7.4495	7.3567	7.8671
1.8	6.7582	7.3269	7.7733

Table (3-7) Gain for TM_{31} mode (dBi)

g/λ_0	$\epsilon_r=2.5$	$\epsilon_r=4.0$	$\epsilon_r=6.0$
0.6	4.2234	4.1510	4.1904
0.7	4.5081	4.2728	4.3325
0.8	4.5035	4.3686	4.3439
0.9	4.6492	4.4225	4.2970
1.0	4.7799	4.7959	4.7770
1.1	6.5677	5.8932	6.2119
1.2	6.9846	6.8573	7.1286
1.3	7.5124	7.1003	7.0578
1.4	7.2693	6.9341	6.9519
1.5	6.7964	6.7351	7.0118
1.6	6.5500	6.5439	6.4332
1.7	6.7601	6.9771	6.7378
1.8	6.7656	7.1529	6.8748

Table (3-8) Gain for TM_{41} mode (dBi)

g/λ_0	$\epsilon_r=2.5$	$\epsilon_r=4.0$	$\epsilon_r=6.0$
0.8	4.5186	4.4660	4.3679
0.9	4.651	4.5531	4.7208
1.0	4.6459	4.5355	5.0916
1.1	4.6014	4.5738	4.6177
1.2	4.7441	5.4352	5.3628
1.3	7.7069	6.2225	7.0964
1.4	7.5083	7.0677	7.0553
1.5	7.7378	6.9470	6.6967
1.6	7.2256	7.2895	7.3809
1.7	7.1378	6.6807	6.6555
1.8	7.5265	6.1149	6.9337

Table (3-9) Minimum and optimum ground plane radii

Mode	Minimum ground plane radius	Optimum ground plane radius
TM ₁₁	not exist	0.6
TM ₂₁	0.8	1.1
TM ₃₁	1.0	1.3
TM ₄₁	1.2	1.4

The other important fact is that for higher order modes, when the lower order modes are not eliminated, a local maximum will appear in the gain graph. For example Fig. 3.8 shows a local maximum at $0.8\lambda_0$ for the TM₃₁ mode (for $\epsilon_r=2.5$) and Fig. 3.9 shows a local maximum at λ_0 for the TM₄₁ mode (for $\epsilon_r=4.0$). These local maxima disappear with elimination of the lower order mode.

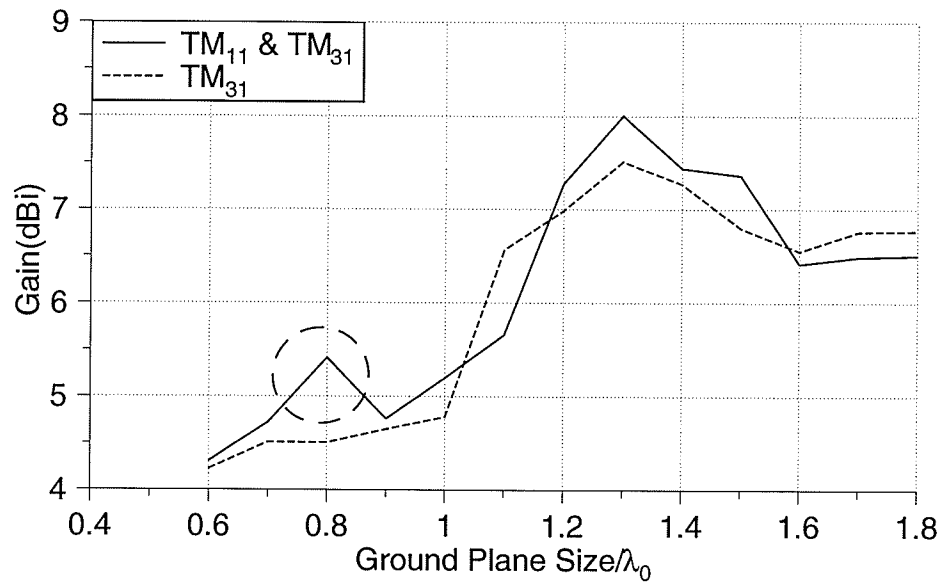


Fig. 3.8. Local maximum for TM_{31} mode (for $\epsilon_r=2.5$)

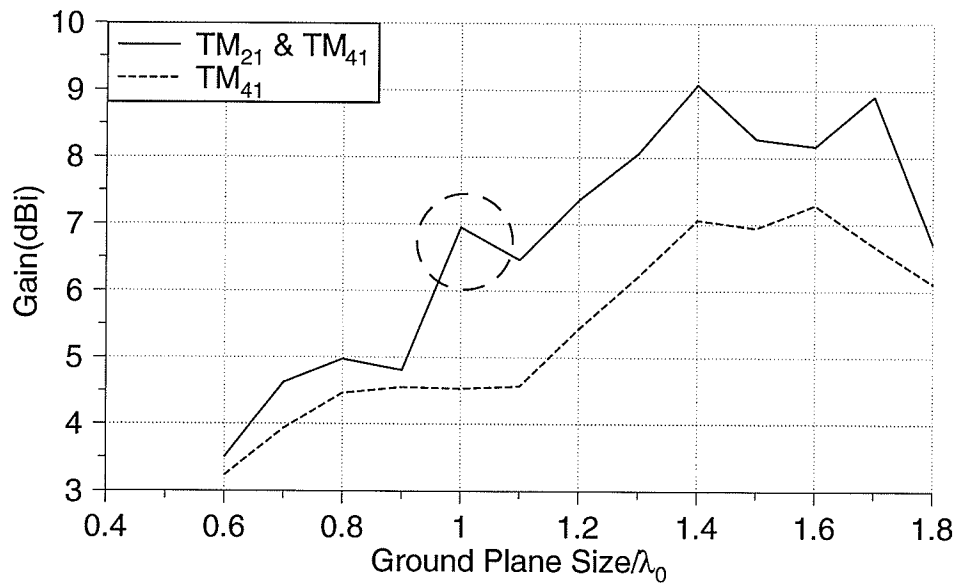


Fig. 3.9. Local maximum for TM_{41} mode (for $\epsilon_r=4.0$)

3.3.2. Experimental Results

In order to confirm simulation results, some experiments were done. The antennas with permittivity of 2.32 were chosen. Radiation patterns were measured in the anechoic chamber site. Return loss were measured with “WILTRON MODEL 360” network analyser. Fig. 3.10 shows the result of return loss measurement. Table (3-10) shows antenna dimensions. Table (3-11) shows the ground planes radii and the corresponding directivities and gains.

Return loss was measured about -13.5dB which gives mismatch loss of 0.2dB. Antenna efficiency assumed to be between 85% and 90% [16]. Fig. 3.11 compares simulation, experimental results and the results taken from [8]. Difference between simulation and experiment could be because of the following facts:

- Efficiency were assumed to be constant, but it changes for different ground planes.
- Inaccuracy in measurements; ground planes were circular disks that antenna were mounted on them. It is possible that in each measurement antennas were not exactly at the centre of the ground plane and this would cause larger error for smaller ground planes.
- Uncertainty in the gain of the standard gain horn.

Table (3-10) Antenna parameters

ϵ_r	2.32
f	3.26GHz
λ_0	9.37cm
h	0.32cm
a	1.65cm
ρ_f	0.40cm

Table (3-11) Experimental and simulation results for gain measurement

g/λ_0	2g(cm)	Simulation Directivity (dBi)	Experiment Gain (dBi)	Experiment Directivity (dBi) $\eta=85\%$	Experiment Directivity (dBi) $\eta=90\%$
0.50	9.4	8.34	6.99	7.89	7.65
0.58	10.9	8.57	7.38	8.28	8.04
0.6	11.3	8.52	7.49	8.39	8.15
0.63	11.9	8.40	7.43	8.33	8.09
0.65	12.2	8.25	7.49	8.39	8.15
0.75	14.2	7.28	6.51	7.41	7.17
0.80	15.1	6.91	6.16	7.06	6.82

WILTRON
360 NETWORK ANALYZER

MODEL:
DEVICE:

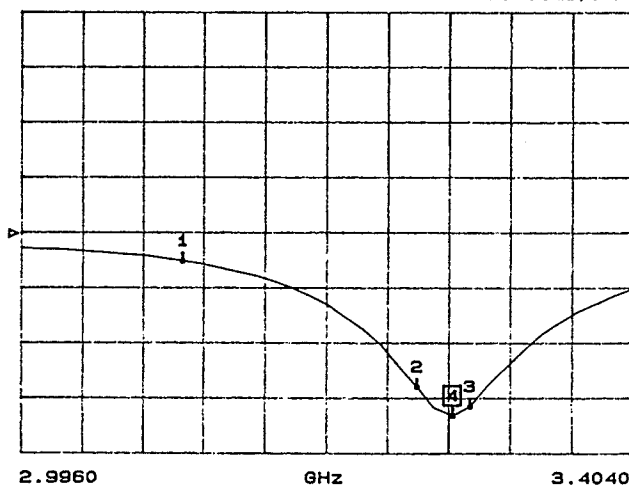
DATE:
OPERATOR:

START: 2.9960 GHz GATE START:
STOP: 3.4040 GHz GATE STOP:
STEP: 0.0120 GHz GATE:
WINDOW:

ERROR CORR: 12 - TERM
AVERAGING: 1 PTS
IF BNDWTH: REDUCED

S11 FORWARD REFLECTION

LOG MAG. ▷REF=0.000dB 5.000dB/DIV



CH 1 - S11
REF. PLANE
0.0000 mm

MARKER 4
3.2840 GHz
-16.592 dB

MARKER TO MAX
▷MARKER TO MIN

1 3.1040 GHz
-2.506 dB

2 3.2600 GHz
-13.878 dB

3 3.2960 GHz
-15.680 dB

Fig. 3.10. Return loss measurement

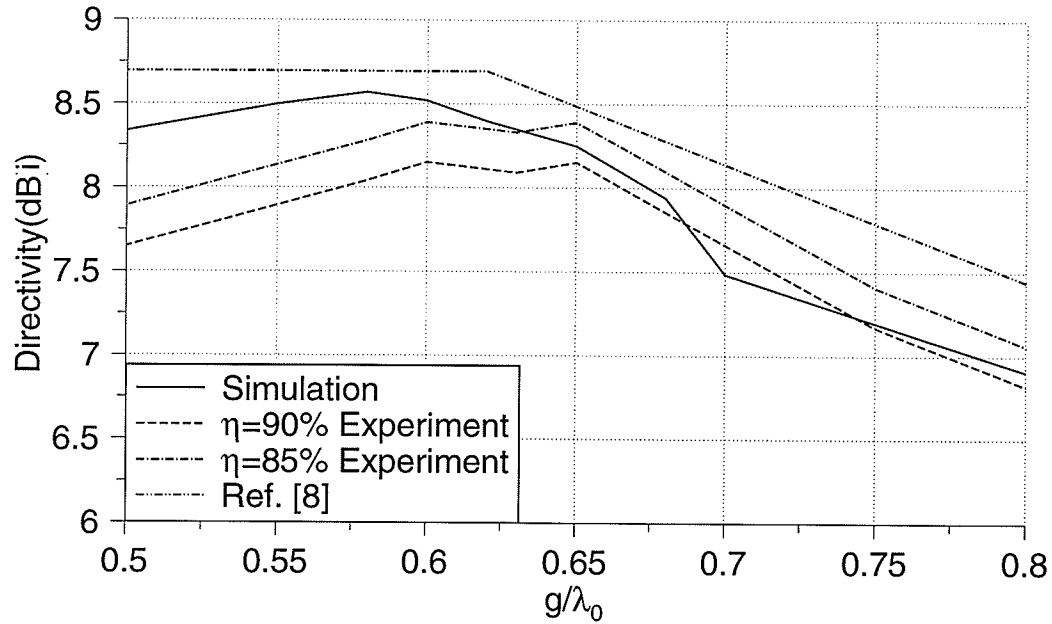


Fig. 3.11. Comparison between simulation and experimental results for directivity

3.4. Effects on the Radiation Pattern

The ground plane radius has pronounced effects on the radiation patterns. For each mode these effects were studied and summarized below,

3.4.1. TM_{11} Mode

Fig. 3.12 shows a few sample results of the radiation patterns. The antenna has a substrate with a permittivity of 2.5. These patterns show that after $g=0.6\lambda_0$, the E-plane peak moves away from boresight toward somewhere between 25° and 37° and a dip appears at $\theta=0^\circ$. The peak angle of the H-plane also moves but with a lesser drop of gain at $\theta=0^\circ$. Fig. 3.13 shows the variation of peak angles. The half power beamwidth (HPBW) also starts increasing after $g=0.6\lambda_0$, but tends to

decrease (Fig. 3.14). The backlobe level increases after g between $0.5\lambda_0$ and $0.6\lambda_0$ and has a periodic behaviour (Fig. 3.15). The difference between the E and H-plane patterns increases after $g=0.7\lambda_0$ and decreases after $g=0.9\lambda_0$ (Fig. 3.16).

All these results show that the beamwidth and peak angle have a similar behaviour as the gain, which is periodic.

3.4.2. TM_{21} Mode

Fig. 3.17 shows samples of radiation patterns for an antenna with $\epsilon_r=4.0$. Fig. 3.18 shows that the E-plane peak angle decreases initially moving toward 35° , increases after $g=0.8\lambda_0$ toward 51° , decreases again after $g=0.9\lambda_0$, and finally increases after $g=1.4\lambda_0$ toward 55° . The H-plane peak angle, also, decreases initially until $g=0.8\lambda_0$. It reaches 35° and then increases until 48° , decreasing again after $g=1.2\lambda_0$.

The E-plane HPBW, in Fig. 3.19, decreases until somewhere around $g=1.3\lambda_0$. At $g=1.4\lambda_0$ there is a peak and HPBW reaches to 49° , after that it decreases again. The H-plane HPBW decreases until $g=0.8\lambda_0$. At $g=0.9\lambda_0$ there is a peak and HPBW is about 49° , after that it decreases again until $g=1.2\lambda_0$, which reaches 35° . After $g=1.2\lambda_0$ it starts increasing toward 55° .

The difference between the E and H-plane peaks starts increasing at $g=0.8\lambda_0$. It becomes as high as 5dB, between $g=1.0\lambda_0$ and $g=1.2\lambda_0$. After that it starts decreasing (Fig. 3.20).

From these results, one can say that $g=0.8\lambda_0$ is a critical point. It is interesting to note that the minimum ground plane radius for having a reasonable gain is $g=0.8\lambda_0$.

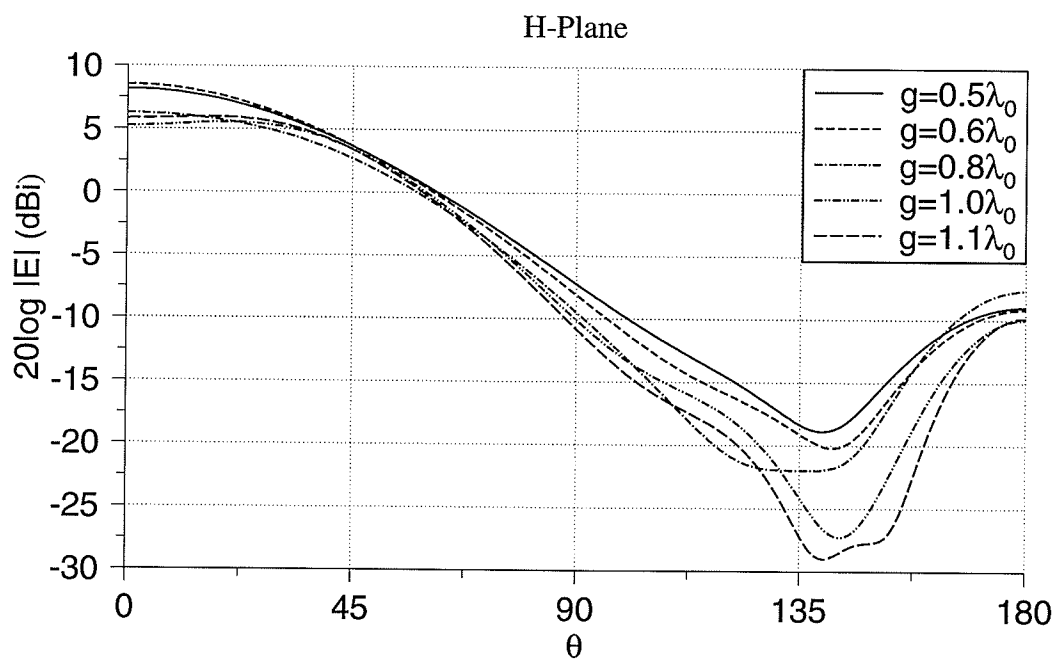
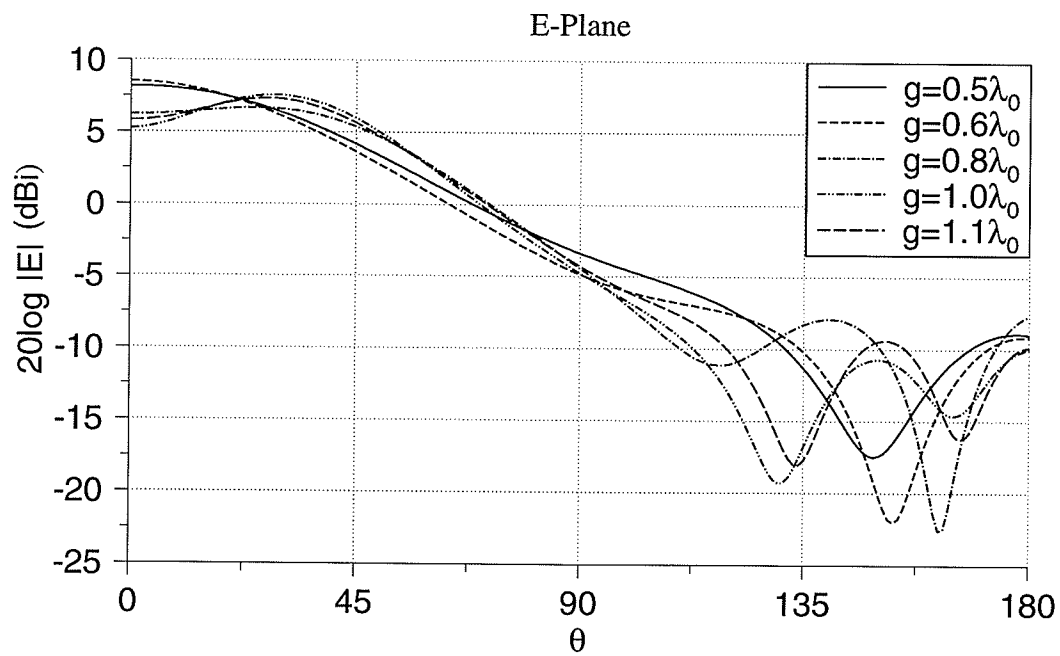


Fig. 3.12. Radiation patterns for TM_{11} mode, $\epsilon_r=2.5$

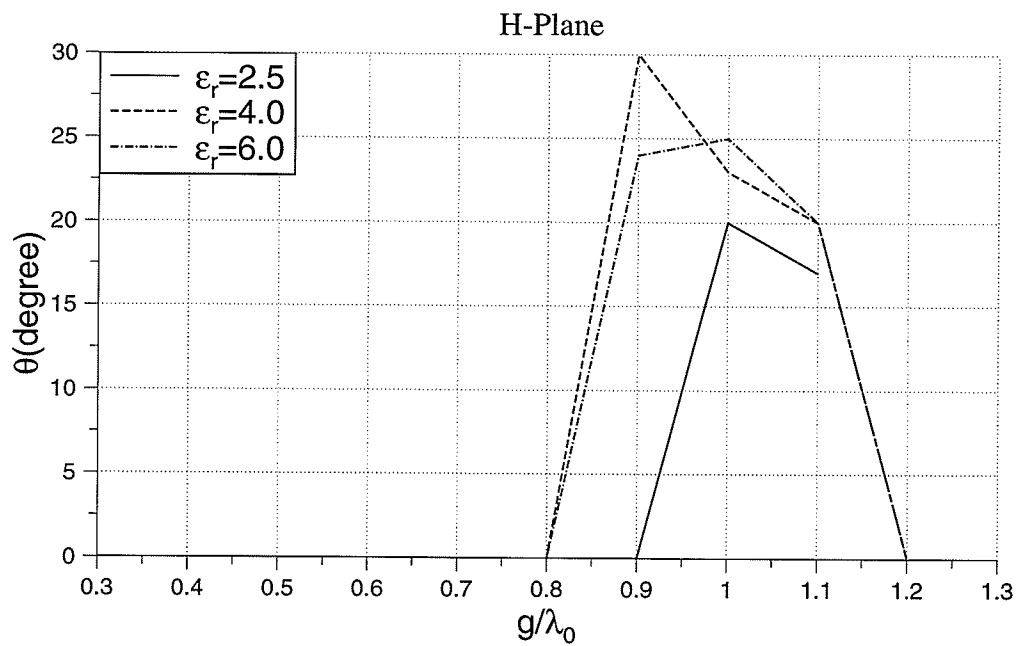
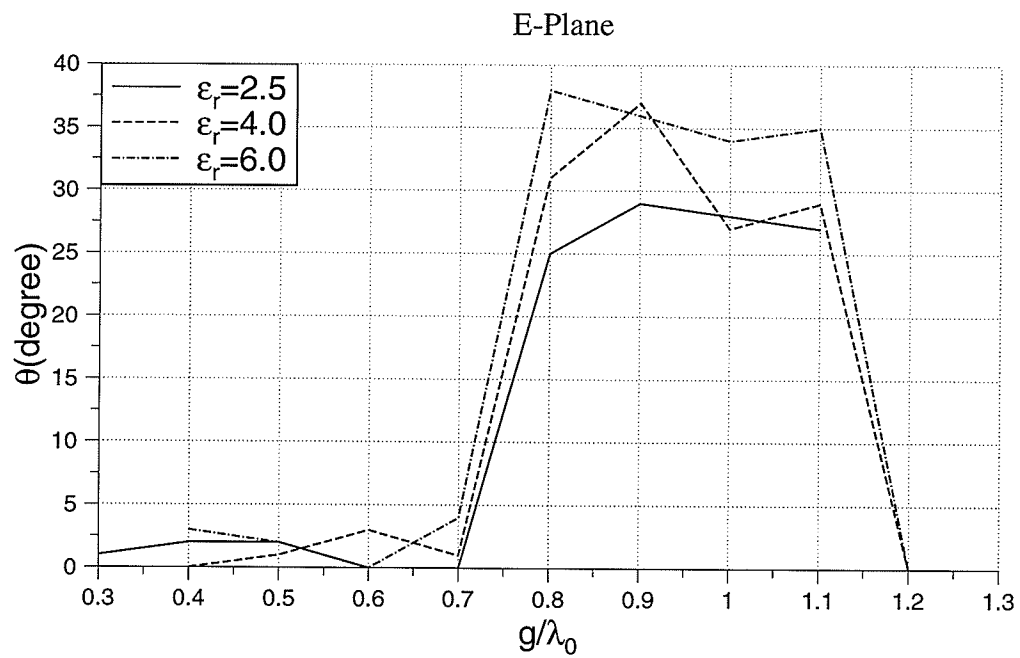


Fig. 3.13. Angle for antenna peak gain for TM_{11} mode

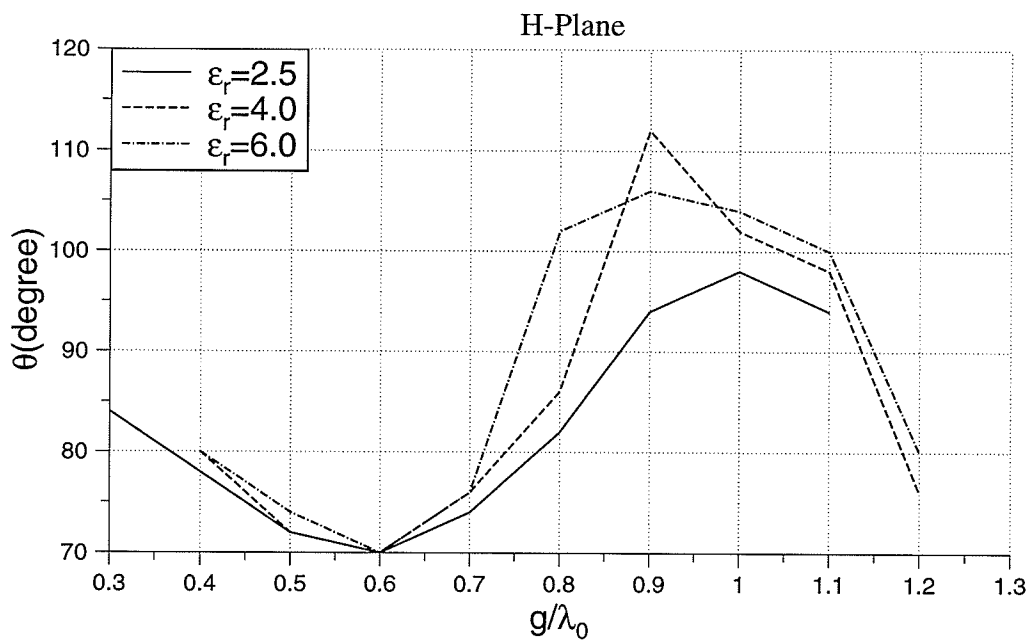
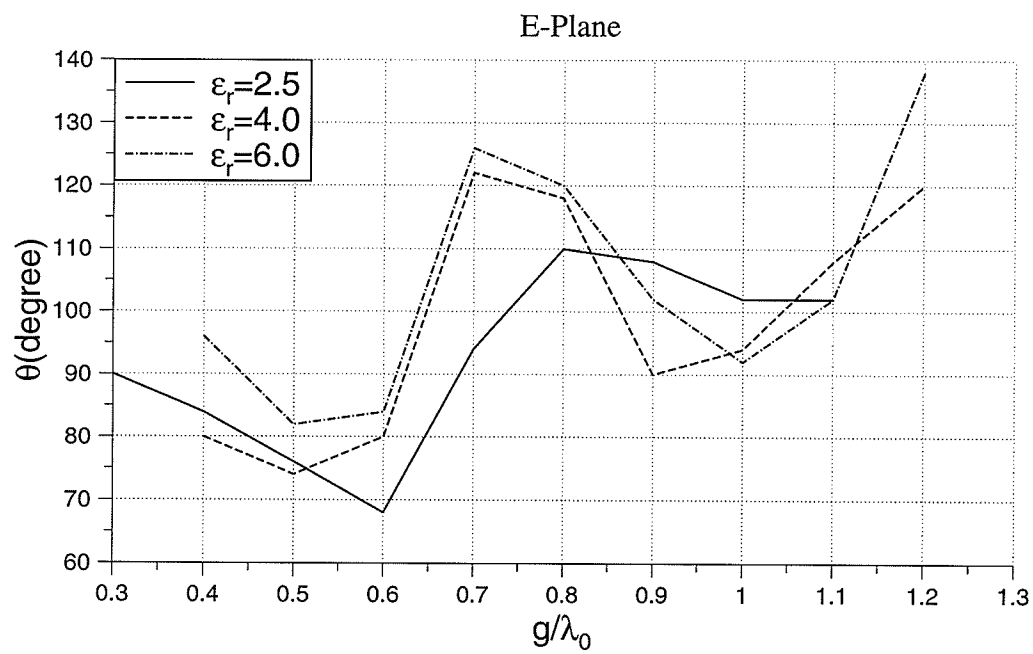


Fig. 3.14. Half power beamwidth for TM_{11} mode

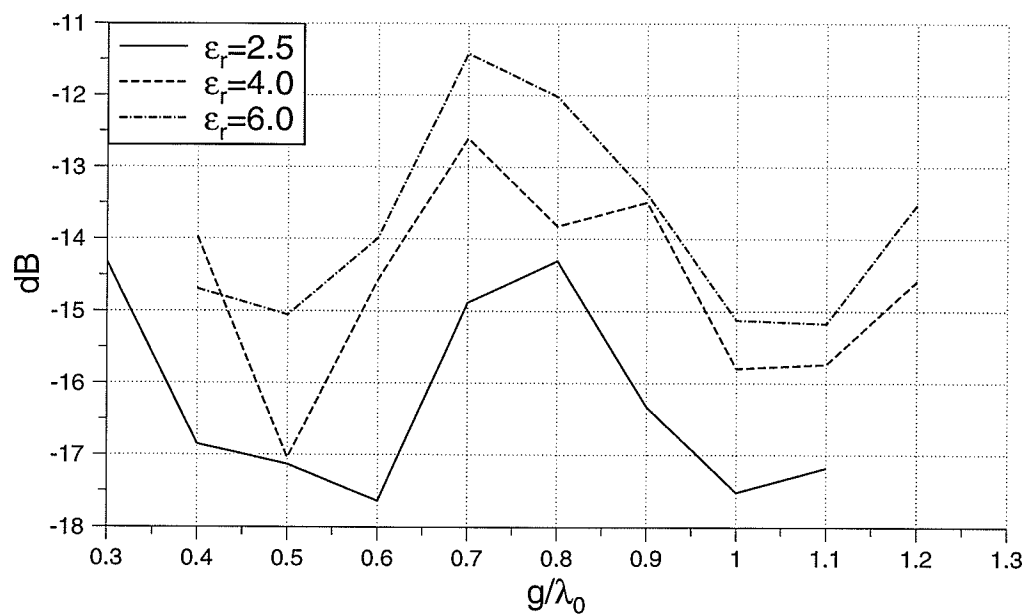


Fig. 3.15. Backlobe level for TM_{11} mode

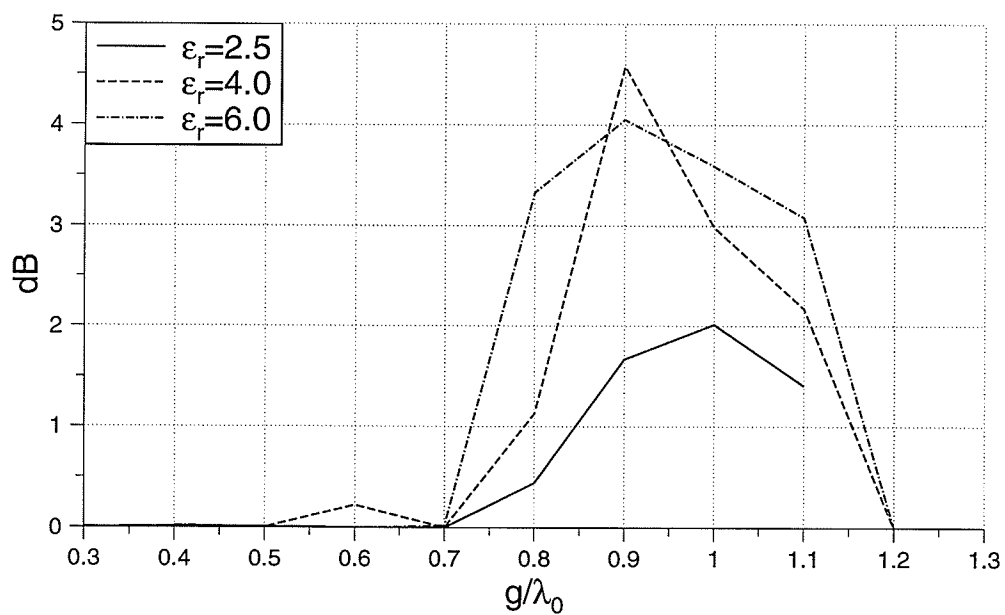


Fig. 3.16. E and H-plane patterns peak difference for TM_{11} mode

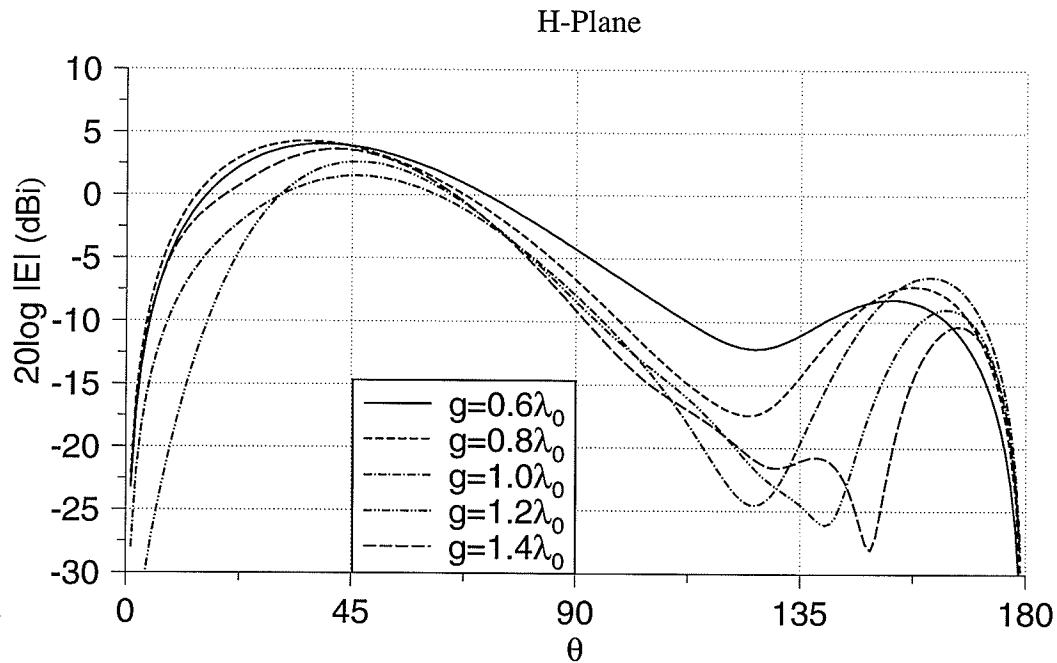
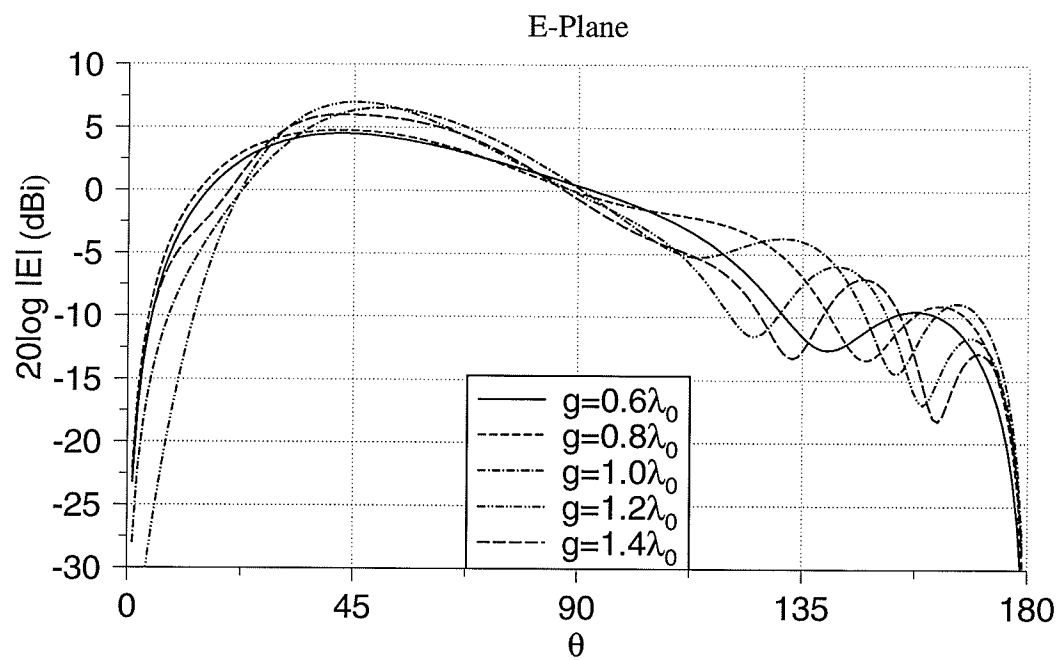


Fig. 3.17. Radiation patterns for TM_{21} mode, $\epsilon_r=4.0$

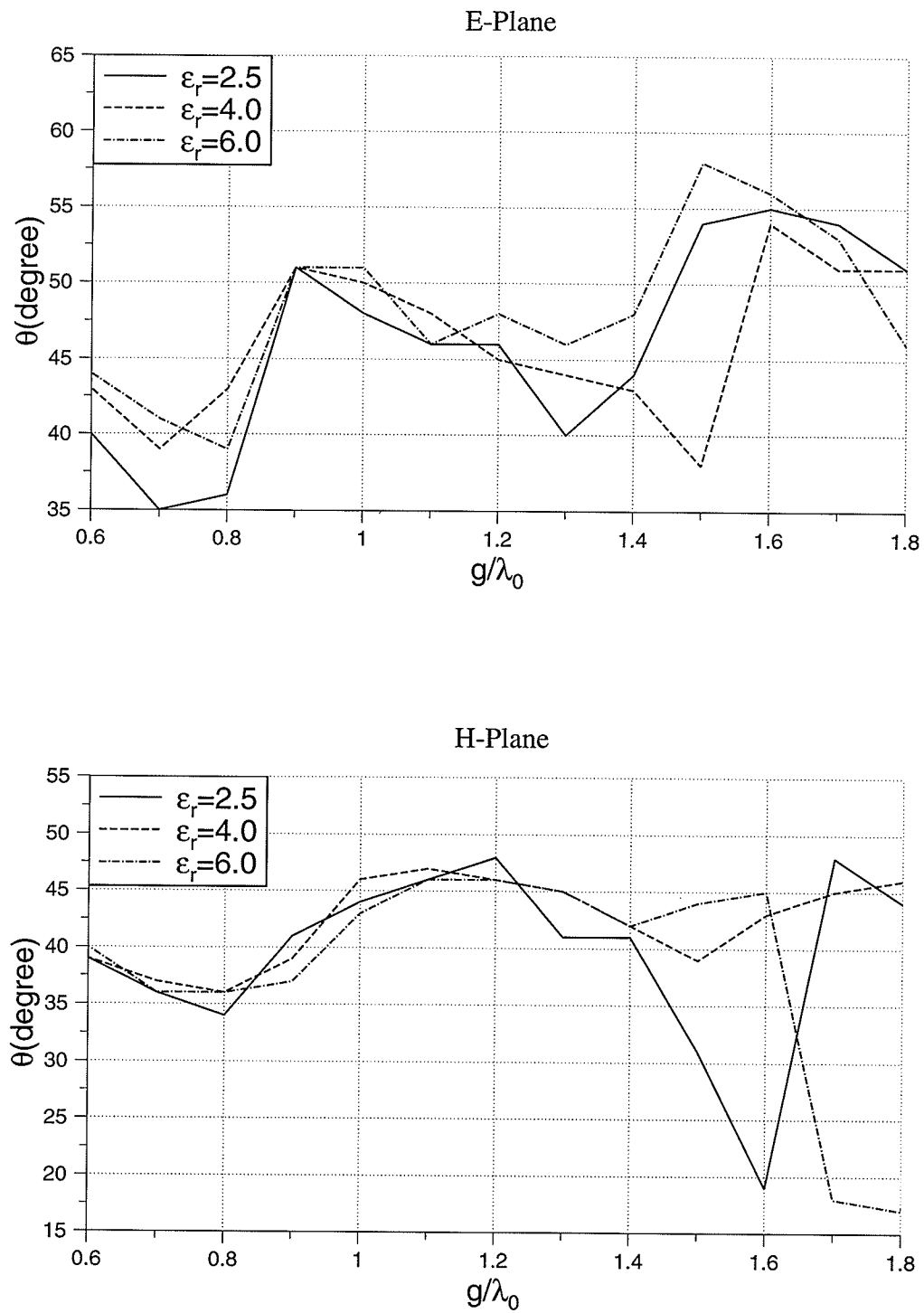


Fig. 3.18. Angle for antenna peak gain for TM_{21} mode

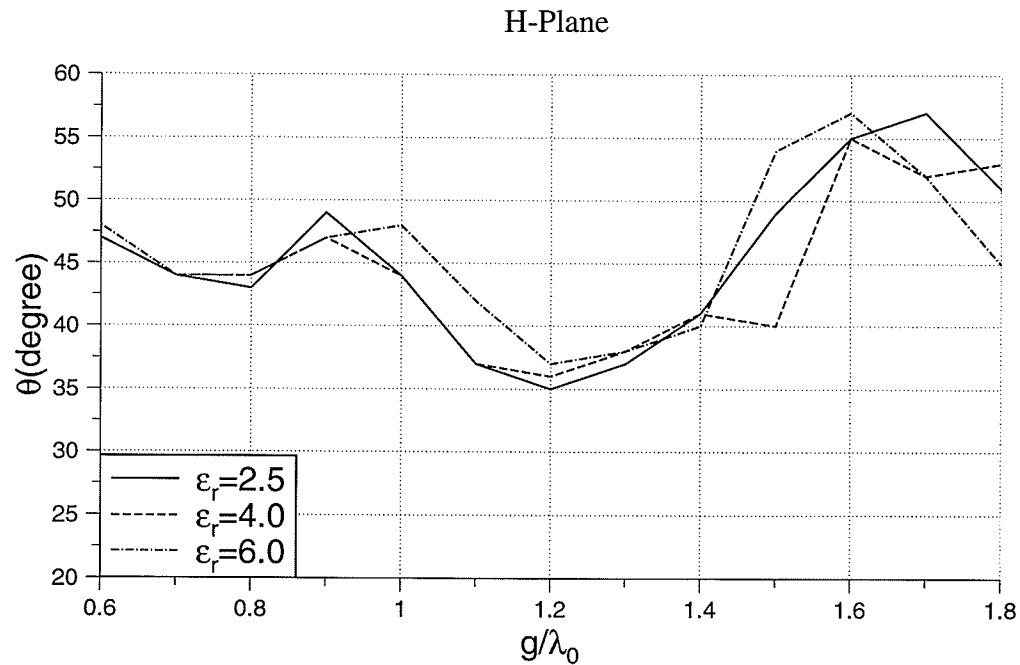
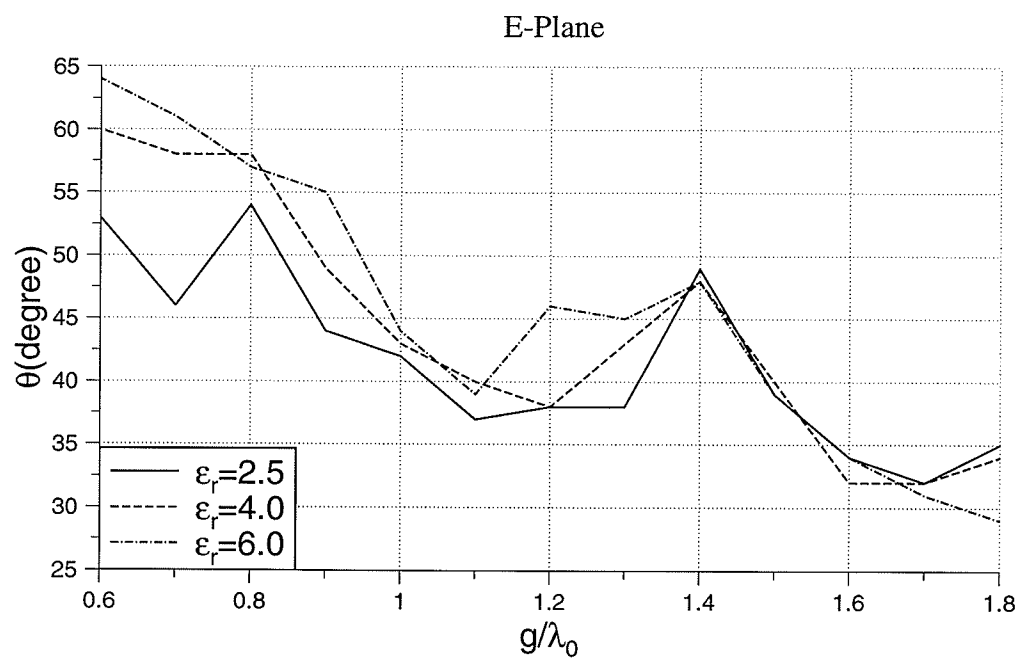


Fig. 3.19. Half power beamwidth for TM_{21} mode

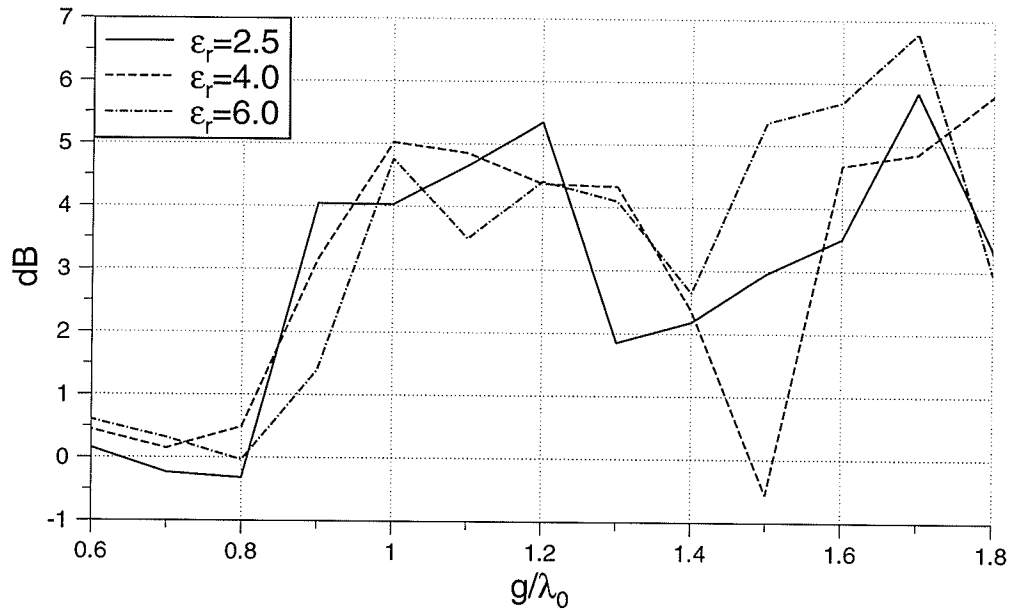


Fig. 3.20. E and H-plane patterns peak difference for TM_{21} mode

3.4.3. TM_{31} Mode

Fig. 3.21 shows the radiation patterns of an antenna with $\epsilon_r=6.0$. The E-plane peak angle decreases from 60° to around 50° , and then somewhere between $g=0.5\lambda_0$ and $g=0.6\lambda_0$ it starts increasing. The H-plane peak angle decreases until $g=1.0\lambda_0$ and then increases. At $g=1.2\lambda_0$ it has a peak. Again it decreases toward 50° (Fig. 3.22).

The E-plane HPBW increases initially. After $g=0.8\lambda_0$ it decreases. The H-plane HPBW decreases until $g=1.4\lambda_0$ and reaches 32° , then increases (Fig. 3.23). The peak difference of the E and H-plane patterns starts increasing after $g=1.2\lambda_0$. Its peak occurs at $1.3\lambda_0$ and then it decreases (Fig. 3.24).

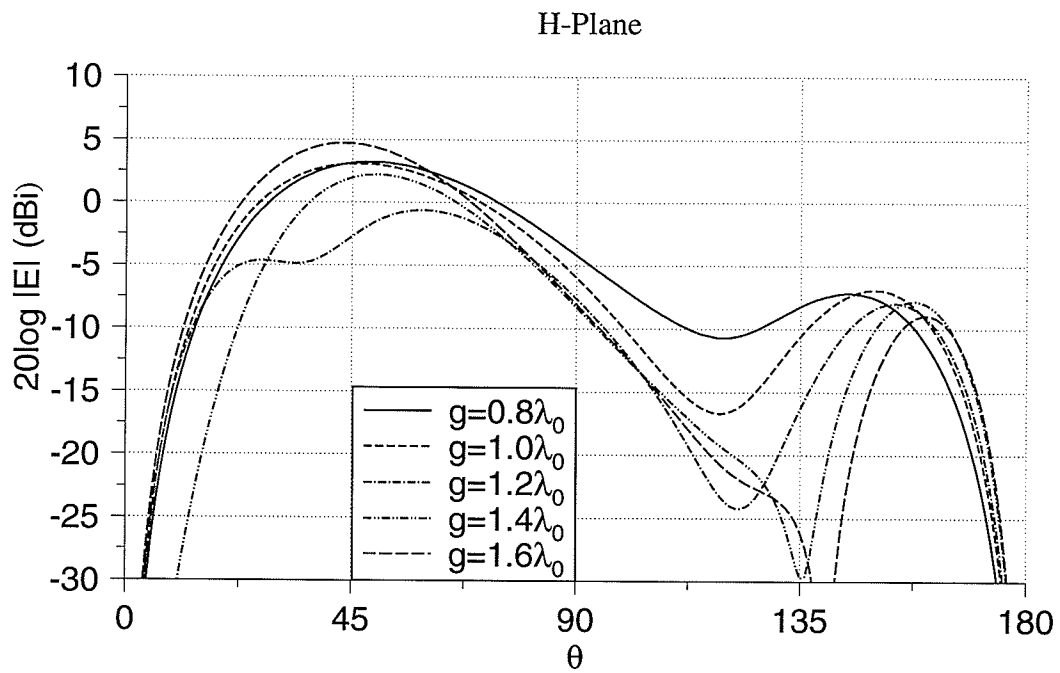
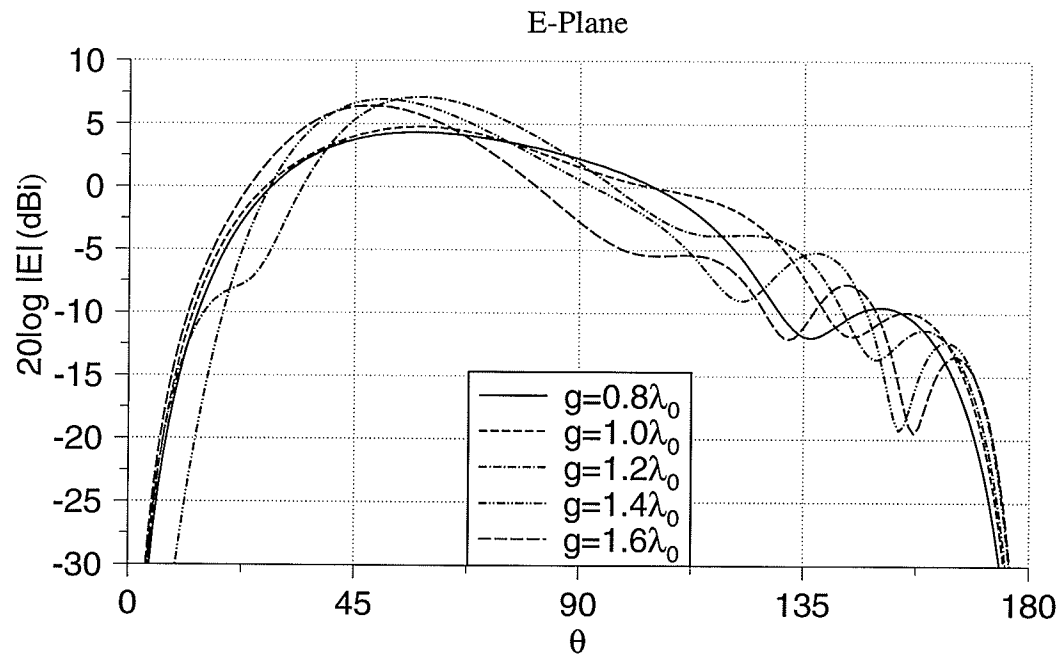


Fig. 3.21. Radiation patterns for TM_{31} mode, $\epsilon_r=6.0$

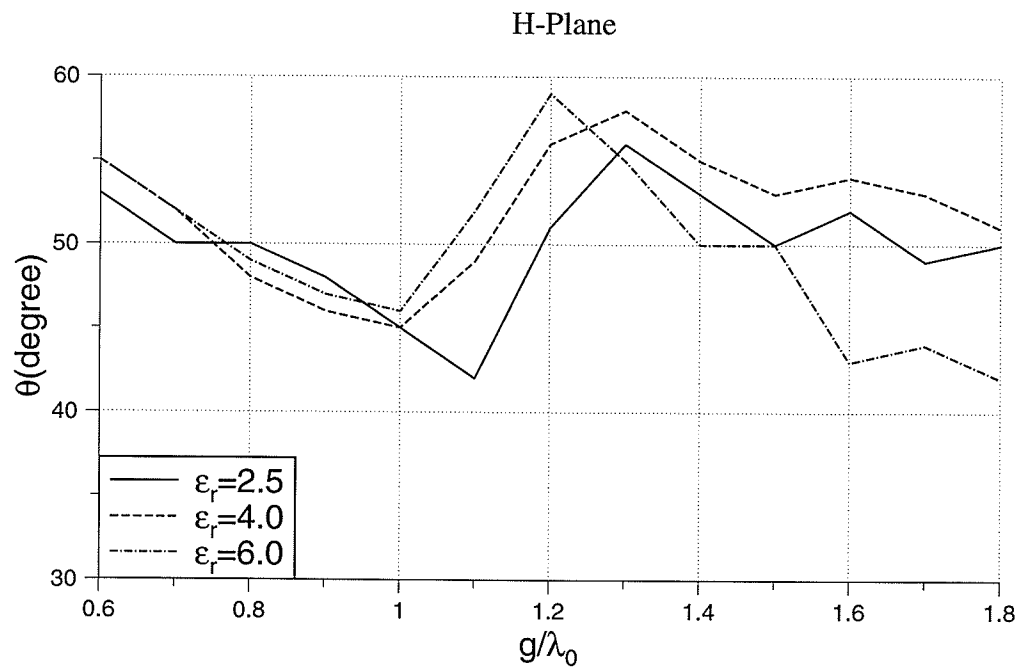
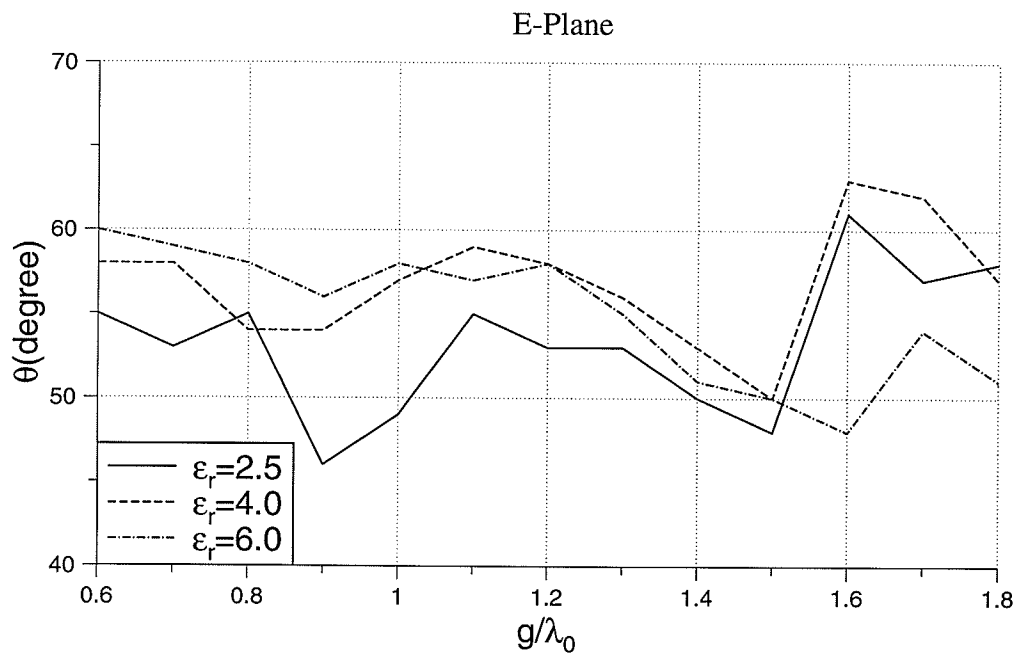


Fig. 3.22. Angle for antenna peak gain for TM_{31} mode

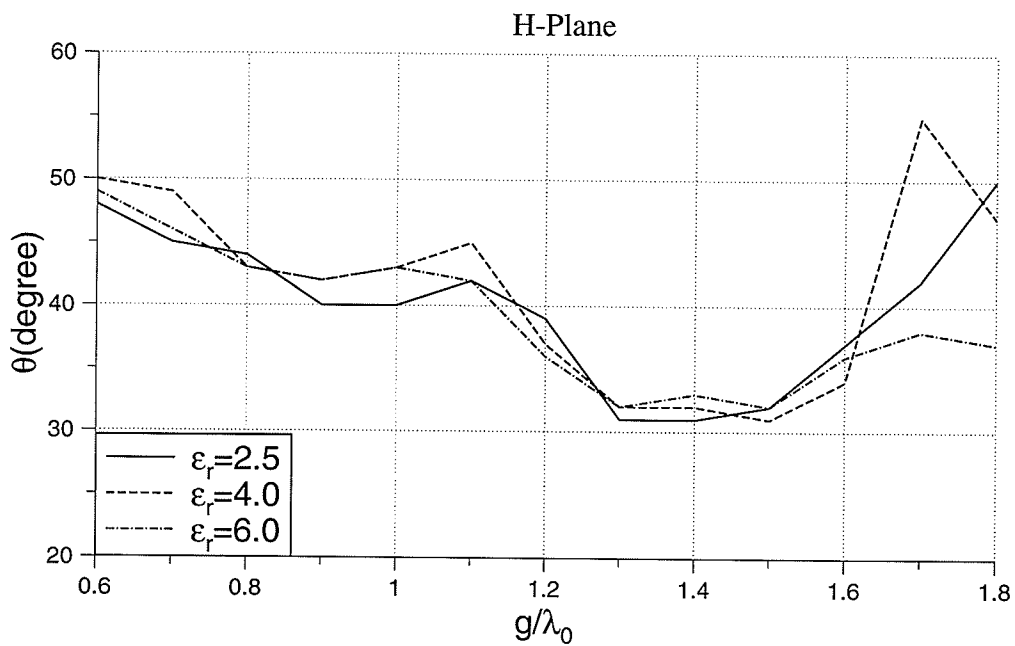
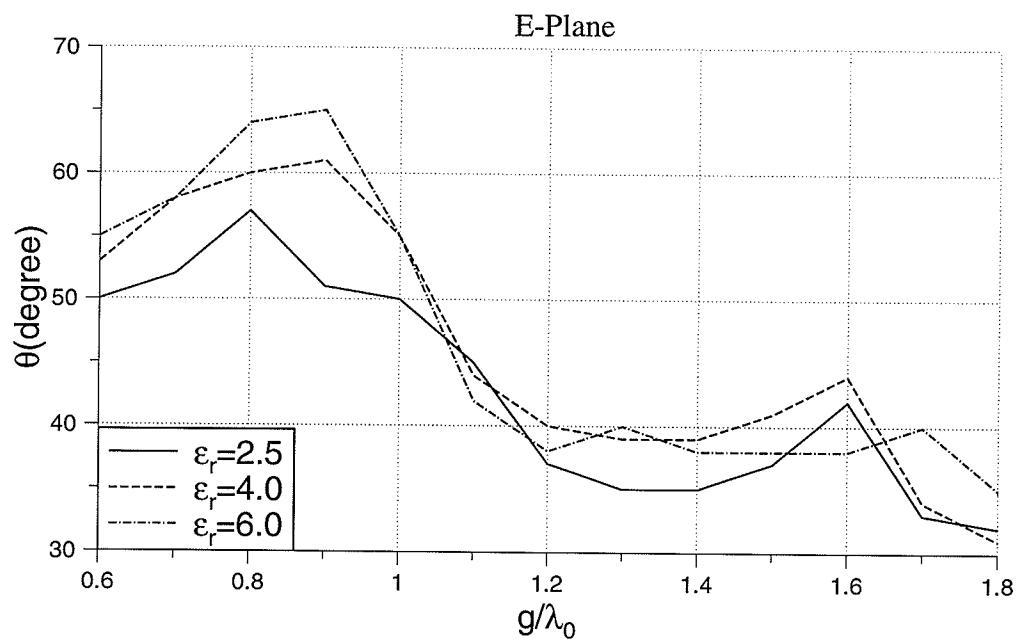


Fig. 3.23. Half power beamwidth for TM_{31} mode

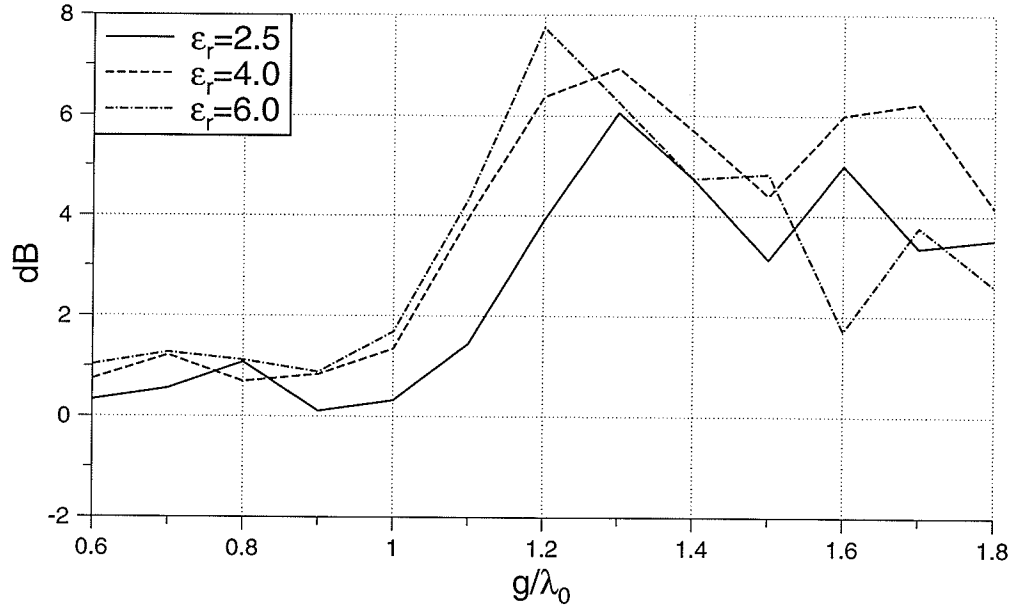


Fig. 3.24. E and H-plane patterns peak difference for TM_{31} mode

3.4.4. TM_{41} Mode

Radiation patterns for antenna with $\epsilon_r=2.5$ are shown in Fig. 3.25. Figs. 3.26 to 3.28 show the variation of the peak angles, HPBW's and the E and H-plane patterns peak difference. The E-plane peak angle oscillates between 50° and 60° . The H-plane peak angle decreases until $g=1.2\lambda_0$ and then increases. Its value is between 45° and 65° .

HPBW of the E-plane increases until $g=1.1\lambda_0$ then decreases. The H-plane HPBW decreases until $g=1.2\lambda_0$ and then peaks at $g=1.3\lambda_0$. After that it decreases.

The backlobe level starts increasing at $g=1.2\lambda_0$, and becomes as high as 7.5dB at $g=1.4\lambda_0$.

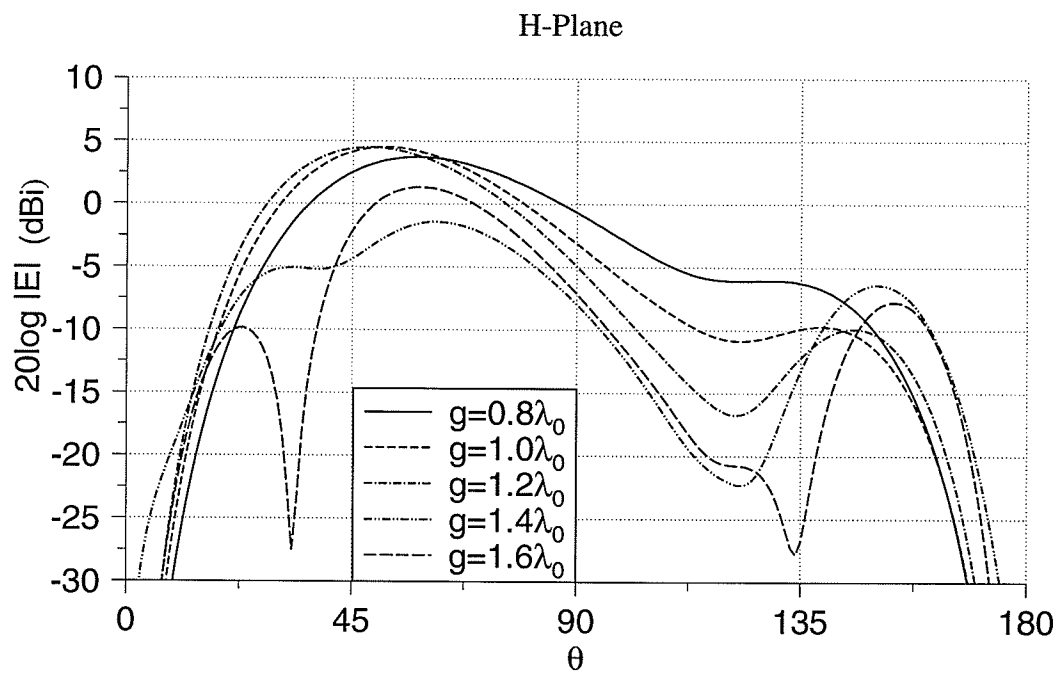
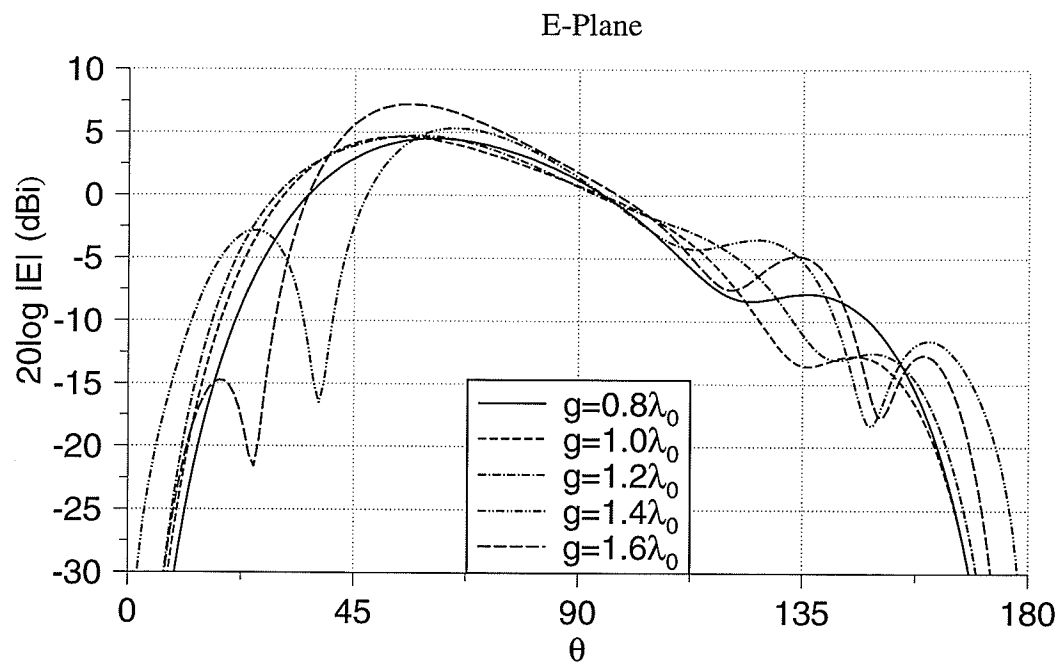


Fig. 3.25. Radiation patterns for TM_{41} mode, $\epsilon_r=2.5$

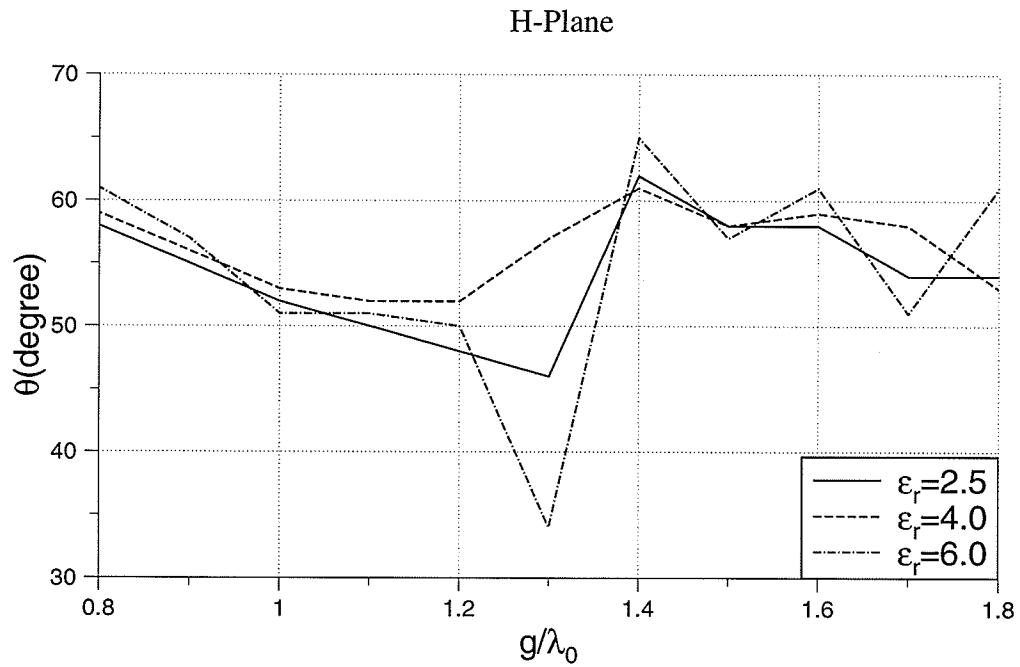
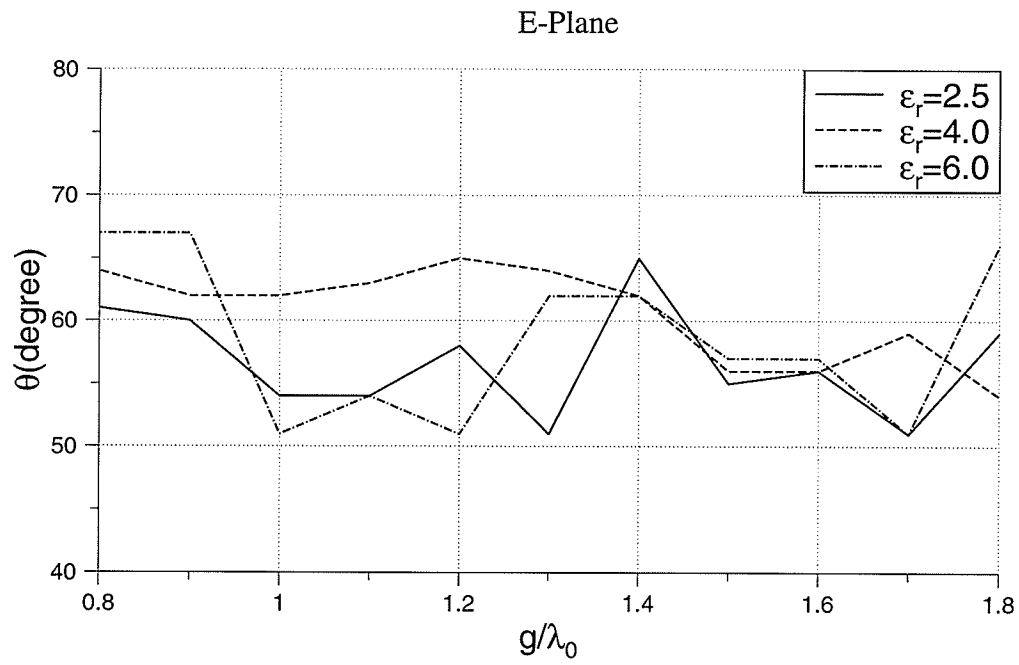


Fig. 3.26. Angle for antenna peak gain for TM_{41} mode

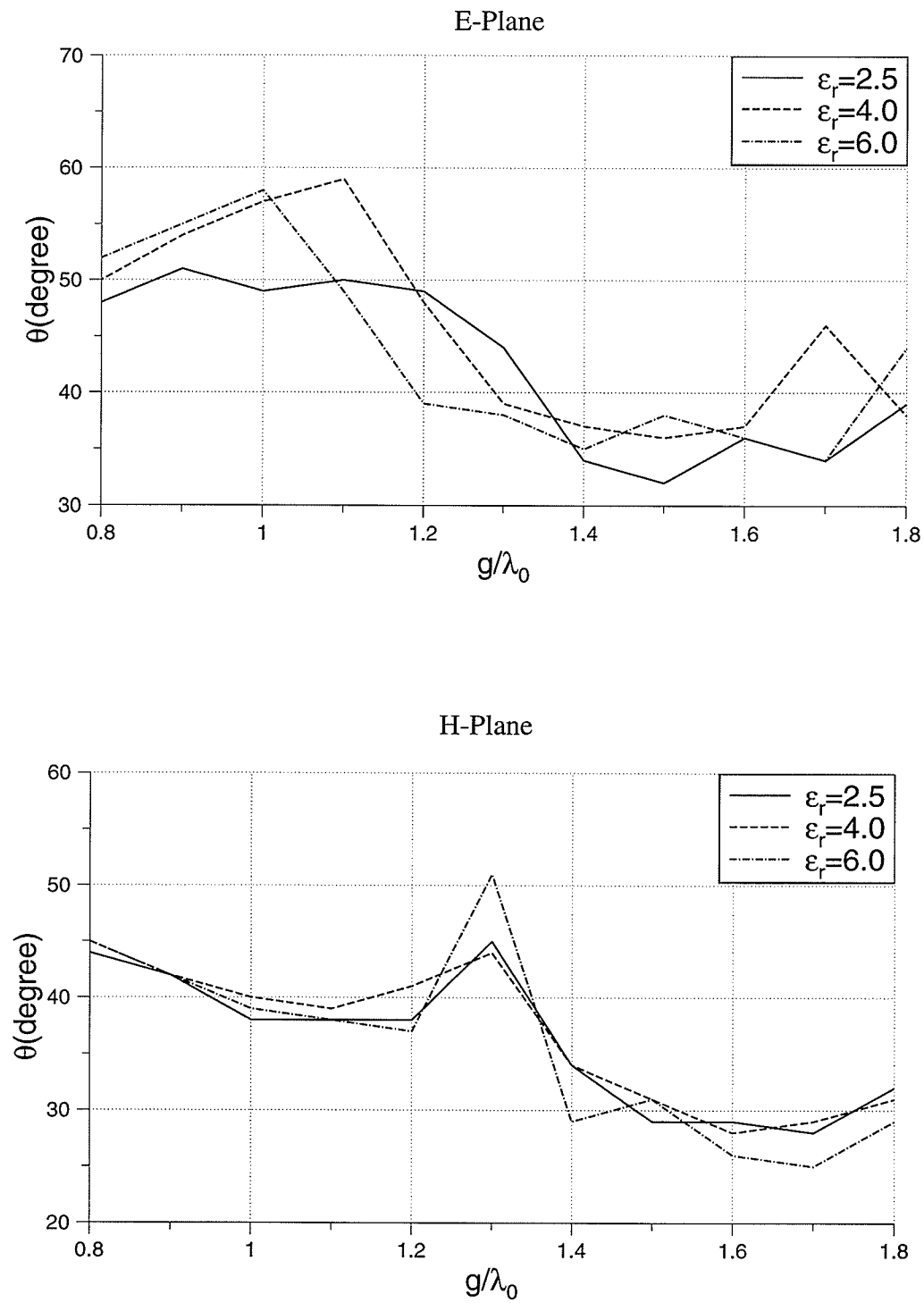


Fig. 3.27. Half power beamwidth for TM_{41} mode

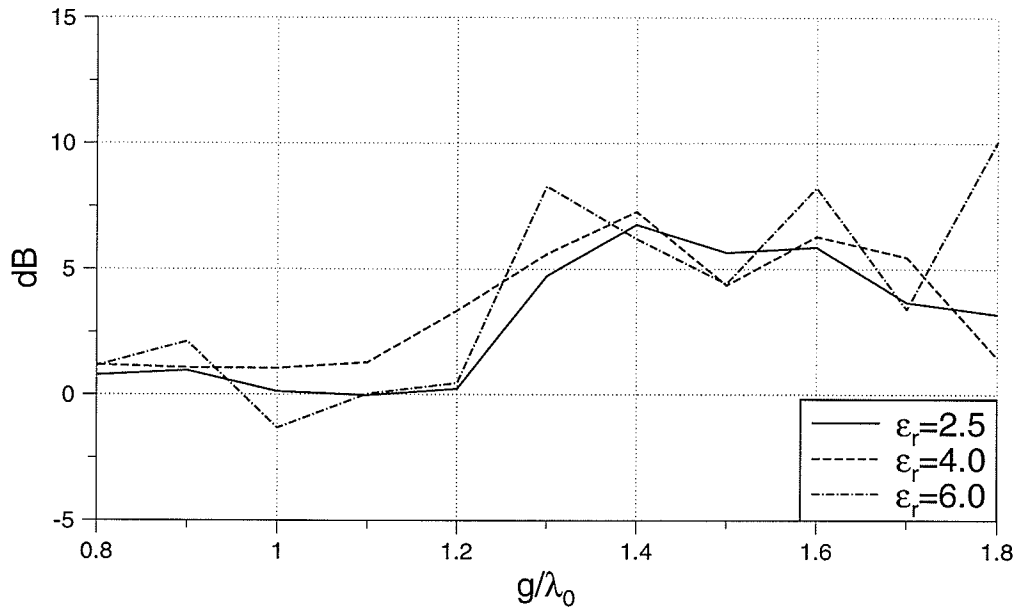


Fig. 3.28. *E* and *H*-plane patterns peak difference for TM_{41} mode

3.4.5. Experimental Results

Figs. 3.29 and 3.30 show the comparison between simulation and measurement of radiation patterns of samples antennas. The antennas have the same parameters as Table (3-10). They show good agreement between theory and experiment. One should consider the fact that the accuracy of MBES package is limited to small permittivities. Also as the ground plane size increases, the numerical solution requires large computation time and the accuracy deteriorates.

THE UNIVERSITY OF MANITOBA
Circular patch, 11.3cm diameter ground plane

File: DISC113.DAT
Frequency : 3.260

ANGLE (R) : See L

Date: 08-Feb-96 12:36
ANGLE (P) : 0.1 Deg

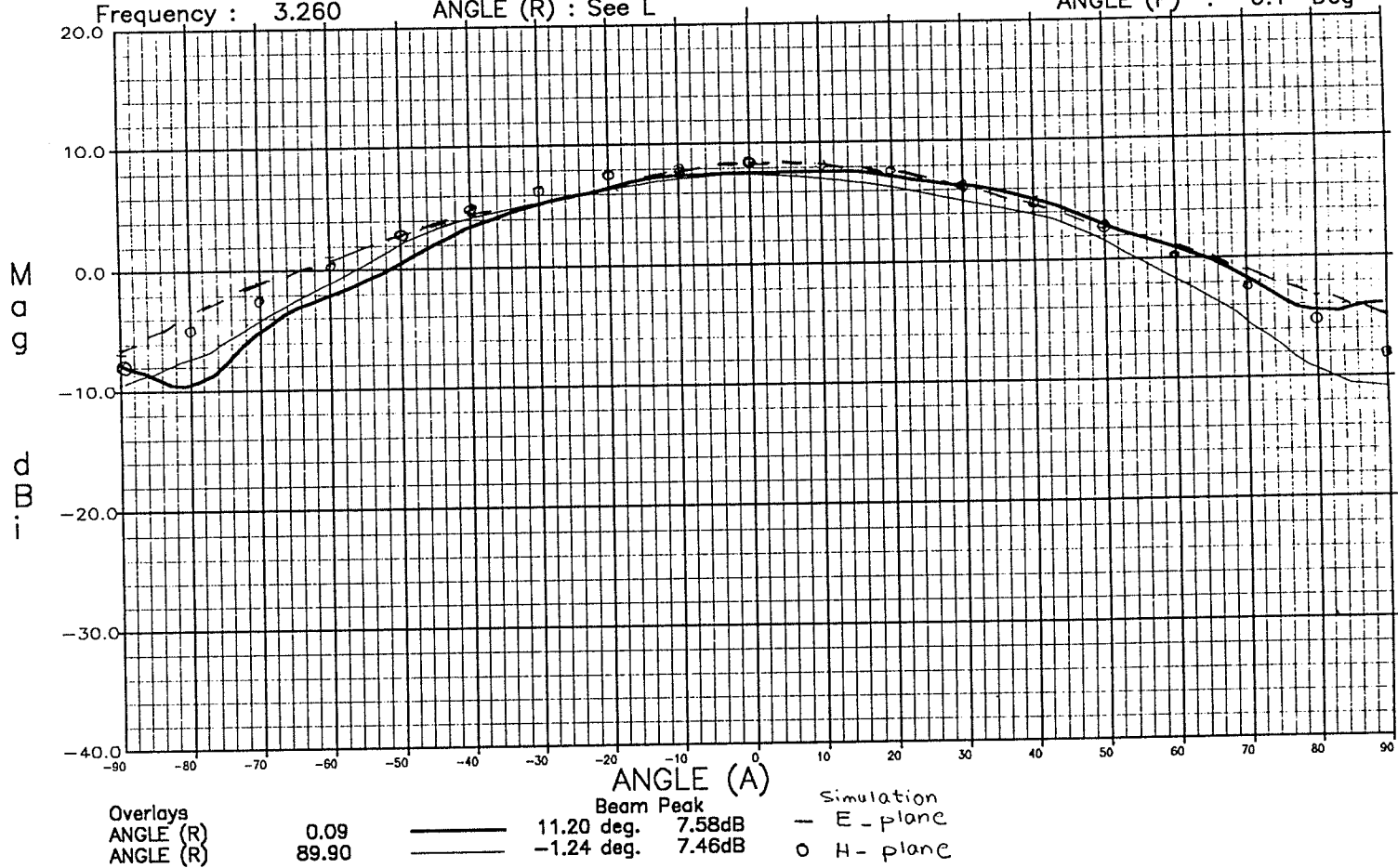


Fig. 3.29. Radiation pattern measurement for $g=0.6\lambda_0$

THE UNIVERSITY OF MANITOBA
Circular patch, 20.7cm diameter ground plane

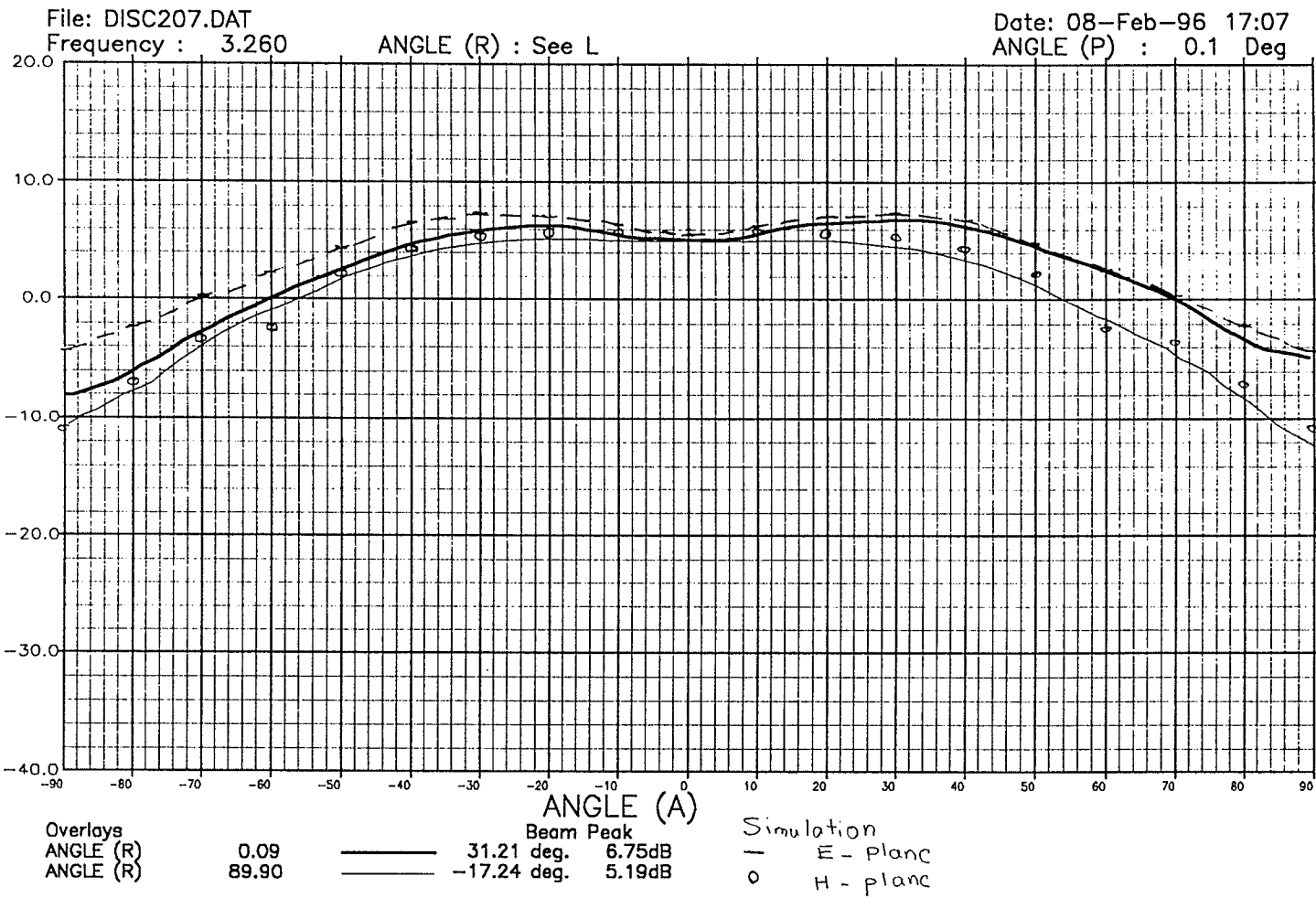


Fig. 3.30. Radiating pattern measurement for $g=1.1\lambda_0$

3.5. Effects on Circular Polarization

In some applications the antenna is required to radiate circular polarization over a wide angle. In microstrip antennas circular polarization can be obtained by exciting two modes which are at phase quadrature in time and space. In such a case it is necessary to shape antenna principal plane patterns to become nearly equal in a large sector of the radiation zone.

With certain sizes of ground plane, the H-plane beamwidth decreases, but the E-plane beamwidth does not change as much. This means that the equality of E and H-plane patterns can be improved by choosing the proper ground plane size.

The axial ratio (AR) was chosen as parameter to measure the equality of the E and H-plane patterns.

3.5.1. Axial Ratio and Polarization Ratio

The instantaneous electric field associated with a general plane wave travelling in the \hat{r} direction can be decomposed into $\hat{\phi}$ and $\hat{\theta}$ components. Each of these components is expressed as:

$$\begin{aligned} E_{\phi} &= E_1 \cos (\omega t - kz) \\ E_{\theta} &= E_2 \cos (\omega t - kz + \delta) \end{aligned} \quad (3-3)$$

where E_1 and E_2 are amplitudes of instantaneous electric fields in the $\hat{\phi}$, $\hat{\theta}$ directions, ω is the radian frequency, $k = 2\pi/\lambda$ is the phase constant and δ is the phase by which the $\hat{\theta}$ component leads the $\hat{\phi}$ component of electric field.

The polarization ellipse is the locus of points formed by the tip of the instantaneous electric field vector (Fig. 3.31). The polarization ellipse can have any shape (axial ratio) and orientation (tilt). The axial ratio (AR) of the polarization ellipse quantifies the shape of the ellipse (equation (3-4)). Different polarization are represented in Table (3-12).

$$AR = \frac{\text{Major axis length}}{\text{Minor axis length}} = \frac{|E_{max}|}{|E_{min}|} \quad (3-4)$$

$$1 < |AR| < \infty$$

$$AR (dB) = 20 \log |AR|$$

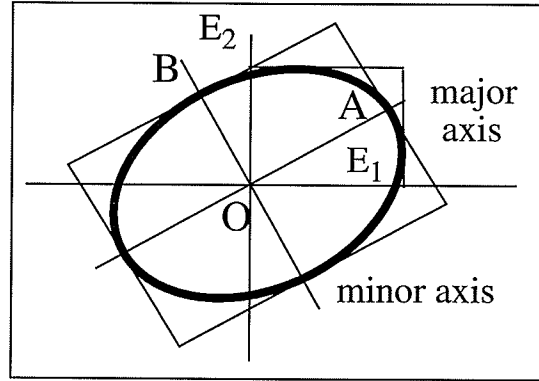


Fig. 3.31. Polarization ellipse

Table (3-12) Representation of polarization states

Polarization state	E_1	E_2	δ	AR
Linear horizontal	1	0	NA	∞
Linear vertical	0	1	NA	∞
Left-hand circular (LHCP)	$1/\sqrt{2}$	$1/\sqrt{2}$	90°	-1
Right-hand circular (RHCP)	$1/\sqrt{2}$	$1/\sqrt{2}$	-90°	1

Any polarization state can be represented as a linear combination of orthogonal states. A left-hand circularly polarized wave is given by:

$$\begin{aligned} \vec{E}_L(t) &= [E_{L0} \cos \omega t \hat{\phi} + E_{L0} \cos (\omega t + 90^\circ) \hat{\theta}] / \sqrt{2} \\ &= \frac{E_{L0}}{\sqrt{2}} [\cos \omega t \hat{\phi} - \sin \omega t \hat{\theta}] \end{aligned} \quad (3-5)$$

Similarly for right-hand circular polarization is given by:

$$\vec{E}_R(t) = \frac{E_{R0}}{\sqrt{2}} [\cos(\omega t + \delta') \hat{\phi} - \sin(\omega t + \delta') \hat{\theta}] \quad (3-6)$$

The polarization ratio is a single complex number that represents polarization state of a wave.

The definition of polarization ratio is:

$$\rho_L = \frac{E_\theta}{E_\phi} = \frac{E_2}{E_1} e^{j\delta} \quad (3-7)$$

For LHCP $\rho_L = j$ and for RHCP $\rho_L = -j$. Fig. 3.32 shows relationship between AR and polarization ratio. For circular polarization ρ_C can be defined as:

$$\rho_C = \frac{E_R}{E_L} \quad (3-8)$$

where E_R and E_L are the phasor circular polarization components [17].

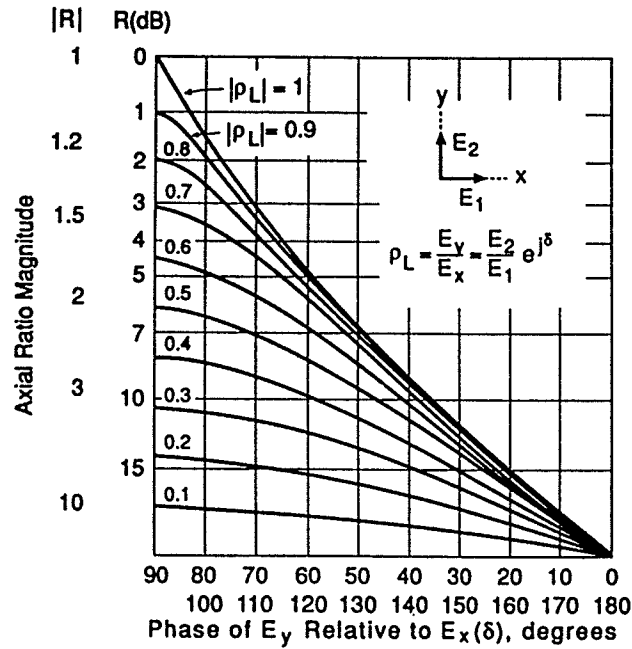


Fig. 3.32. Relationship between axial ratio and polarization ratio

$$E_L = \frac{E_{L0}}{\sqrt{2}} (E_1 - jE_2^{j\delta}) \quad (3-9)$$

$$E_R = \frac{E_{R0}}{\sqrt{2}} (E_1 + jE_2^{j\delta})$$

$$\rho_C = \frac{1 + j\frac{E_2}{E_1}e^{j\delta}}{1 - j\frac{E_2}{E_1}e^{j\delta}} = \frac{1 + j\rho_L}{1 - j\rho_L} \quad (3-10)$$

$$AR = \frac{E_{R0} + E_{L0}}{E_{R0} - E_{L0}} = \frac{|\rho_C| + 1}{|\rho_C| - 1}$$

The program written for the gain and axial ratio calculation, is listed in Appendix B.

3.5.2. Simulation Results

TM₁₁ Mode- Figs. 3.33 to 3.35 show the axial ratio for the TM₁₁ mode and for different substrate permittivities. At $\theta=0^\circ$, the E and H-plane patterns have exactly the same values which means the polarization can be circular and $|AR| = 1$. As the angle increases AR increases and polarization becomes elliptical. Polarization ellipticity increases for larger ground planes, but for larger ground plane radii, circular polarization improves between $\theta=0^\circ$ and 45° . The results also show that the axial ratio depends on the substrate permittivity.

TM₂₁ Mode- For all patterns, there is a null at $\theta=0^\circ$, so the axial ratio is equal to 1 at this angle. As the TM₁₁ mode, the axial ratio increases as the angle θ increases. For small ground planes, the AR has an increasing shape, but for larger ground planes, it starts to improve for a certain angular range (22.5° and 45°) (Figs. 3.36 to 3.38). For $\epsilon_r=2.5$ and $g=1.6\lambda_0$, at 36° , it is equal to 1.03, which means that the polarization is almost circular for this angle.

TM₃₁ and TM₄₁ Modes- These modes have similar behaviour as the TM₂₁ mode, except that the polarization becomes almost linear around $\theta=22.5^\circ$ for TM₃₁ and $\theta=33^\circ$ for TM₄₁ mode. The

polarization sense changes in these regions. The exact location of each region depends on the substrate permittivity. Figs. 3.39 and 3.40 show two samples of the axial ratio for these modes.

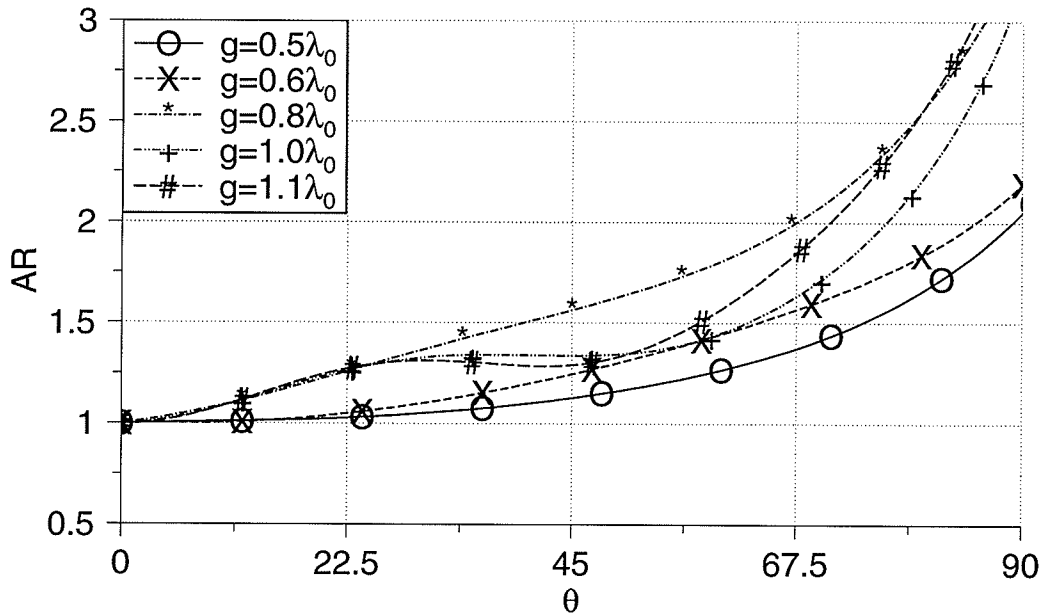


Fig. 3.33. Axial ratio for TM_{11} mode, $\epsilon_r=2.5$

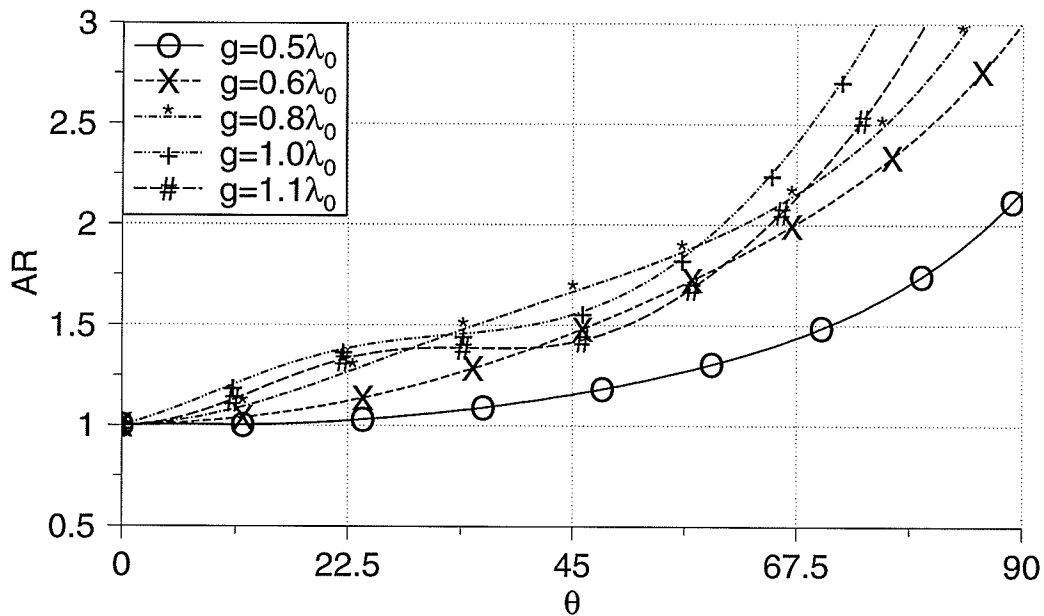


Fig. 3.34. Axial ratio for TM_{11} mode, $\epsilon_r=4.0$

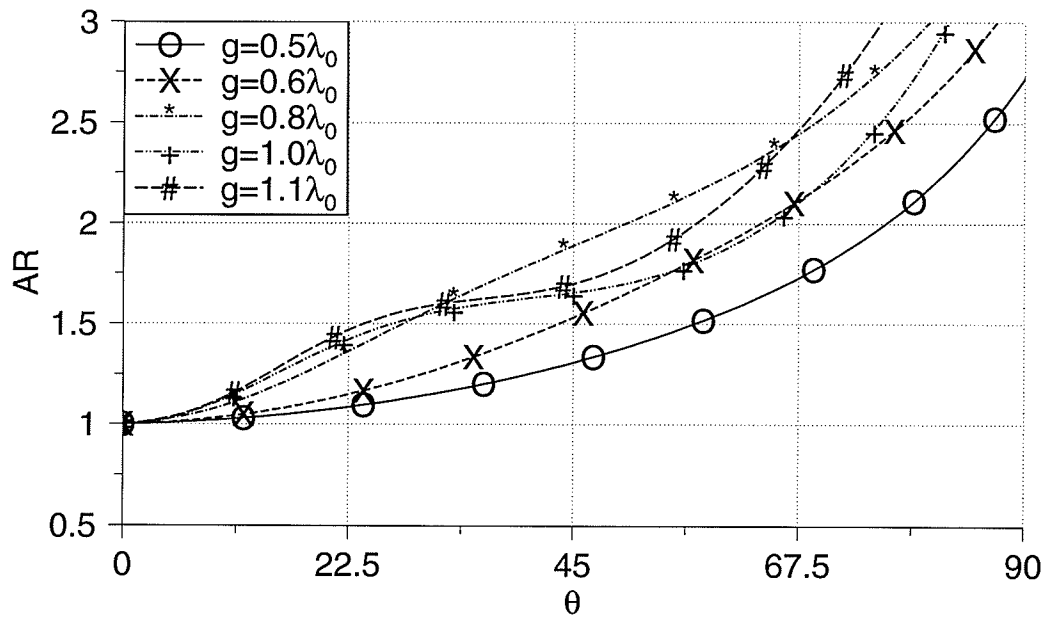


Fig. 3.35. Axial ratio for TM_{11} mode, $\epsilon_r = 6.0$

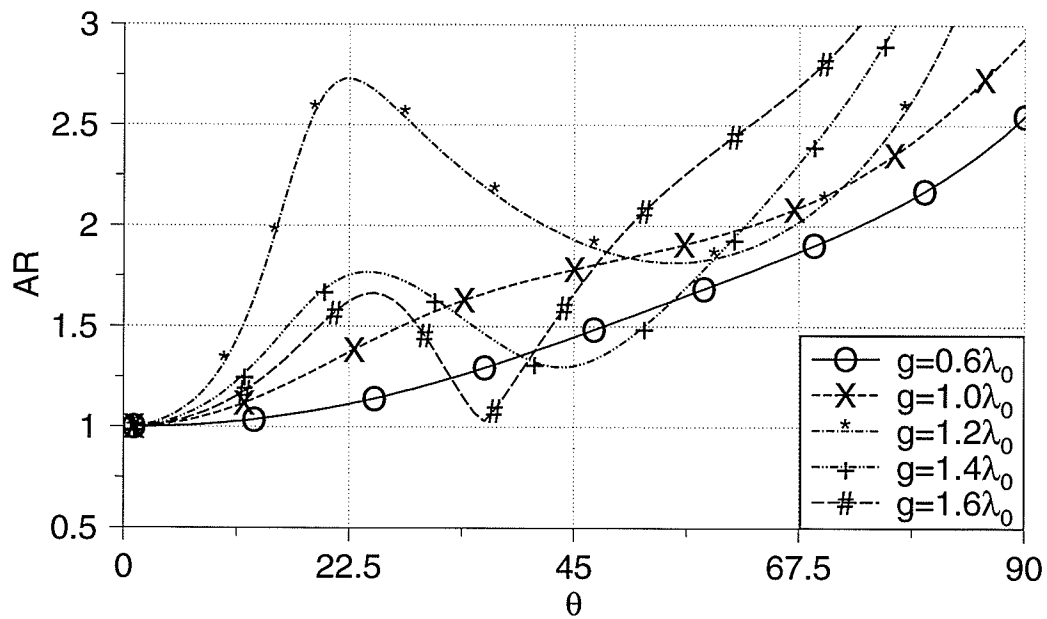


Fig. 3.36. Axial ratio for TM_{21} mode, $\epsilon_r = 2.5$

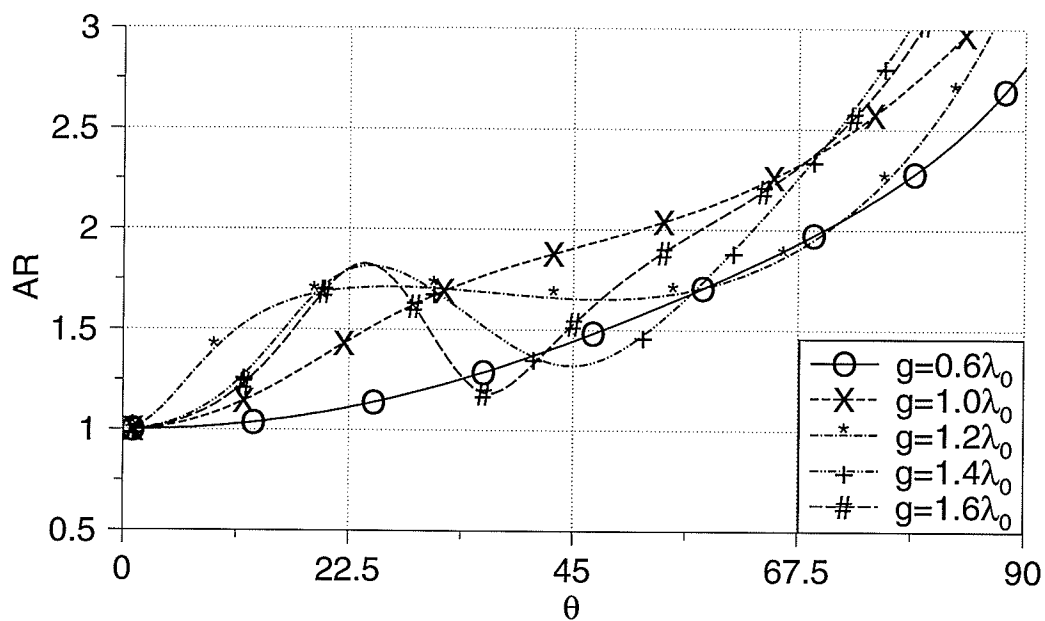


Fig. 3.37. Axial ratio for TM_{21} mode, $\epsilon_r=4.0$

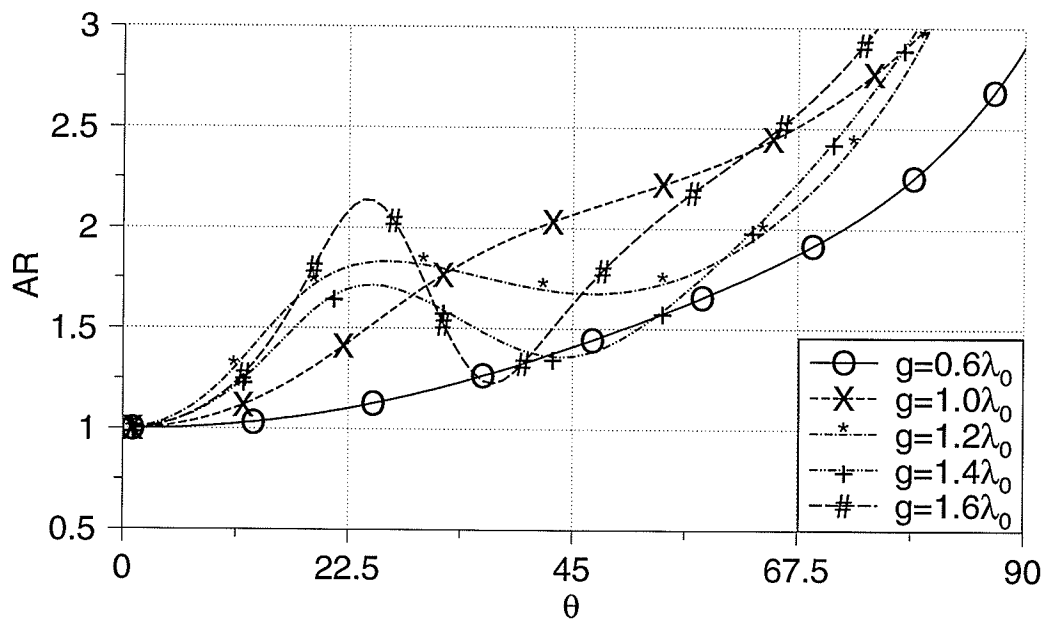


Fig. 3.38. Axial ratio for TM_{21} mode, $\epsilon_r=6.0$

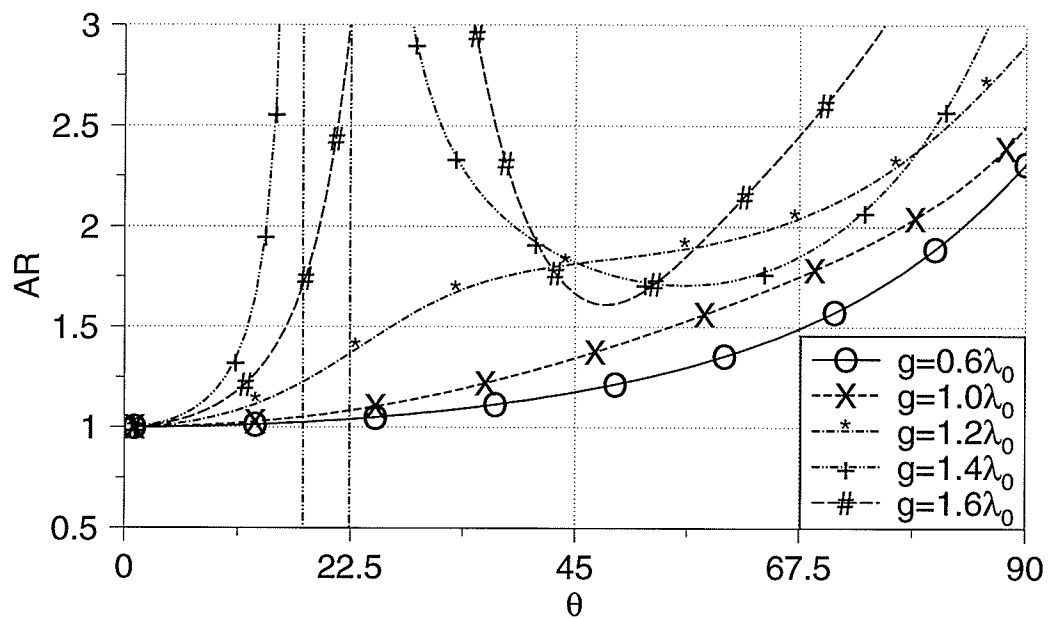


Fig. 3.39. Axial ratio for TM_{31} mode, $\epsilon_r=2.5$

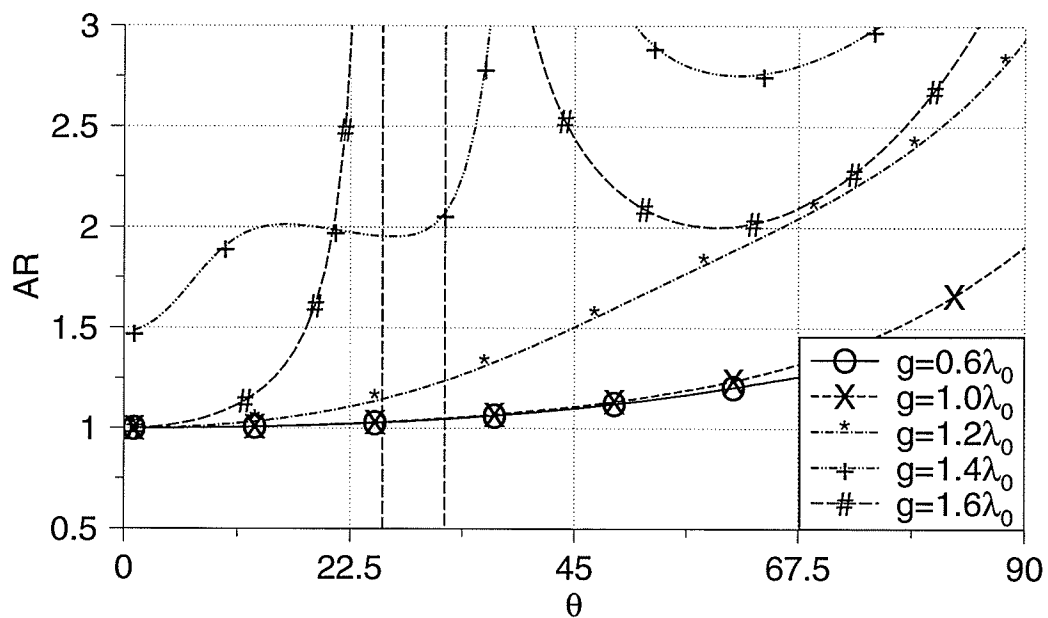


Fig. 3.40. Axial ratio for TM_{41} mode, $\epsilon_r=2.5$

3.6. Summary

In this chapter the effects of the ground plane radius on the gain, radiation pattern and circular polarization of a circular microstrip antenna were studied. Some comparisons between the experiment and simulation, showed good agreements.

It was shown that the gain can be controlled by choosing a proper ground plane radius and it is almost independent of other parameters.

Radiation pattern and polarization can also be controlled by the ground plane radius, but they are also dependent on the substrate permittivity. If circular polarization is desired for a specific range of angle, with choosing the right excited mode and substrate permittivity, it is possible to achieve a reasonable axial ratio. In this case, the ground plane radius can be used as a parameter to maximize the gain.

Radiation angle can be controlled by the ground plane radius, especially for the TM_{21} and higher order modes.

Chapter 4

Effects of the Ground Plane Shape

4.1. Introduction	68
4.2. Cavity Antenna.....	68
4.3. Shaping the Ground Plane	78
4.4. Summary	83

4.1. Introduction

Traditionally the ground plane shape is assumed to be a flat and thin plate. The ground plane shape can be modified in order to change the radiation patterns, beamwidth, as well as the gain and circularity of polarization. For some applications a narrow beamwidth is desired, while for others wide beamwidths may be required. In this chapter the effects of the ground plane shape on the shape of radiation patterns are discussed by means of some designs. The first design provides high gain and narrow beamwidths, while the next one has a flat radiation pattern, very wide beamwidths and good circular polarization. These designs are for the dominant mode and all the antennas have a permittivity of 2.5.

4.2. Cavity Antenna

The geometry of the first design is shown in Fig. 4.1. The ground plane has a rim of height r and width d at its edge, which resembles an open cavity fed by a microstrip antenna.

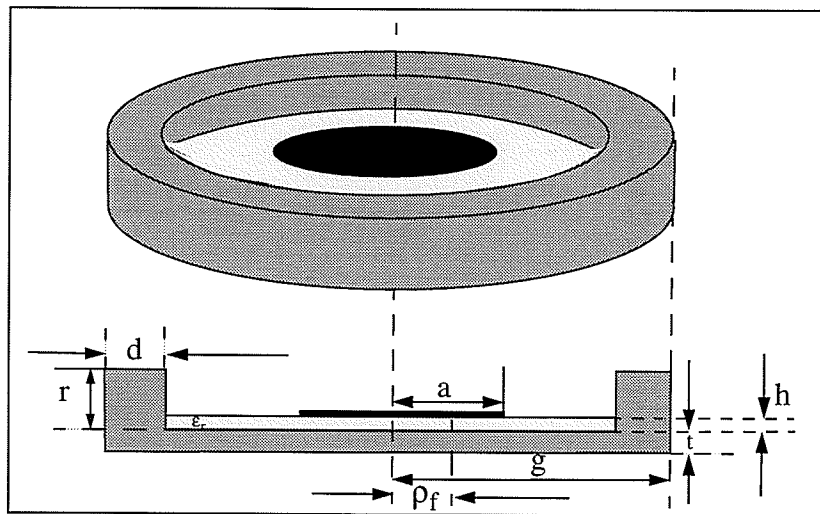


Fig. 4.1. Geometry of microstrip antenna with cavity shape ground plane

The rim, in fact, limits the amount of radiation to the sides and backward directions. This configuration was used for three different ground plane radii ($0.4\lambda_0$, $0.6\lambda_0$ and $0.8\lambda_0$) and the effect of rim height (r) and width (d) were investigated.

Figs. 4.2 and 4.3 compare samples of radiation patterns of antennas with and without a rim. They show that adding a rim will increase the gain and decrease the beamwidth. The pattern symmetry also improves for at least $\theta < 70^\circ$.

Fig. 4.4 shows the gain variations for three different antennas. It also shows the effect of rim width and height. The best improvement in the gain for each antenna is given in Table (4-1).

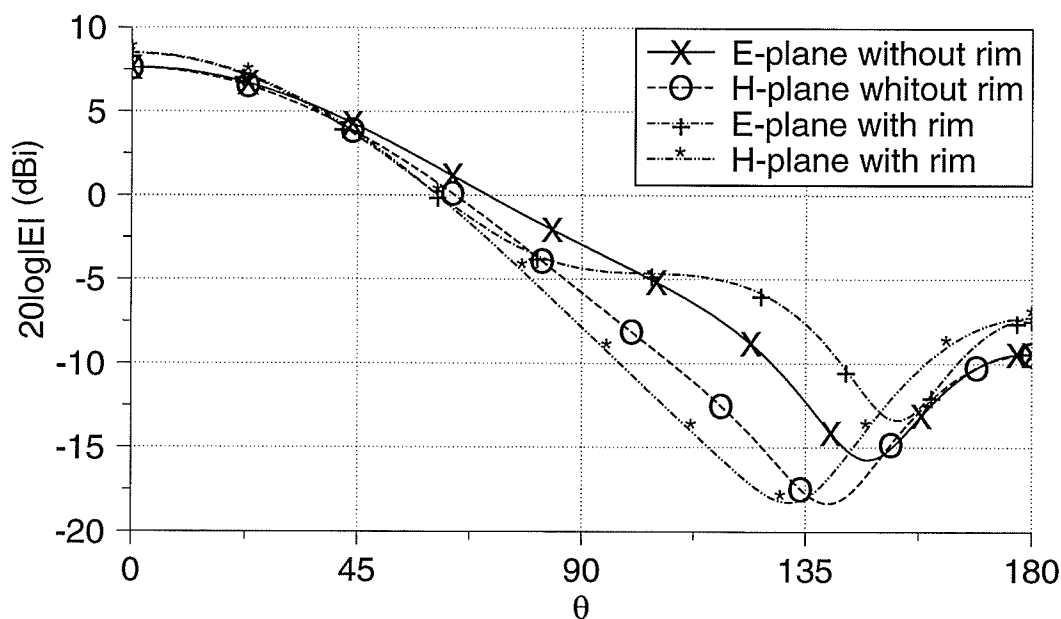


Fig. 4.2. Radiation patterns for antennas with $g=0.4\lambda_0$, rim dimensions are $r=0.4\lambda_0$, $d=0.02\lambda_0$

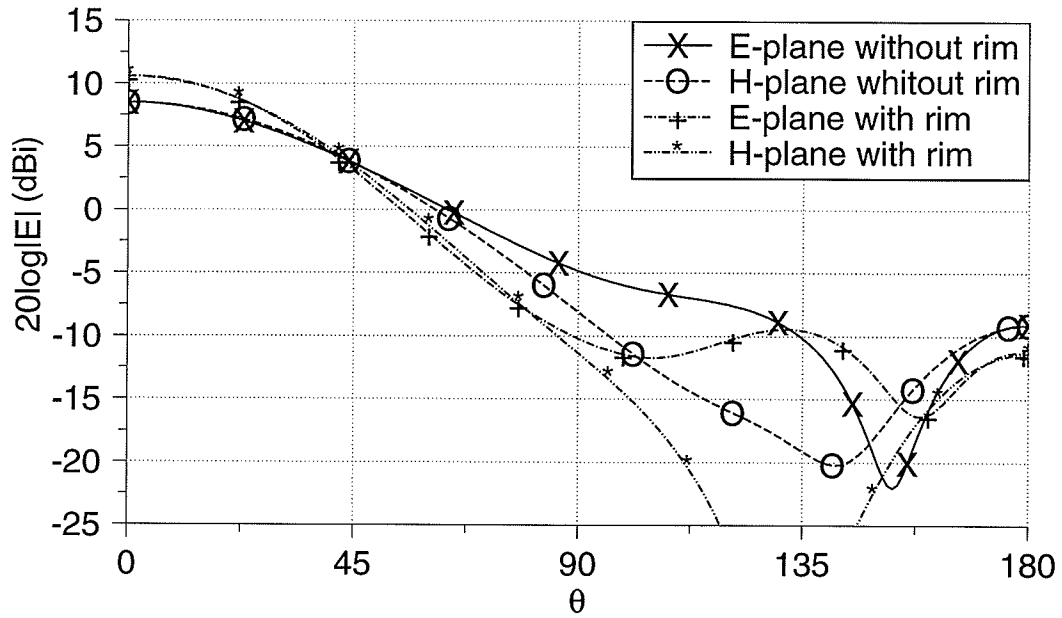


Fig. 4.3. Radiation patterns for antennas with $g=0.6\lambda_0$, rim dimensions are $r=0.4\lambda_0$, $d=0.1\lambda_0$

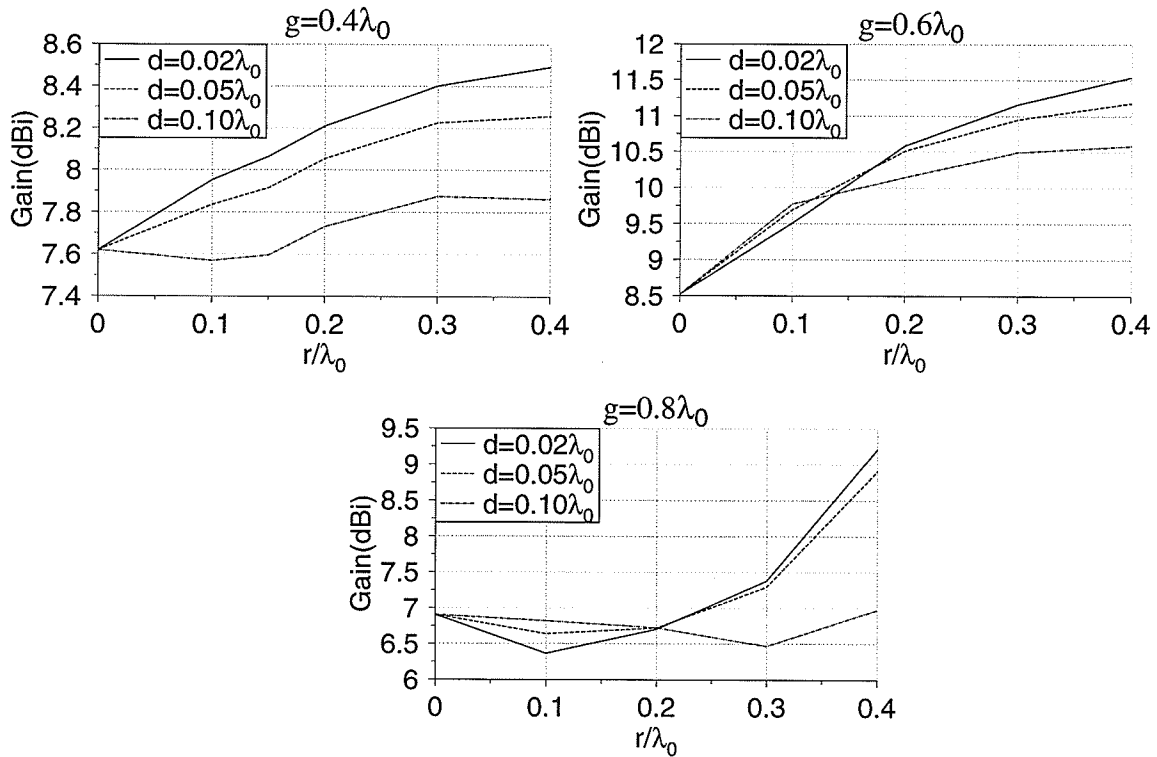


Fig. 4.4. Gain variation for antennas with cavity shape ground plane

Table (4-1) Maximum gain improvement in terms of ground plane radius

g/λ_0	Gain improvement (dBi)
0.4	0.87
0.6	3.02
0.8	2.30

These results show that:

- Gain is maximum for $g=0.6\lambda_0$.
- Gain improvement is dependent not only on the size of the rim but also on the ground plane radius (g), and thus the ratio of the rim height to ground plane radius (r/g) is a determining factor.
- Increasing rim height (r) increases the gain.

It is worth mentioning that increasing the gain does not necessarily mean improvement in the pattern symmetry. In Figs. 4.5 and 4.6 the radiation patterns for two antennas with the same ground plane radius ($g=0.6\lambda_0$), rim height ($r=0.4\lambda_0$) and different rim widths ($d=0.02\lambda_0$, and $d=0.1\lambda_0$) are shown. Although for the antenna with $d=0.1\lambda_0$, the gain improvement is more than that of the antenna with $d=0.02\lambda_0$, the pattern symmetry, axial ratio and backlobe level are much better for the first one.

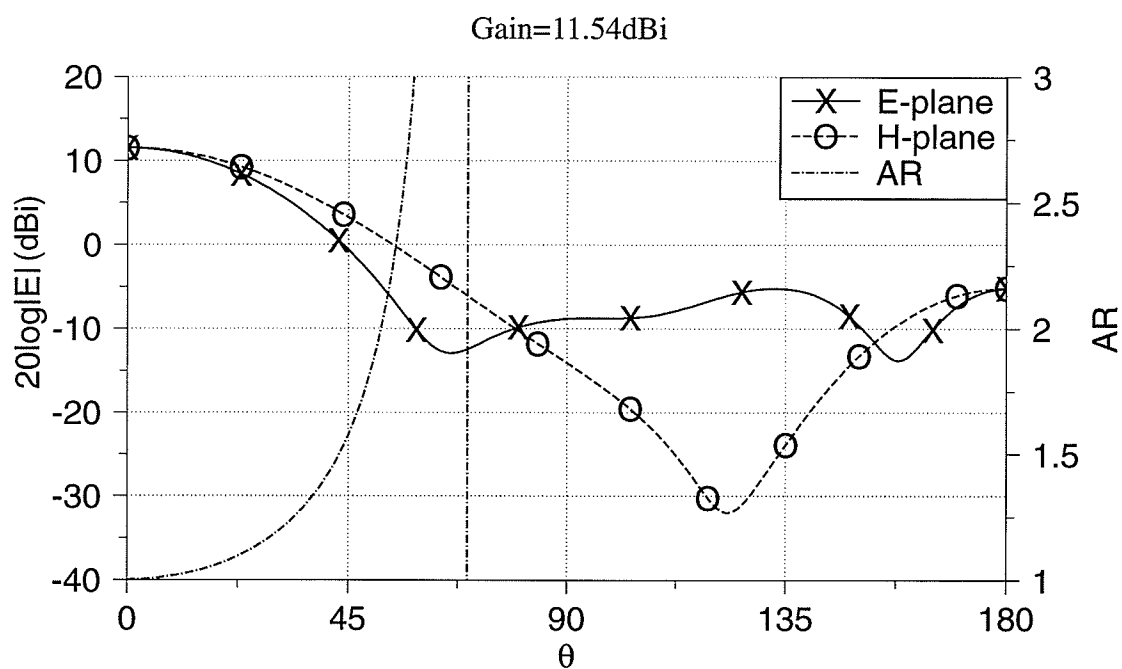


Fig. 4.5. Radiation patterns for antenna with $g=0.6\lambda_0$, $r=0.4\lambda_0$, and $d=0.02\lambda_0$

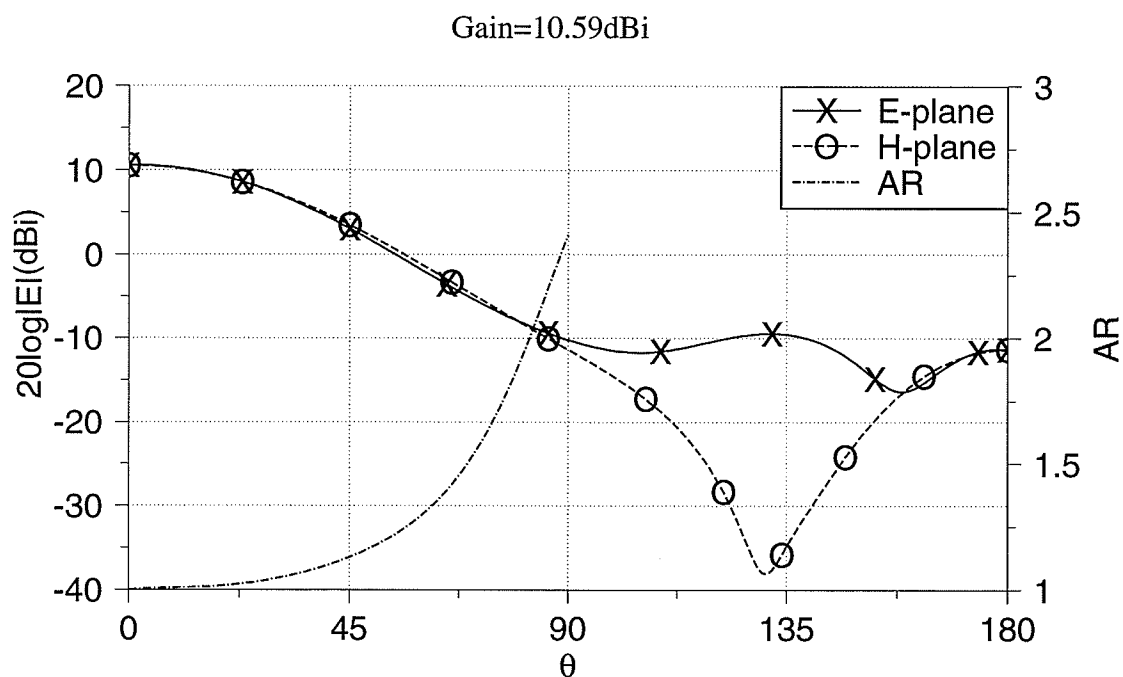


Fig. 4.6. Radiation patterns for antenna with $g=0.6\lambda_0$, $r=0.4\lambda_0$, and $d=0.10\lambda_0$

Adding a chock to the rim wall as shown in Fig. 4.7 provides more gain and lower backlobe level, but it decreases the beamwidth of the E-plane and deteriorates the pattern symmetry. Fig. 4.8 shows the radiation patterns for an antenna with chock. Note that the radiation patterns for the same antenna without chock is shown in Fig. 4.6. The gain for this antenna is 11.94dBi and the backlobe level decreases to -30.55dB (8.65dB less than the same antenna without chock). By changing the wall thickness, the gain improves further, but the backlobe level also increases.

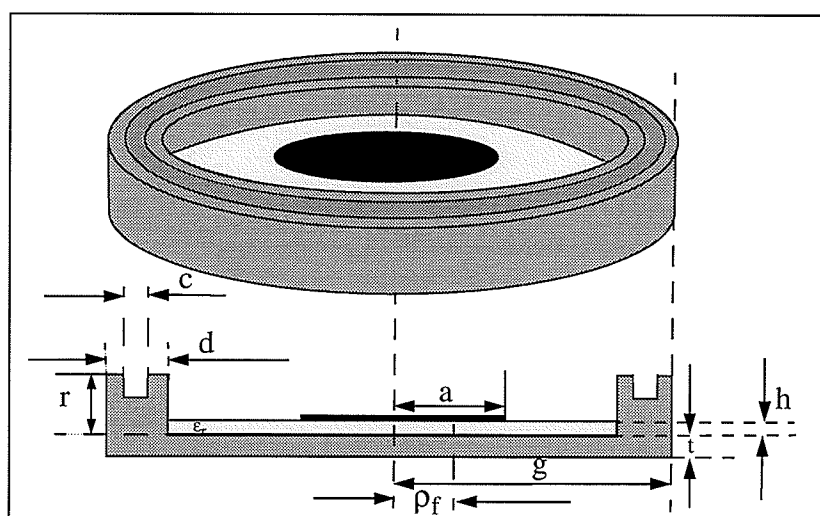


Fig. 4.7. Configuration of antenna with chock

In Figs. 4.9 and 4.10 the HPBW's variations are shown. Changing the rim height (r) does not have an important effect on the radiation patterns of antennas with smaller ground planes, but for $g=0.8\lambda_0$, changes are significant. The backlobe level also shows large variations for larger ground planes (Fig. 4.11). It decreases with r .

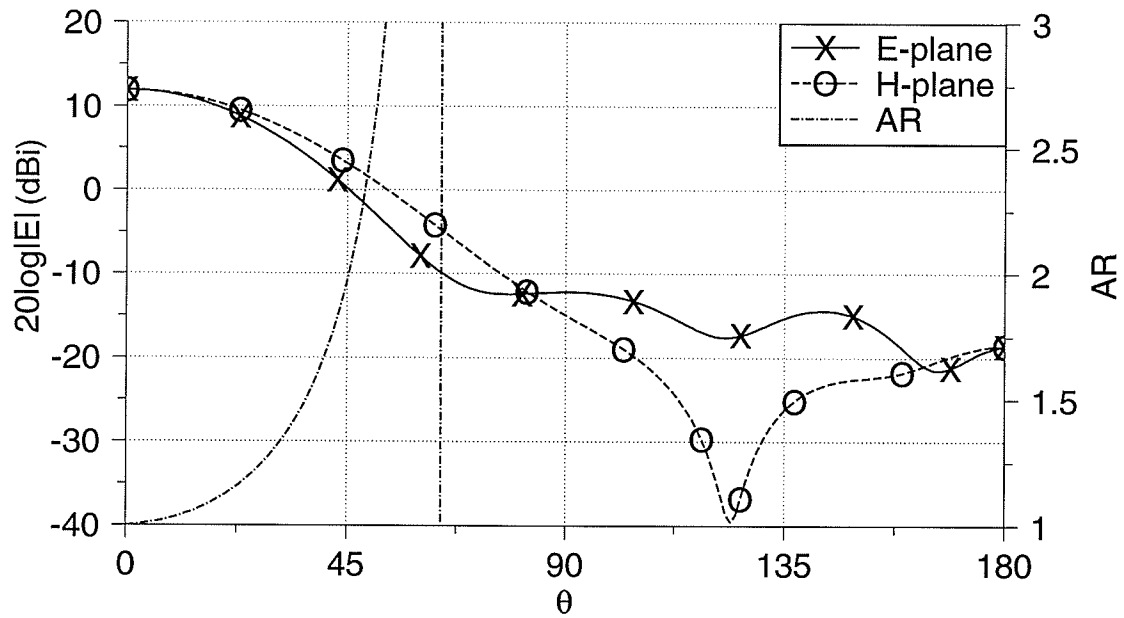


Fig. 4.8. Radiation patterns for antenna with chock, $g=0.6\lambda_0$, $r=0.4\lambda_0$, and $d=0.10\lambda_0$

The axial ratio for $g=0.4\lambda_0$, is weakly dependant on d , and improves by increasing r , for $0 < r < 0.3\lambda_0$. For $r=0.4\lambda_0$, its improvement is for $\theta=75^\circ$. For $g=0.6\lambda_0$, the axial ratio is more dependant on d . For smaller d , it improves by increasing r , but for larger d , it degrades for $r < 0.3\lambda_0$ and then starts to improve. For $g=0.6\lambda_0$, increasing d improves the axial ratio for a constant r , but deteriorates it for $g=0.8\lambda_0$. Increasing r , for $g=0.8\lambda_0$, increases the axial ratio. These results are summarized in Table (4-2). Some sample results are shown in Figs. 4.12 to 4.14.

Table (4-2) Variation of axial ratio with rim dimensions

g/λ_0	$r \nearrow$	$d \nearrow$
0.4	\searrow	no change
0.6	\nearrow small d \nwarrow large d	\searrow
0.8	\nearrow	\nearrow

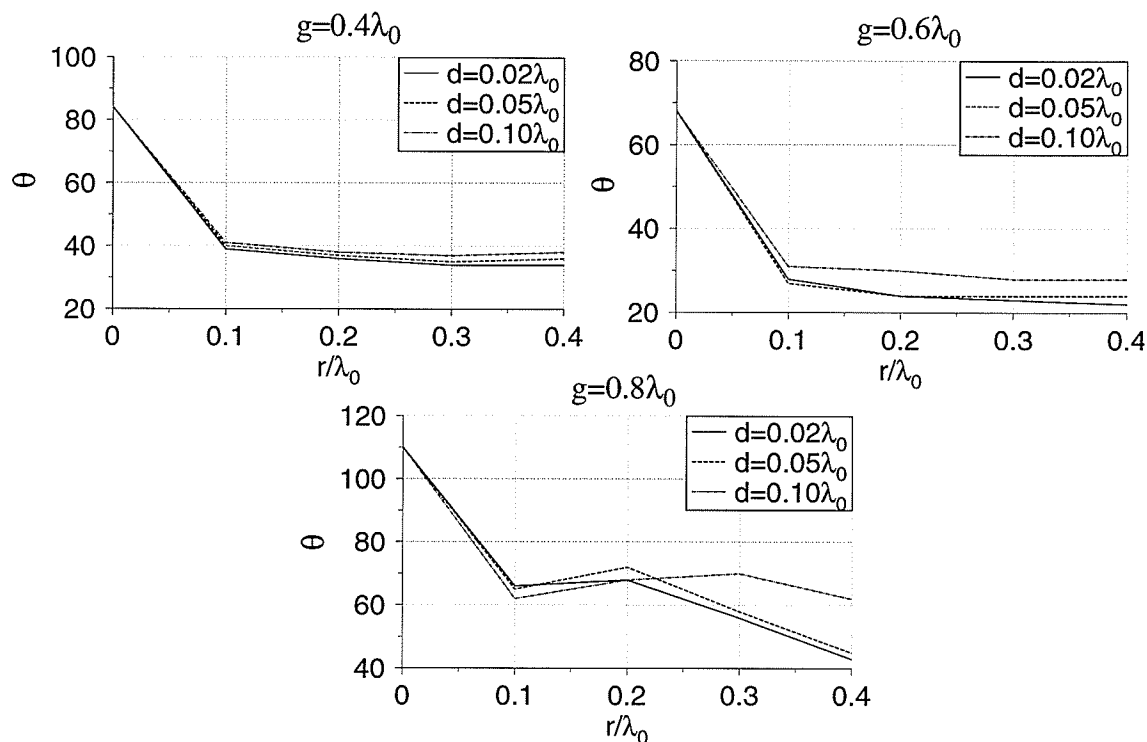


Fig. 4.9. E-plane beamwidth

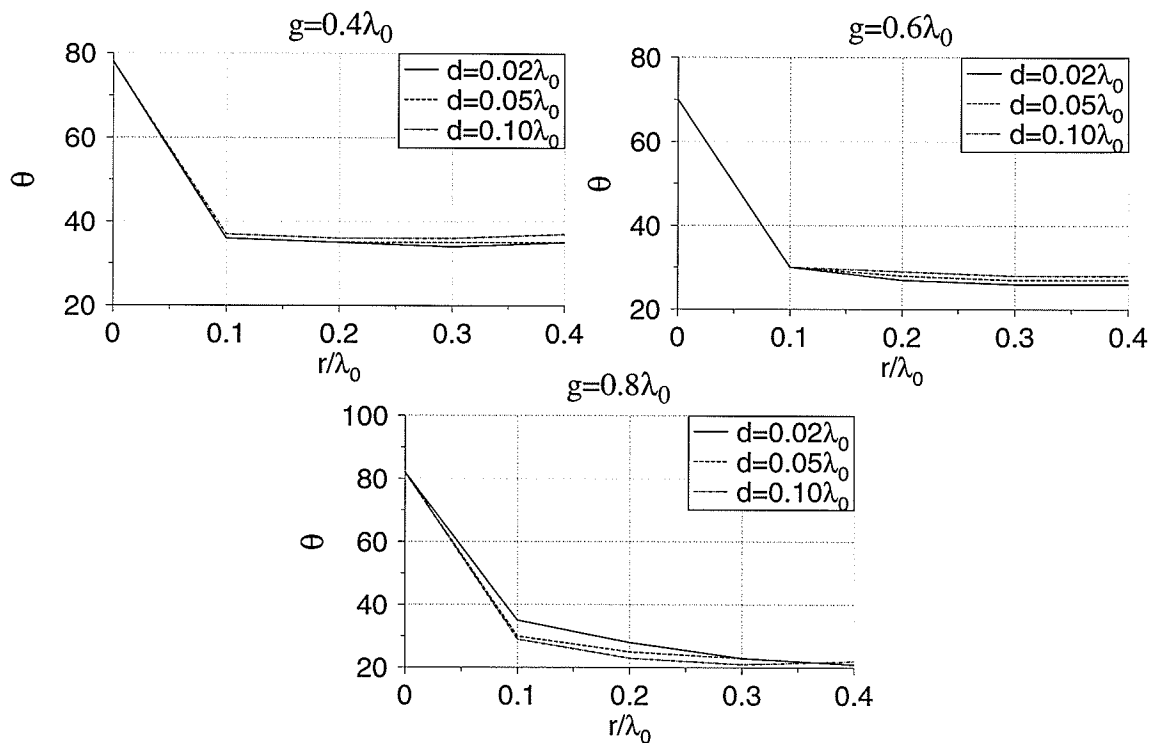


Fig. 4.10. H-plane beamwidth

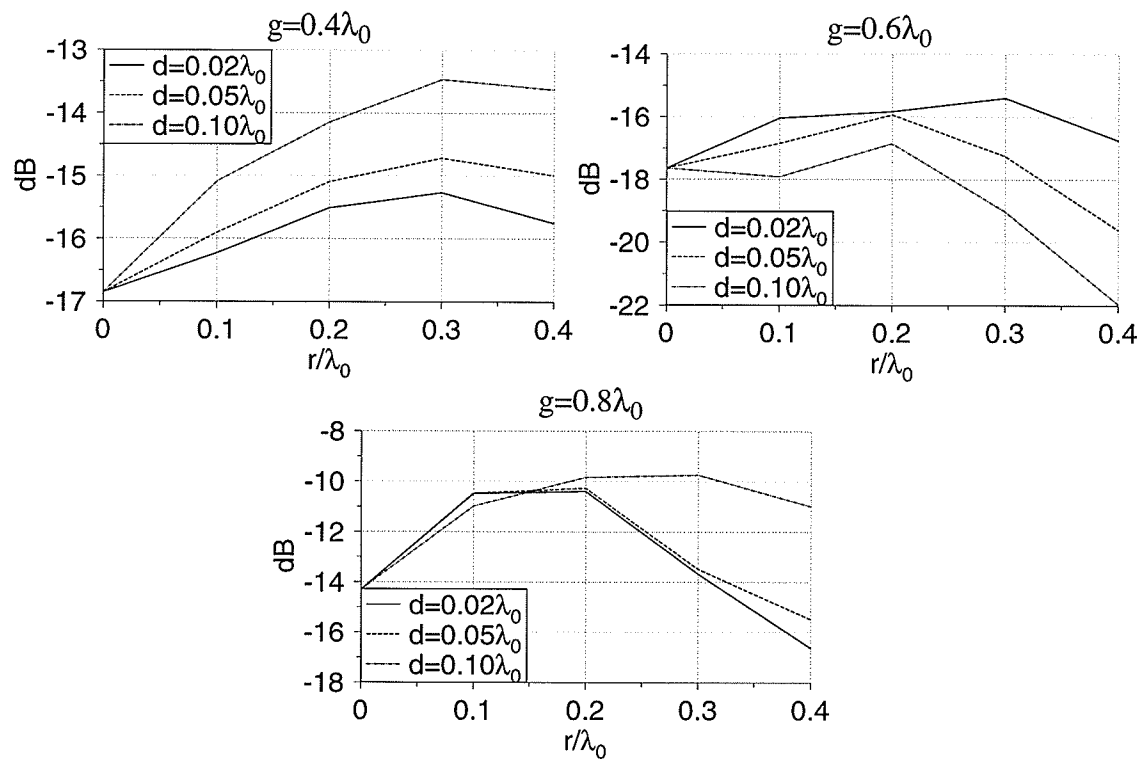


Fig. 4.11. Backlobe level

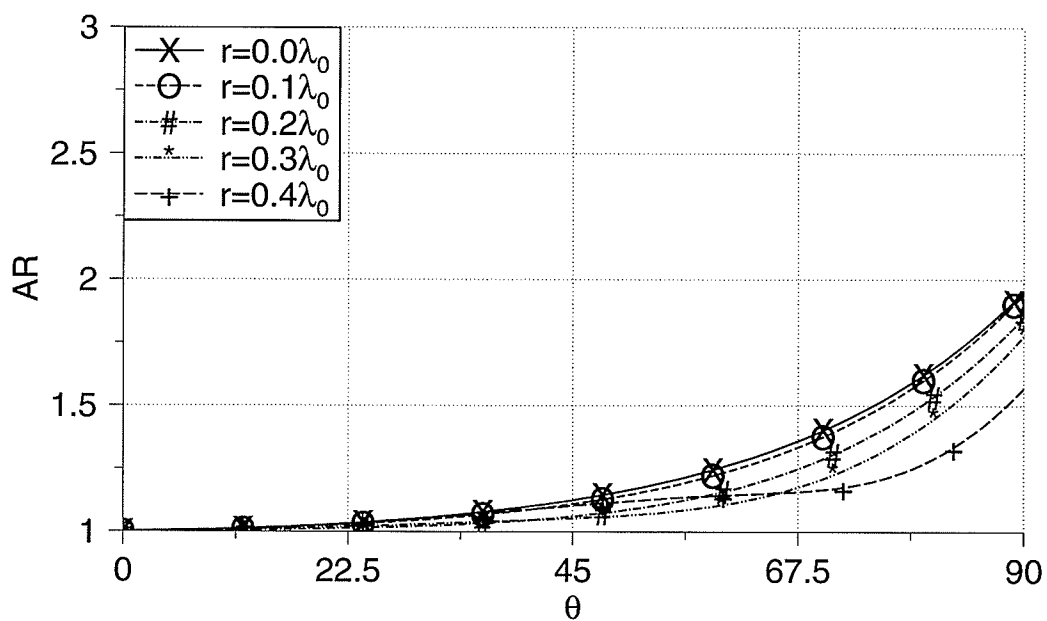


Fig. 4.12. Axial ratio for $g=0.4\lambda_0$, $d=0.05\lambda_0$

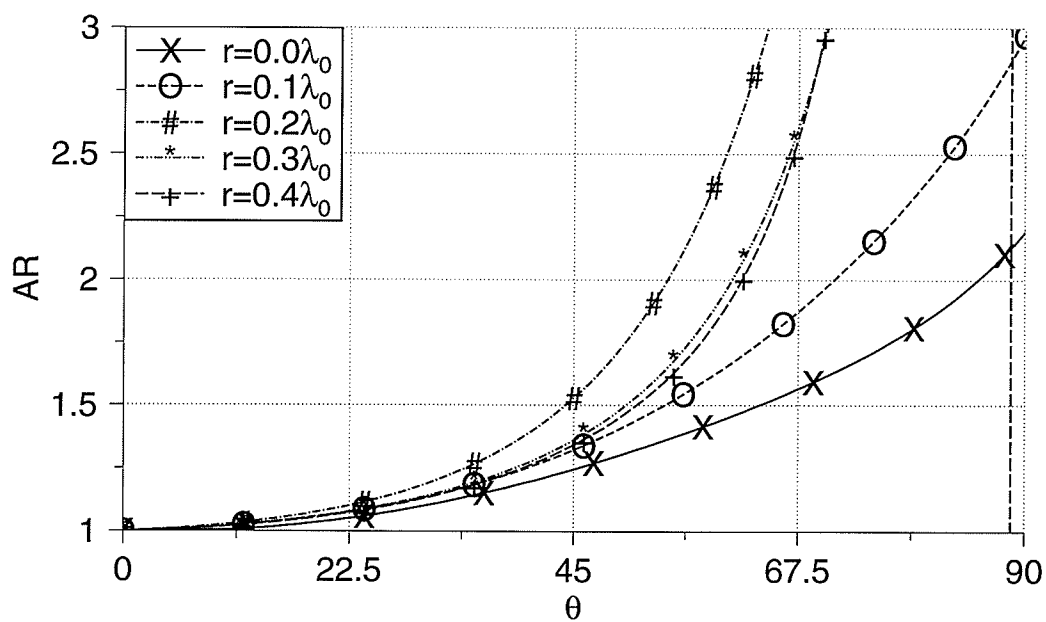


Fig. 4.13. Axial ratio for $g=0.6\lambda_0$, $d=0.05\lambda_0$

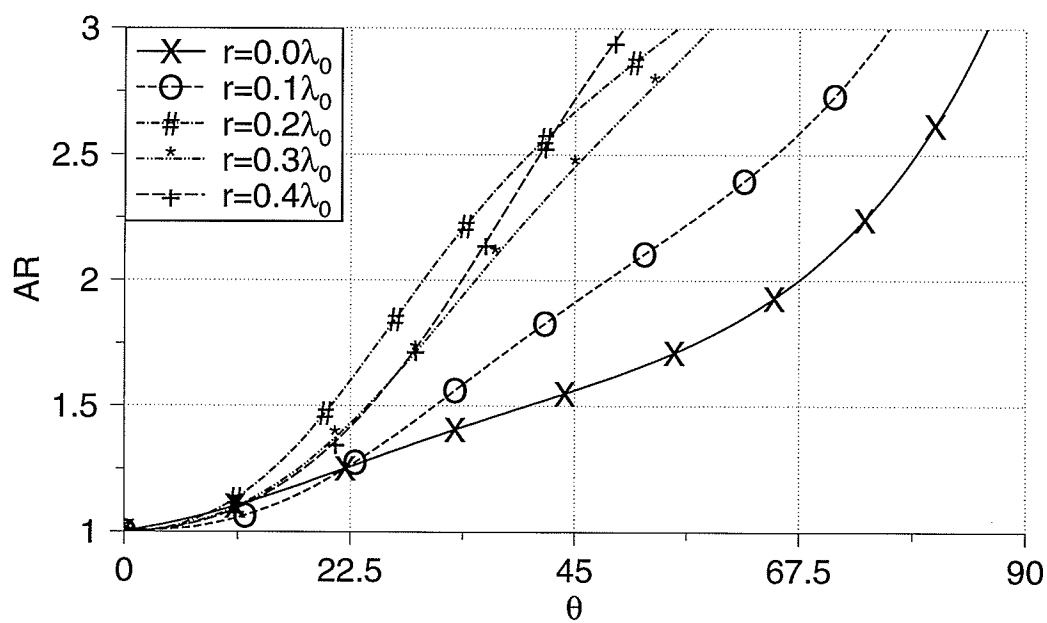


Fig. 4.14. Axial ratio for $g=0.8\lambda_0$, $d=0.05\lambda_0$

4.3. Shaping the Ground Plane

In this section, the effects of changing the ground plane shape on the radiation pattern is discussed. The goal is to find a ground plane shape which provides larger beamwidths and flat radiation patterns. The general shape of the antenna is given in Fig. 4.15. The effects of shaping the ground plane, as shown in Figs. 4-15-b to 4-15-g, can be summarized as:

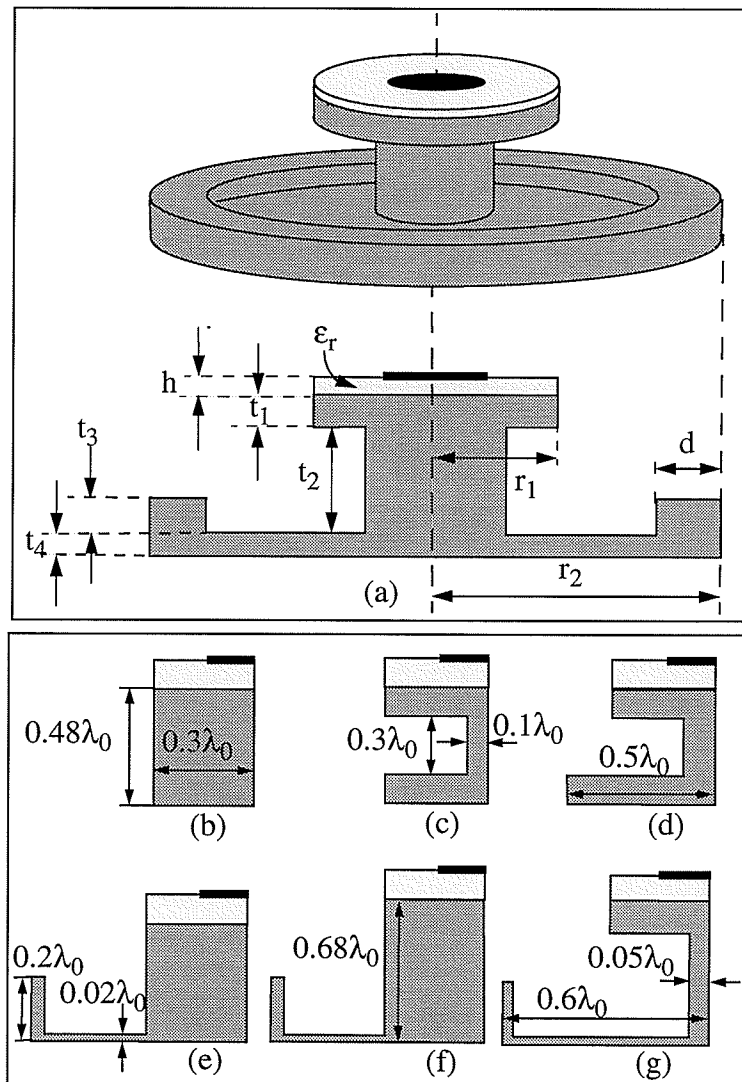


Fig. 4.15. Microstrip antenna with shaped ground plane, ($h=0.04\lambda_0$)

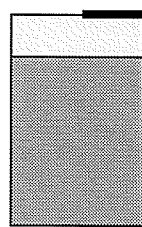
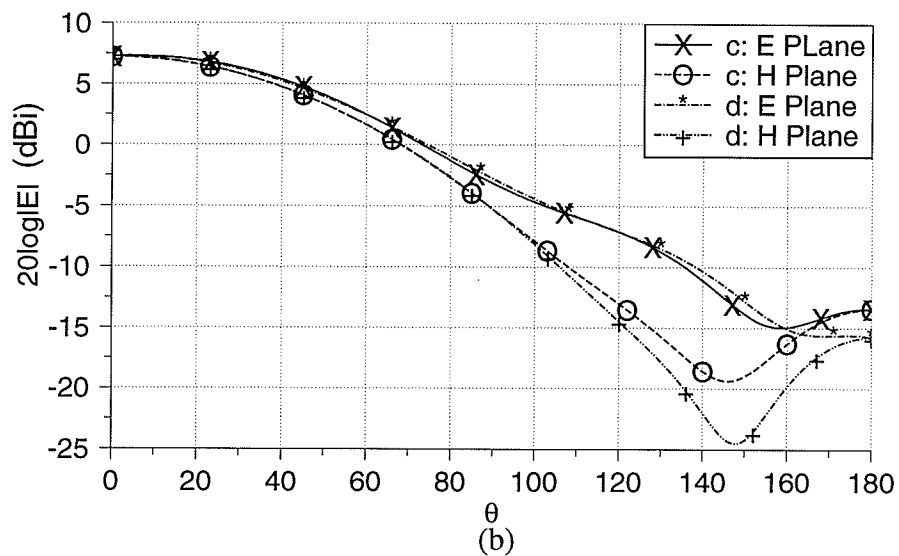
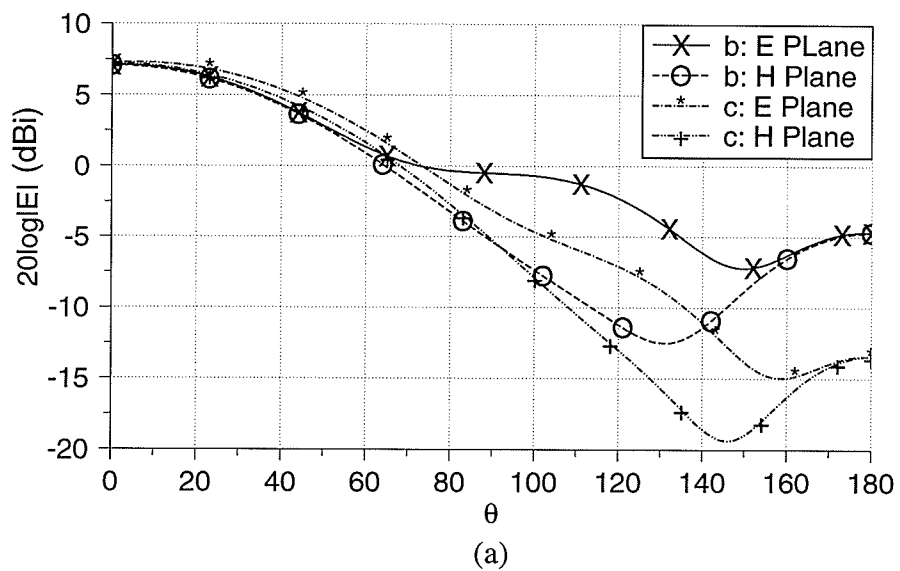
- Changing a regular ground plane as shown in Fig. 4.15-b, to the shape shown in Fig. 4.15-c reduces the backlobe level (Fig. 4.16-a).
- Increasing r_2 further in Fig. 4.15-d, as compared to Fig. 4.15-c, reduces the backlobe level further (Fig. 4.16-b).
- Adding a vertical rim (t_4), as shown in Fig. 4.15-e, increases the gain and improves the pattern equality (Fig. 4.17-a).
- Increasing r_1 , as shown in Fig. 4.15-f, reduces the gain, but increases the backlobe level (Fig. 4.17-b).
- The configuration of Fig. 4.15-g provides lower backlobe level and more flatness in the patterns (Fig. 4.18).

Radiation pattern parameters for these antennas are listed in Table (4-3).

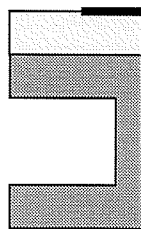
The radiation patterns and axial ratio for the antenna shown in Fig. 4.15-g, are shown in Fig. 4.19. The radiation patterns are flat over a wide range of θ and the axial ratio is less than 1.15 for $\theta < 65^\circ$.

Table (4-3) Radiation pattern parameters for the antennas shown in Fig. 4.15

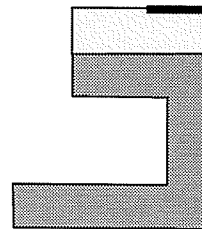
Antenna	Gain (dBi)	E-Plane HPBW (degree)	H-Plane HPBW (degree)	Peak Difference (dB)	Backlobe Level (dB)
b	7.1073	41	41	0.0147	-11.7961
c	7.2976	48	43	0.0517	-20.7260
d	7.3089	47	43	0.0382	-23.0549
e	7.6949	44	43	0.0933	-21.9944
f	5.1689	81	62	1.2626	-14.2329
g	4.6232	73	70	-0.0546	-14.4516



#b



#c



#d

Fig. 4.16. Radiation pattern variations for the antennas shown in Figs. 4.15-b to 4.15-d.

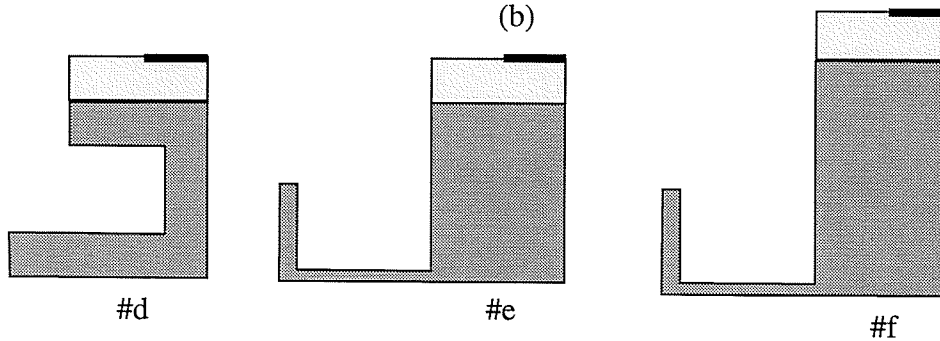
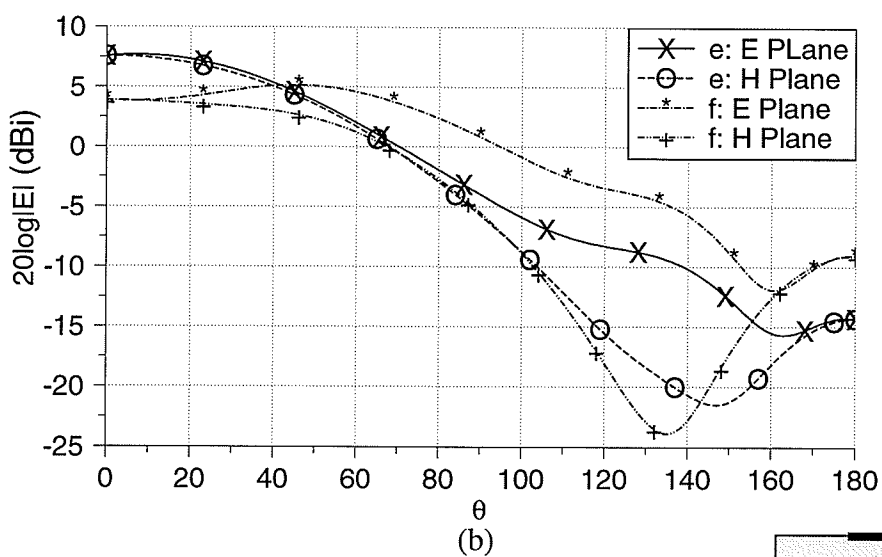
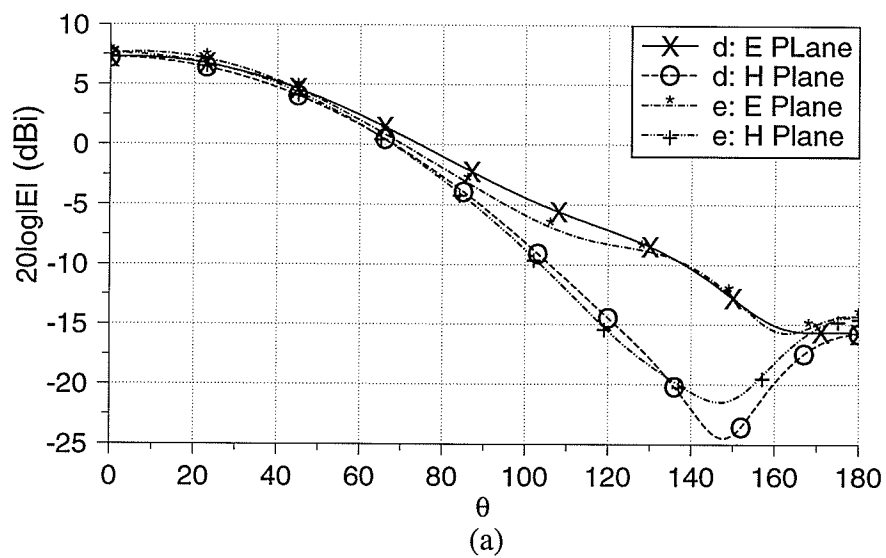


Fig. 4.17. Radiation pattern variations for the antennas shown in Figs.4.15-d to 4.15-f

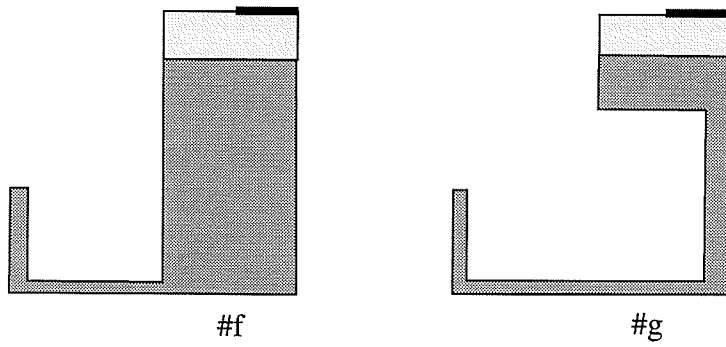
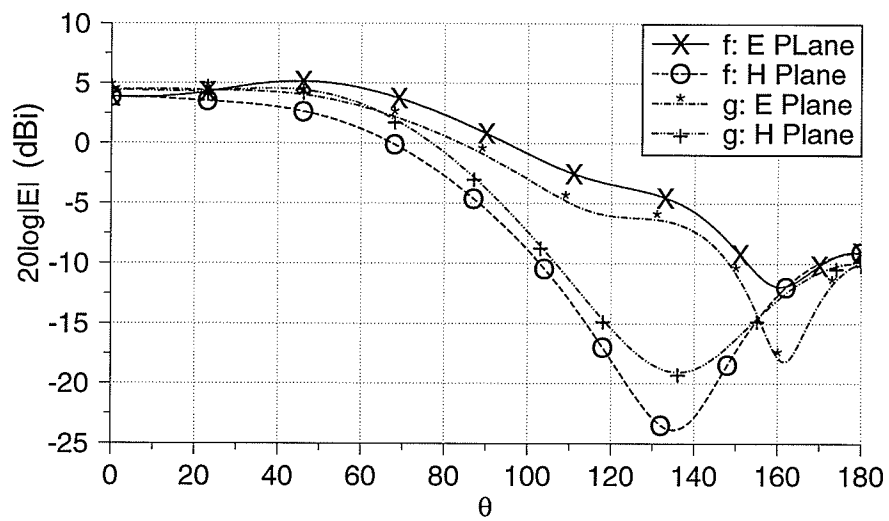


Fig. 4.18. Radiation pattern variations for the antennas shown in Figs.4.15-f and 4.15-g

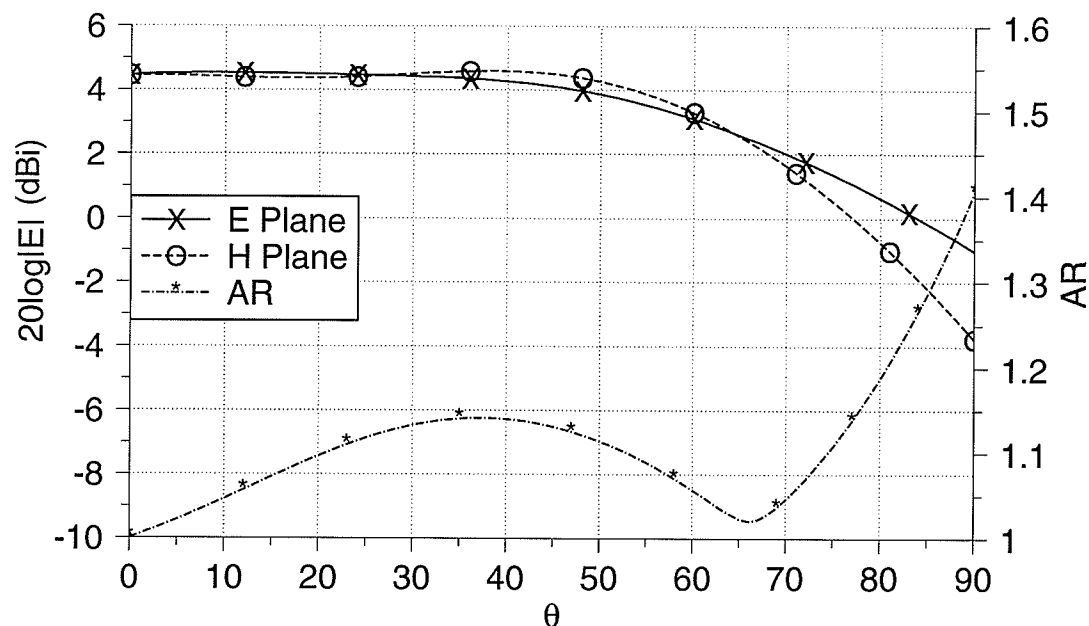


Fig. 4.19. Radiation patterns for the antenna shown in Fig. 4.15-g

4.4. Summary

In this chapter, the method of shaping the radiation patterns by shaping the ground plane was discussed. Two sample designs were studied.

The first design was an open cavity fed by a microstrip antenna. This antenna has a high gain and narrow beamwidth and is useful for the applications which require linear polarization.

The second design provides a flat and wide beamwidth. Its axial ratio is excellent and it can be used as a circularly polarized antenna.

For more designs see [18].

Effects of the Ground Plane and Substrate Thicknesses

5.1. Introduction	85
5.2. Effects on the Gain	85
5.3. Effects on the Radiation Patterns	88
5.4. Effects on Circular Polarization	96
5.5. Summary	100

5.1. Introduction

In general, the radius of ground plane has a strong effect on the performance of antenna. However in applications that limit the ground plane radius, its thickness, as well as the substrate thickness, may be used as controlling parameters.

A study was performed for small sizes of the ground plane of microstrip patch antenna with configuration shown in Fig. 3.3 ($g=0.18\lambda_0, 0.20\lambda_0, 0.25\lambda_0$). The substrate permittivity (ϵ_r) for all antennas was equal to 2.5. The effects of ground plane thickness (t) and substrate thickness (h) on the gain, radiation patterns and circular polarization (for the dominant mode) were investigated.

5.2. Effects on the Gain

For each antenna, three different substrate thicknesses ($h=0.01\lambda_0, 0.03\lambda_0, 0.06\lambda_0$) and five different ground plane thicknesses ($t=0.02\lambda_0, 0.05\lambda_0, 0.10\lambda_0, 0.20\lambda_0, 0.30\lambda_0$) were considered. Patch sizes for these substrate thicknesses are listed in Table (5-1). Table (5-2) shows the gain for these antennas. The gain plots are shown in Fig. 5.1. They show that for small ground planes the substrate thickness (h) does not affect the gain, which maximizes for a specific ground plane thickness (t). This size depends on the ground plane radius (g) and is given in Table (5-3).

Table (5-1) Patch sizes for TM_{11} mode and $\epsilon_r=2.5$

h	a/λ
0.01λ	0.1789
0.03λ	0.1708
0.06λ	0.1623

Table (5-2) Gain variation with ground plane and substrate thicknesses(dBi)

g/λ_0	t/λ_0	$h=0.01\lambda_0$	$h=0.03\lambda_0$	$h=0.06\lambda_0$
0.18	0.02	5.4094	5.6422	5.4391
	0.05	6.0453	6.1637	6.0797
	0.10	6.4807	6.4686	6.4884
	0.20	6.4525	6.3620	6.3833
	0.30	5.8768	5.7314	5.6995
0.20	0.02	6.4309	6.5223	6.4057
	0.05	6.6233	6.6889	6.5946
	0.10	6.6687	6.7152	6.6620
	0.20	6.3362	6.3767	6.3453
	0.30	5.5865	5.6159	5.5857
0.25	0.02	6.9716	6.9558	6.7044
	0.05	6.9857	6.9450	6.6821
	0.10	6.8253	6.7969	6.5570
	0.20	6.2627	6.2193	6.0369
	0.30	5.6437	5.6126	5.4432

Table (5-3) Ground plane thicknesses which maximize the gain

g/λ_0	t/λ_0
0.18	0.1-0.2
0.20	0.1
0.25	0.02-0.05

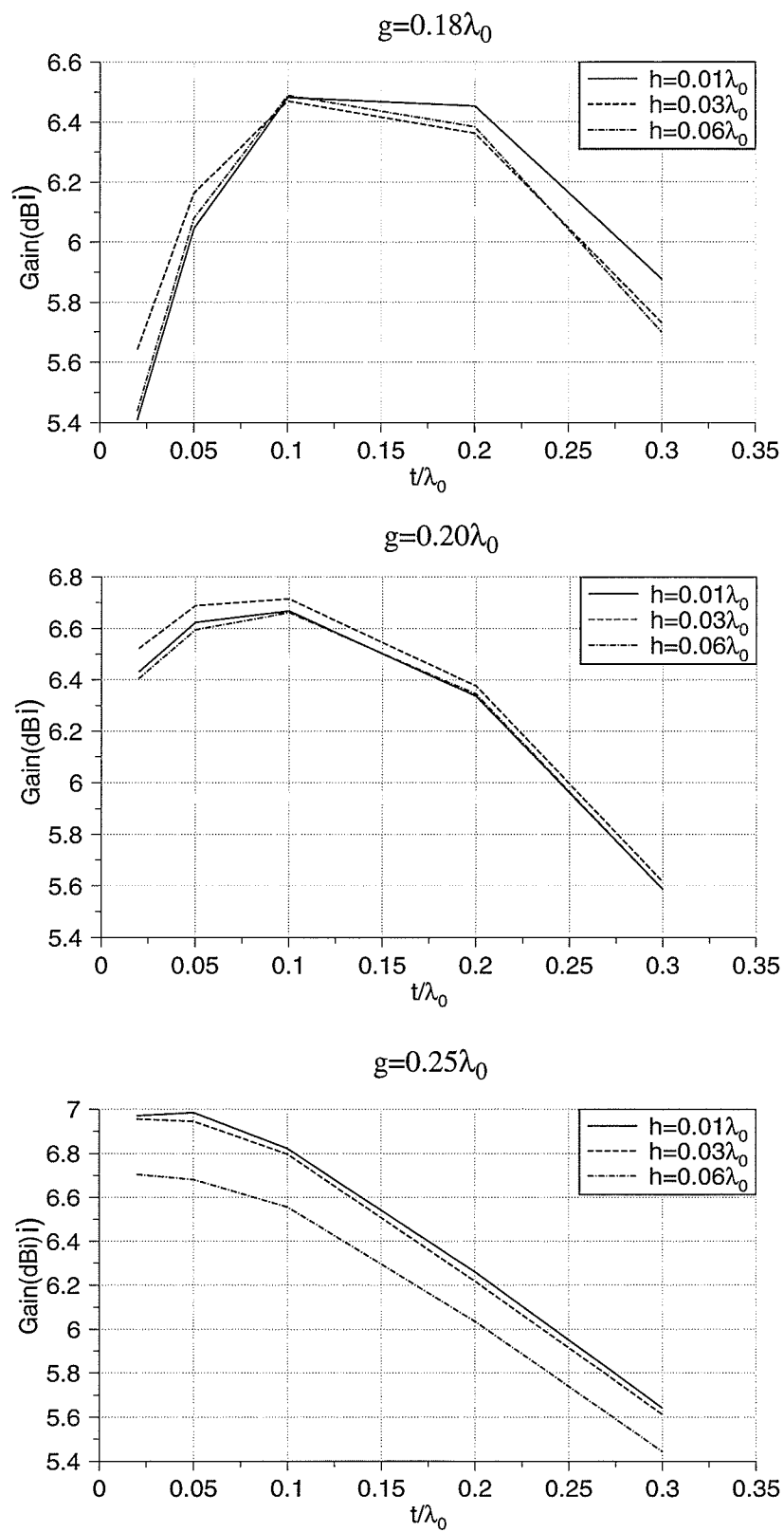


Fig. 5.1. Antennas gain

5.3. Effects on the Radiation Patterns

For all antennas E and H-plane half power beamwidth (E- and H-BW, in degree), peak difference and backlobe level (BLL) were calculated. Table (5-4) and Figs. 5.2 to 5.5 show the results.

Table (5-4) Radiation pattern parameters

g/λ_0	h/λ_0	t/λ_0	E-BW	H-BW	Peak Difference(dB)	BLL(dB)
0.18	0.01	0.02	46	42	0.0000	-2.7494
		0.05	45	43	0.0002	-4.6547
		0.10	43	44	0.0004	-6.3596
		0.20	43	46	0.0000	-7.0360
		0.30	47	49	0.0002	-6.0415
	0.03	0.02	47	43	0.0020	-3.3100
		0.05	45	43	0.0028	-4.7702
		0.10	44	44	0.0027	-6.2501
		0.20	44	46	0.0000	-6.7775
		0.30	49	50	0.0000	-5.6730
	0.06	0.02	49	42	0.0300	-1.9119
		0.05	48	43	0.0361	-3.4256
		0.10	47	44	0.0432	-4.8786
		0.20	48	46	0.0308	-5.5167
		0.30	51	50	0.0121	-4.5355
0.20	0.01	0.02	45	45	0.0000	-7.6069
		0.05	44	45	0.0002	-8.7092
		0.10	45	46	0.0004	-9.4134
		0.20	48	48	0.0000	-8.8687
		0.30	57	50	0.0002	-7.1029

Table (5-4) Radiation pattern parameters

g/λ_0	h/λ_0	t/λ_0	E-BW	H-BW	Peak Difference(dB)	BLL(dB)
0.20	0.03	0.02	46	45	0.0063	-7.7128
		0.05	46	45	0.0093	-8.6405
		0.10	47	46	0.0102	-9.2551
		0.20	50	48	0.0064	-8.6796
		0.30	58	50	0.0046	-6.9040
	0.06	0.02	49	44	0.0426	-6.0750
		0.05	49	45	0.0538	-7.0985
		0.10	50	45	0.0670	-7.8870
		0.20	53	47	0.0581	-7.5942
		0.30	60	51	0.0219	-6.0023
0.25	0.01	0.02	43	45	0.0012	-12.5066
		0.05	44	44	0.0018	-13.0501
		0.10	46	45	0.0023	-12.6930
		0.20	52	47	0.0019	-10.7301
		0.30	61	47	0.0020	-8.6759
	0.03	0.02	45	45	0.0081	-13.2458
		0.05	46	45	0.0131	-13.3802
		0.10	48	45	0.0135	-12.7567
		0.20	55	47	0.0119	-10.7199
		0.30	65	46	0.0088	-8.6785
	0.06	0.02	49	45	0.0270	-12.6602
		0.05	50	45	0.0338	-12.7829
		0.10	52	46	0.0427	-12.4209
		0.20	60	47	0.0381	-10.7278
		0.30	71	48	0.0090	-8.8705

From these results the following facts can be concluded:

- While increasing h does not have a serious effect on the H-plane HPBW, it increases the E-plane HPBW.
- h has a strong effect on the E and H-plane peak difference. Increasing h increases it. This shows that for larger h , the symmetry degrades.
- The backlobe level also increases by increasing h .
- Variation of the E-plane HPBW with t depends on the ground plane radius (g). the H-plane HPBW increases by increasing t .

The variation of radiation pattern parameters with t and h are summarized in Table (5-5).

Table (5-5) Variation of radiation pattern parameters with ground plane and substrate thicknesses

	E-Plane HPBW	H-Plane HPBW	Peak Difference	Backlobe Level
h ↗	↗	—	↗↗	↗
t ↗	↻	↗	↻	↻

Samples of the radiation patterns are shown in Fig. 5.6. For larger g , only the E-plane radiation pattern depends on the ground plane thickness. This parameter can be used to improve the pattern symmetry.

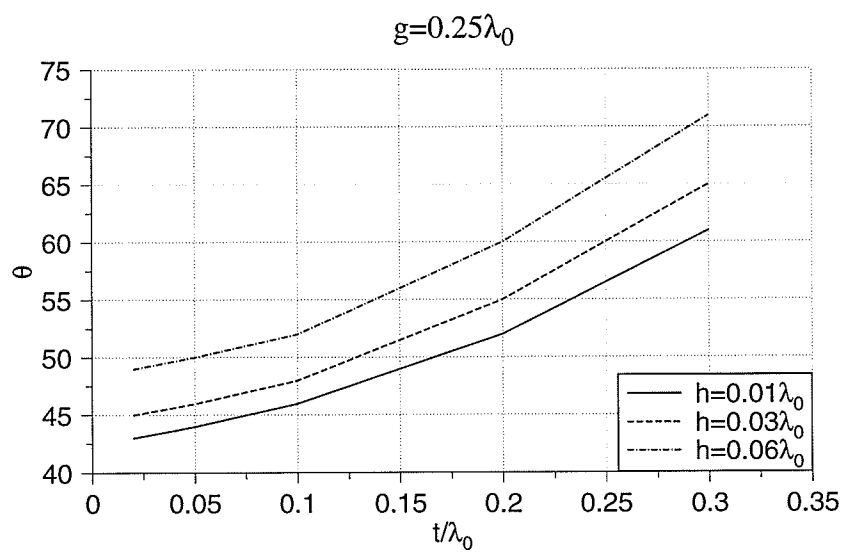
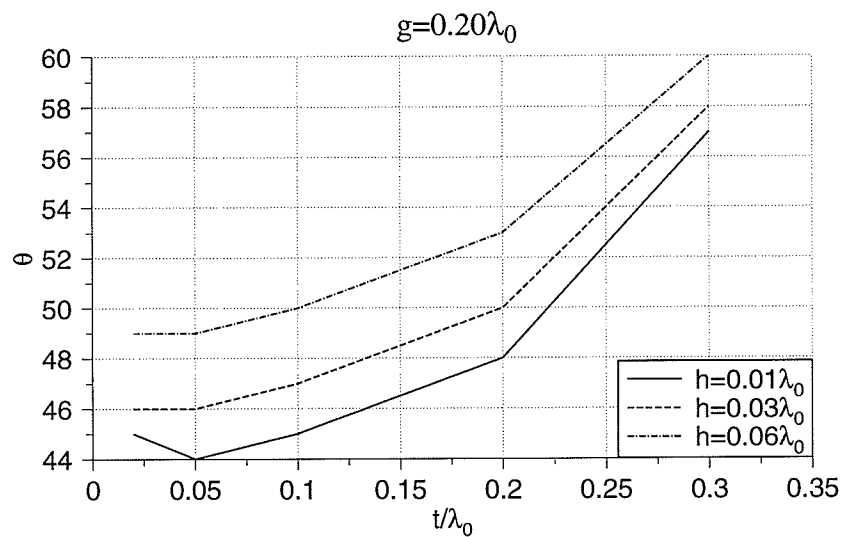
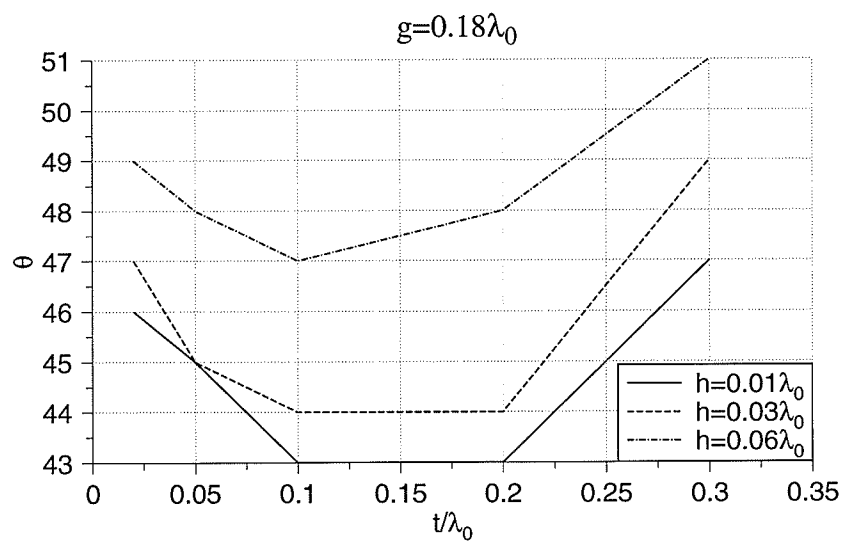


Fig. 5.2. E-plane half power beamwidth

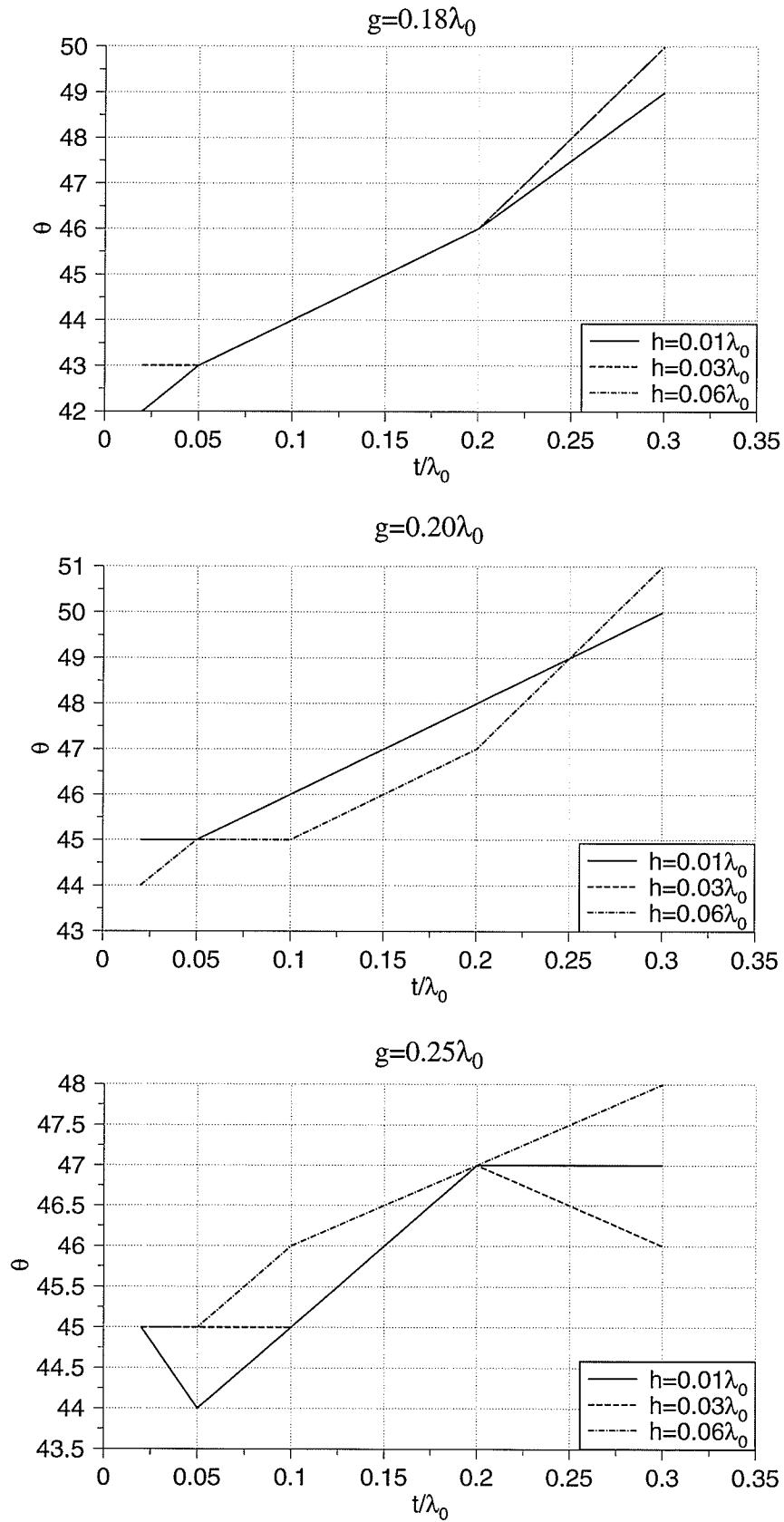


Fig. 5.3. H-plane half power beamwidth

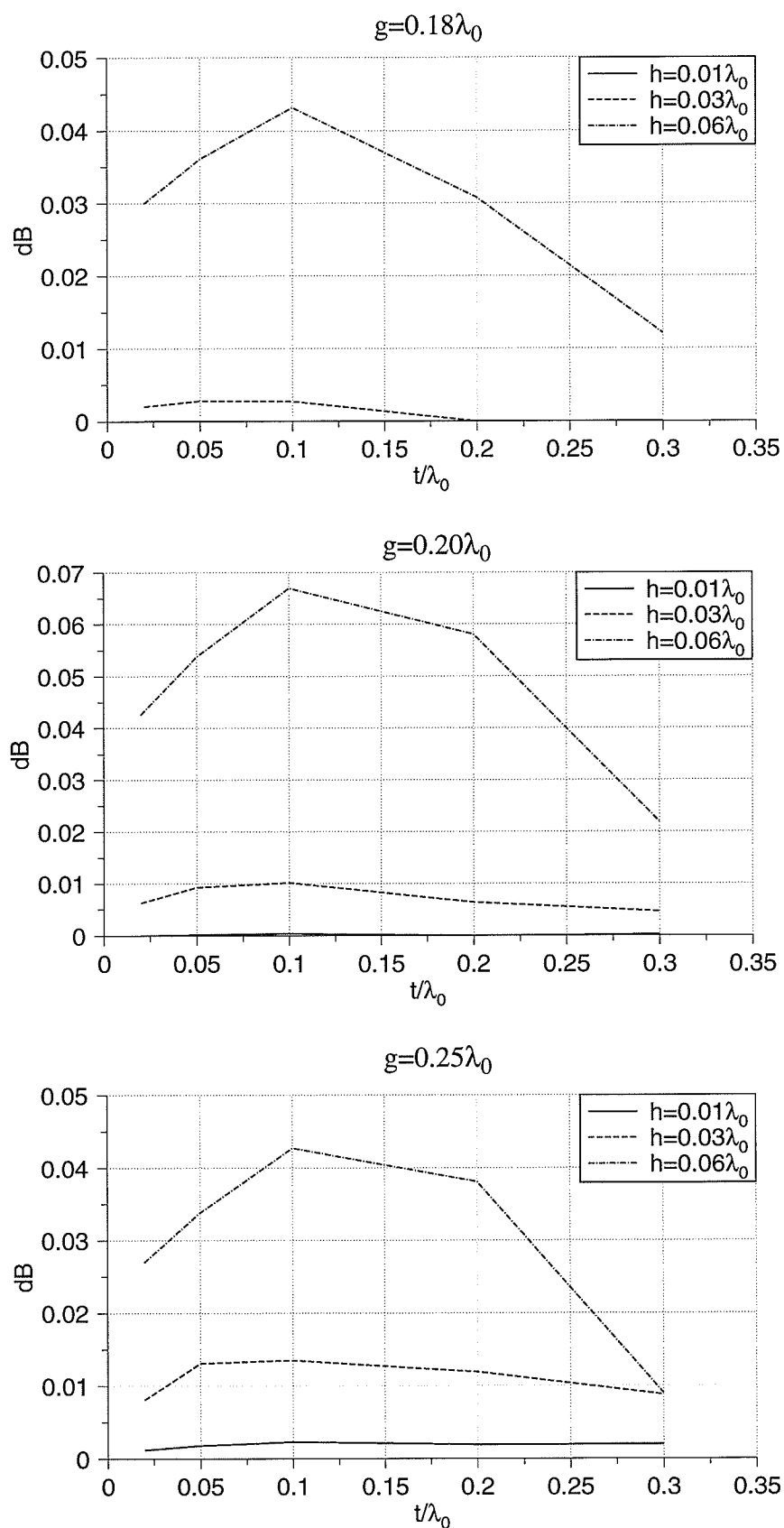


Fig. 5.4. E and H-plane peak difference

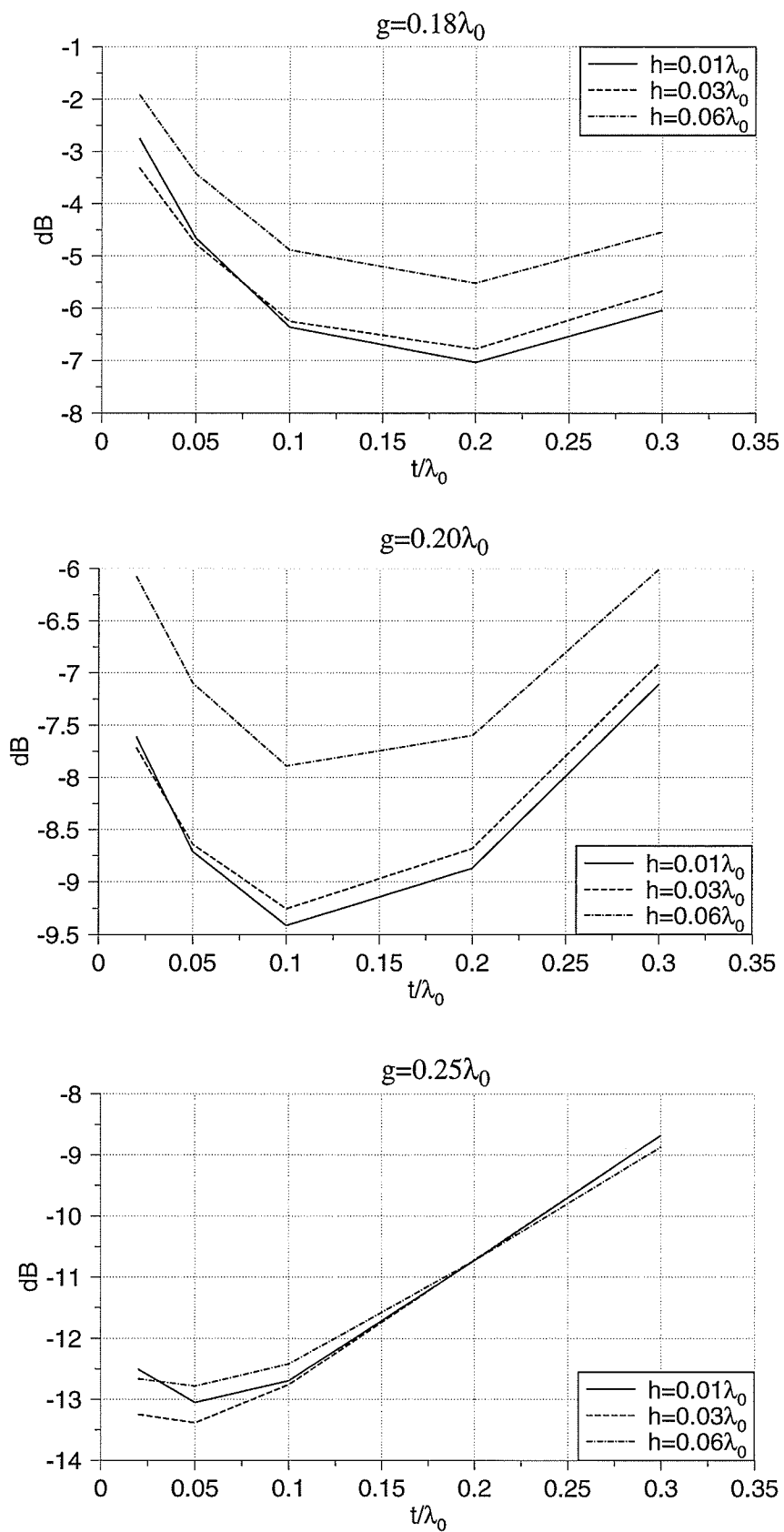


Fig. 5.5. Backlobe level

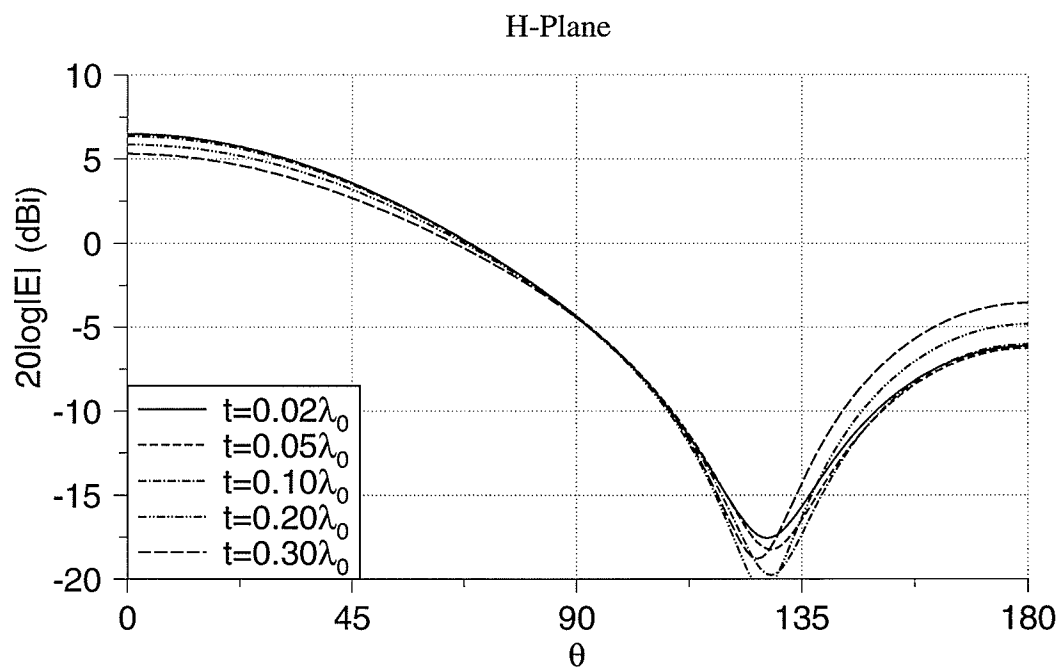
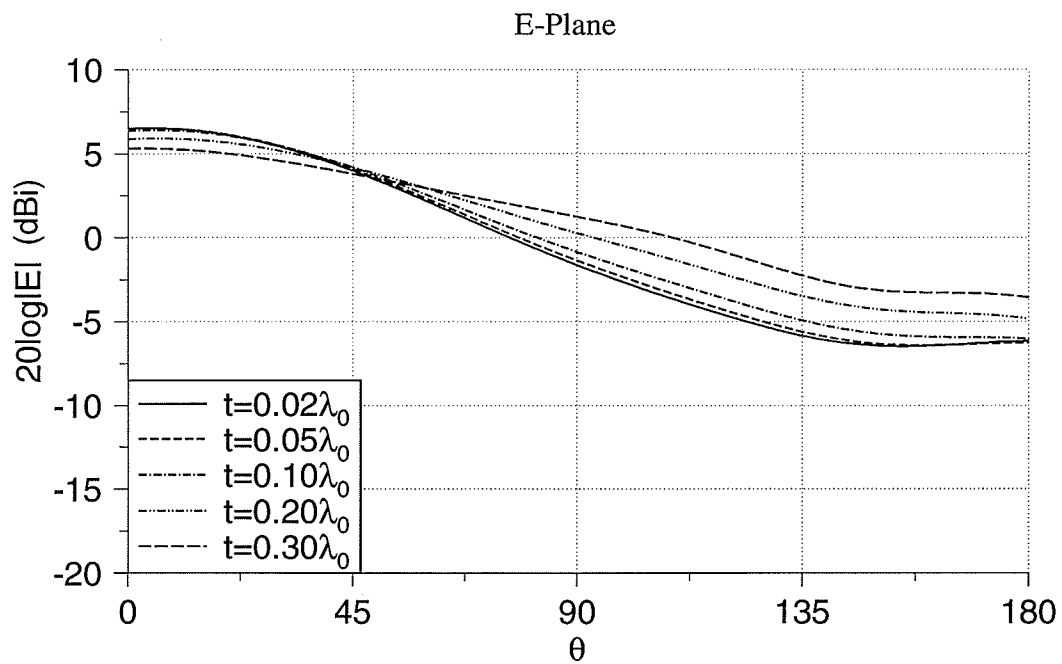


Fig. 5.6. Radiation patterns for an antenna with $g=0.25\lambda_0$ and $h=0.06\lambda_0$.

5.4. Effects on Circular Polarization

The axial ratio for each antenna was calculated. Some sample results are shown in Figs. 5-7 to 5-9. They show that:

- For all antennas, the axial ratio is less than 1.4 for $\theta < 50^\circ$.
- A smaller substrate thickness gives a better axial ratio.
- The best combination of g and t , for each case is:

$$g=0.18\lambda_0, t=0.2\lambda_0$$

$$g=0.20\lambda_0, t=0.1\lambda_0$$

$$g=0.25\lambda_0, t=0.02\lambda_0$$

Therefore, as the ground plane radius increases, its thickness should be decreased. The gain also maximizes for the dimensions mentioned above.

From these results, one can conclude that initially the ground plane radius can be chosen to maximize the gain, then its thickness can be modified to optimize the pattern symmetry and its axial ratio.

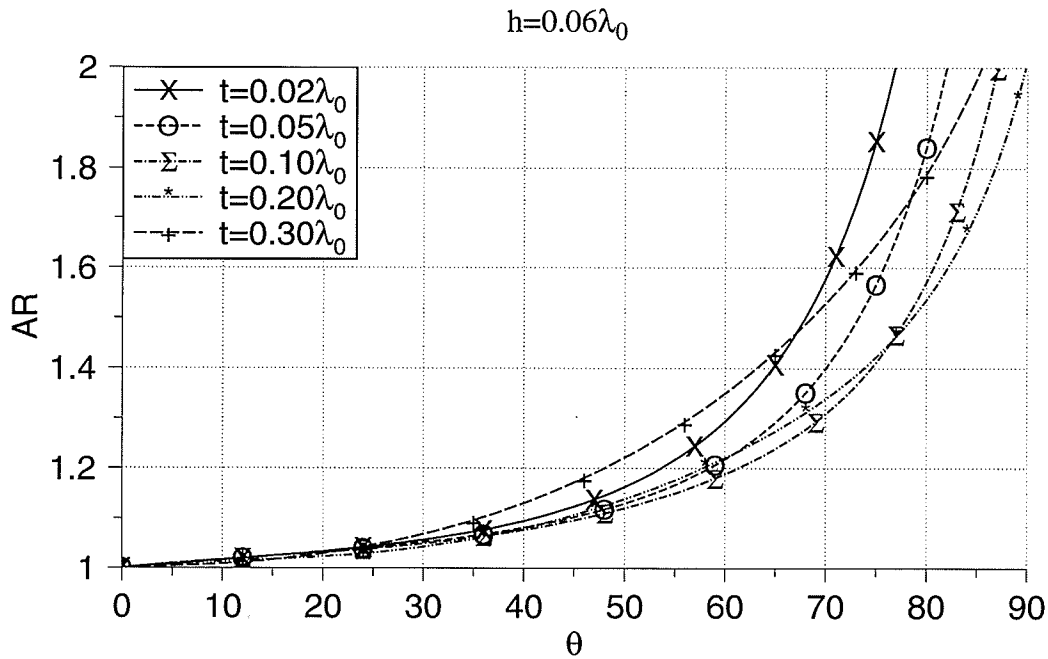
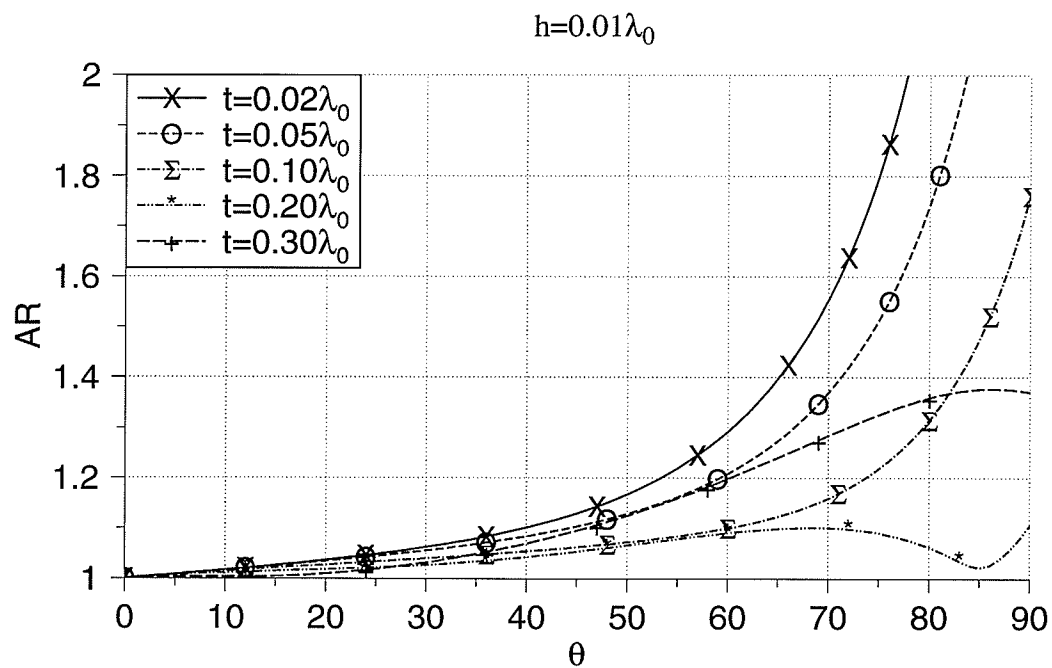


Fig. 5.7. Axial ratio for $g=0.18\lambda_0$

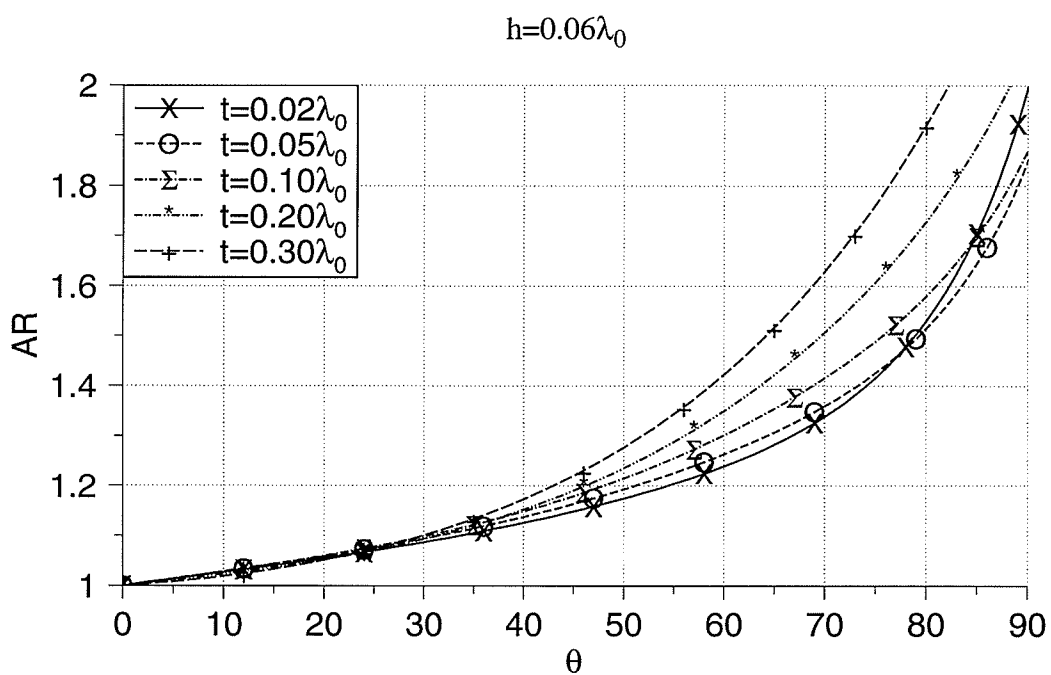
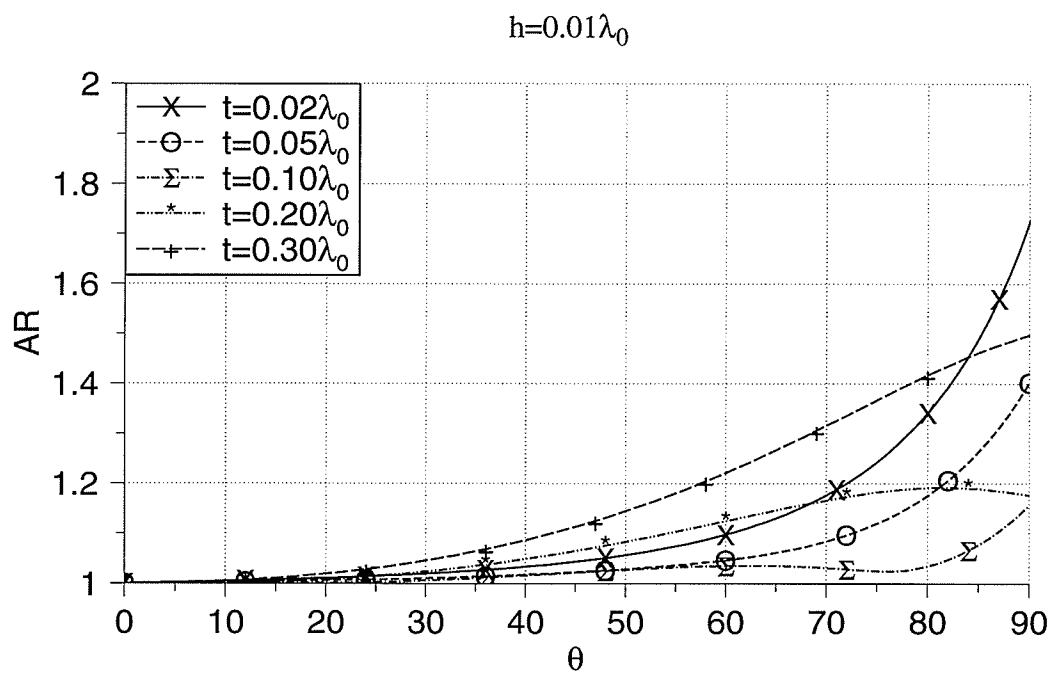


Fig. 5.8. Axial ratio for $g=0.20\lambda_0$

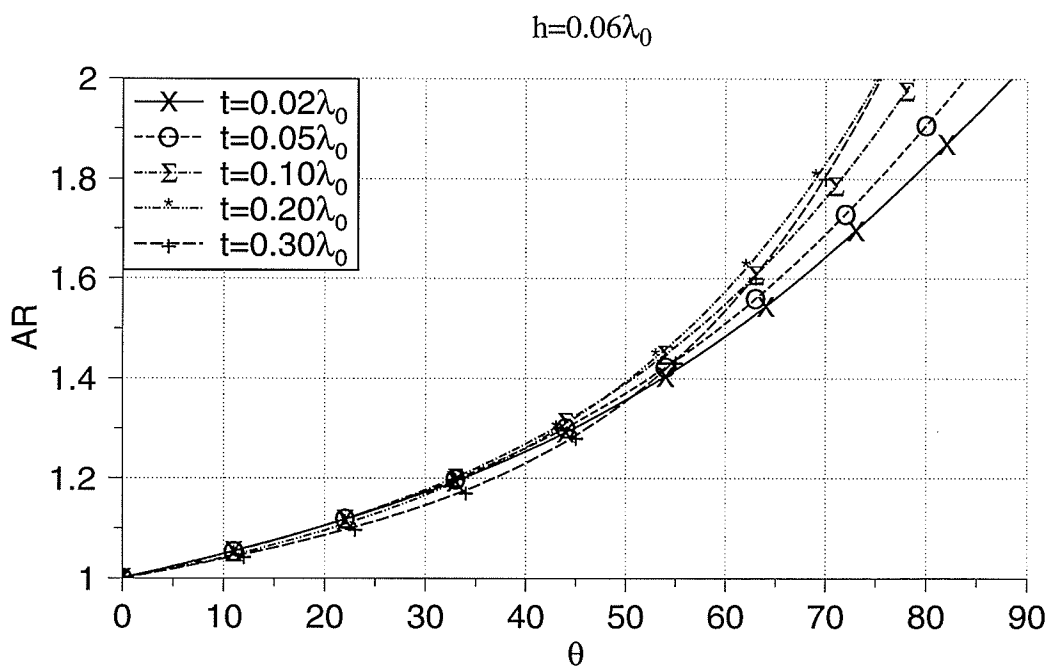
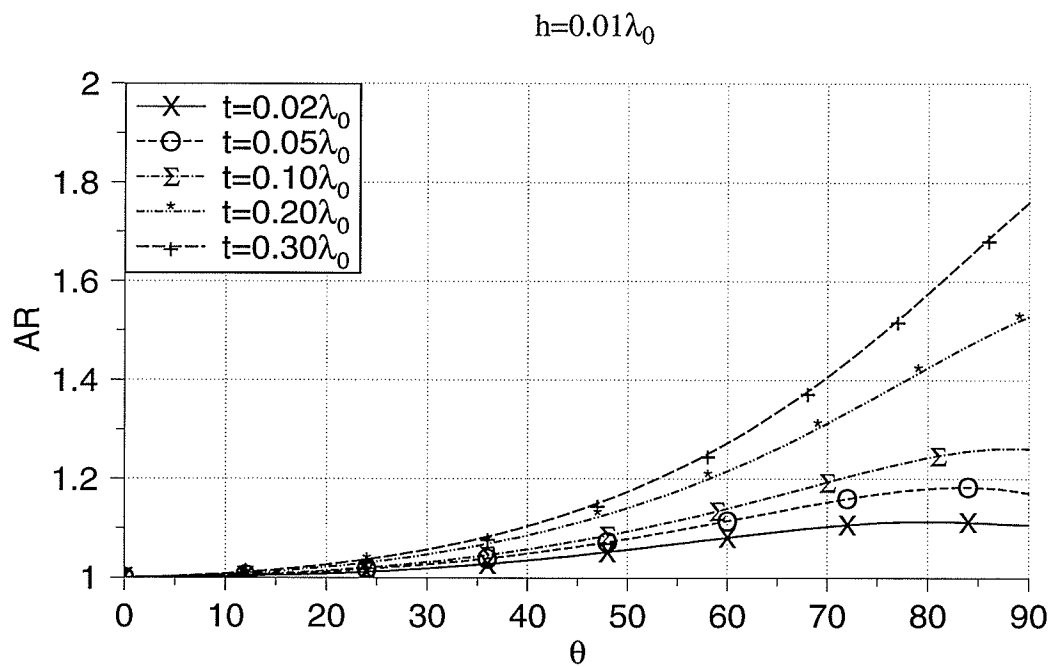


Fig. 5.9. Axial ratio for $g=0.25\lambda_0$

5.5. Summary

This chapter discussed the investigation of the effects of the ground plane and substrate thicknesses, that can be used to optimize the antenna pattern symmetry.

In general, increasing the substrate thickness (h) deteriorates the circular polarization, while it does not significantly affect the gain, except for antennas with larger ground planes. For larger ground planes, increasing h decreases the gain. As a result, h should be kept as small as possible.

Effects of t is more dependant on the ground plane radius, and can be chosen to maximize the gain. It was found that the sizes of t which maximize the gain, also give the best axial ratio and pattern symmetry.

Effects of Finite Ground Plane on the Dielectric Resonator Antenna

6.1. Introduction	102
6.2. Dielectric Resonator Antenna Structure	103
6.3. Analytical Method	105
6.4. Numerical Method	108
6.5. Simulation Results.....	109
6.6. Summary	118

6.1. Introduction

Dielectric resonators (DRs) offer attractive features as antenna elements. These include their small size, mechanical simplicity, high radiation efficiency due to no inherent conductor loss, relatively large bandwidth, simple coupling shape to nearly all commonly used transmission lines, and the advantage of obtaining different radiation characteristics using different modes of the resonator.

The design of dielectric resonator antennas (DRAs) requires information on basic quantities such as the radiated fields, resonant frequency, bandwidth and field distribution inside the resonator. Unfortunately no comprehensive information of this form is available in the literature which can be used by an antenna engineer. The most of work reported so far on DRs related to their use as a circuit element in shielded circuits and therefore radiated fields are generally not considered [19].

The comparison between dielectric resonator antennas and microstrip antennas shows that the dielectric resonator antennas can be more efficient radiators than the microstrip antennas, can achieve wider frequency bandwidth, and can have better power-handling capability. At millimetre-wave frequencies, they have much smaller conducting losses compared to microstrip antennas [20].

The earliest study of cylindrical dielectric resonator antennas belongs to Long et al. [21]. They performed an experimental study of the radiation pattern of a resonant cylindrical DRA. A simple theory utilizing the magnetic wall boundary condition was proposed and compared with measured results. This method is a first order solution which is seen to provide reasonably accurate predictions for the radiation patterns and resonant frequency.

A comprehensive review of the modes and radiation characteristics of DRAs of different

shapes including cylindrical DRA is given by Mongia and Bhartia [19]. Accurate closed form expressions are provided for resonant frequencies, radiation Q-factors, and inside fields of a cylindrical DR.

Kishk et al. [22] computed the radiation pattern of cylindrical dielectric resonator antennas excited by a coaxial probe numerically, using the method of moment. They also investigated the effects of the ground plane size, dielectric constant and resonator dimensions on the radiation pattern.

This chapter is an opening to a future work, study of radiation characteristics of cylindrical dielectric resonator antennas. The same method used for microstrip antenna can be used for dielectric resonator antenna. There are more parameters for a dielectric resonator antenna which can be used to control its performance. One of them is the ratio of radius to height of dielectric resonator and the other one is the excited mode. The emphasis in this study is on the effects of ground plane radius and the ratio of dielectric resonator radius to its height on the gain and radiation patterns.

6.2. Dielectric Resonator Antenna Structure

A DRA consists of a piece of low loss dielectric bulk mounted on supporting plane usually a conductor. The geometry of dielectric can be cylindrical, rectangular, ring cylinder, hemispherical, or half-split cylinder. The geometry of a cylindrical dielectric resonator antenna is shown in Fig. 6.1.

Dielectric resonator antenna offers many attractive features which among the most important ones are the followings.

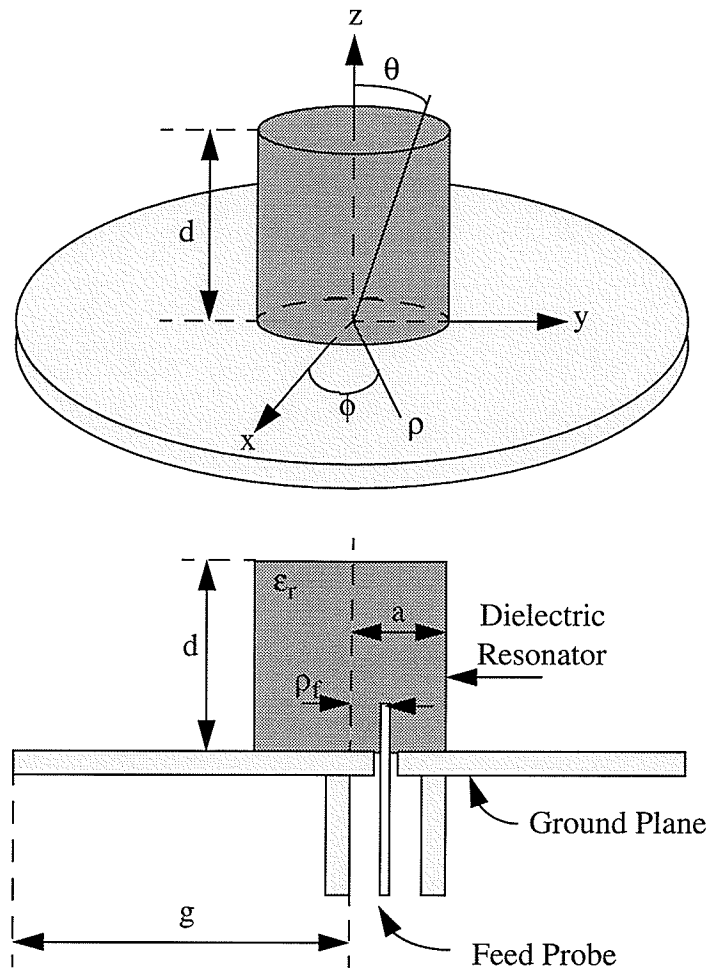


Fig. 6.1. Cylindrical dielectric resonator antenna geometry

- The dimensions of a DRA are of the order of $\lambda_0/\sqrt{\epsilon_r}$, where λ_0 is the free space wavelength and ϵ_r is the dielectric constant of the resonator material. Thus, by choosing a high value of ϵ_r , the size of the DRA can be significantly reduced.
- There is no inherent conductor loss in dielectric resonators. This leads to high radiation efficiency of the antenna.
- DRs offer simple coupling schemes to nearly all transmission lines used at microwave and millimetre-wave frequencies. This make them suitable for integration into different planar

technologies.

- The operating bandwidth of a DRA can be varied over a wide range by suitably choosing resonator parameters.
- Each mode of a DRA has a unique internal and associated external field distribution. Therefore, different radiation characteristics can be obtained by exciting different modes of a DRA [19].

In the present study a cylindrical DRA with coaxial feed probe is considered. The coaxial feed probe is simulated as an infinitesimal dipole. The method of moment is used for simulation, and cylindrical DRA is modelled as a body of revolution.

6.3. Analytical Method

This is a brief review of the simple analytical method proposed by Long et al. [21]. The geometry of the problem is shown in Fig. 6.1. The ground plane is assumed to be infinite, thus image theory can be applied immediately and ground plane can be replaced by an imaged portion of the cylinder extending to $z=-d$; the isolated cylinder is now analysed with an implied boundary condition of zero E_ϕ and E_θ at $z=0$.

An approximate solution for the fields inside such a cylinder can be obtained by assuming that the surfaces are perfect magnetic conductors. Wave functions transverse electric (TE) and transverse magnetic (TM) to z may be postulated as:

$$\psi_{TE_{npm}} = J_n\left(\frac{X_{np}}{a}\rho\right)\left(\frac{\sin n\phi}{\cos n\phi}\right)\sin\left[\frac{(2m+1)\pi z}{2d}\right] \quad (6-1)$$

$$\psi_{TM_{npm}} = J_n\left(\frac{X'_{np}}{a}\rho\right)\left(\frac{\sin n\phi}{\cos n\phi}\right)\cos\left[\frac{(2m+1)\pi z}{2d}\right] \quad (6-2)$$

where J_n is the Bessel function of the first kind.

$$\begin{aligned} J_n(X_{np}) &= 0 \\ J'_n(X'_{np}) &= 0 \\ n &= 1, 2, 3, \dots \\ p &= 1, 2, 3, \dots \\ m &= 0, 1, 2, \dots \end{aligned} \quad (6-3)$$

The resonant frequency of the npm mode is as follows:

$$f_{npm} = \frac{1}{2\pi a \sqrt{\mu\epsilon}} \sqrt{\left\{ \begin{matrix} X_{np}^2 \\ X'_{np}{}^2 \end{matrix} \right\} + \left[\frac{\pi a}{2d} (2m+1) \right]^2} \quad (6-4)$$

where X_{np} is used for TM_{npm} and X'_{np} is used for TE_{npm} . Using Maxwell's equations electric field components for TM_{npm} and magnetic components for TE_{npm} will be determined.

$$\left. \begin{aligned} E_\phi &= \frac{1}{j\omega\epsilon\rho} \frac{\partial^2 \psi}{\partial\phi\partial z} = \frac{n(2m+1)\pi}{2j\omega\epsilon\rho d} J_n\left(\frac{X'_{np}}{a}\rho\right) \sin n\phi \sin \frac{(2m+1)\pi z}{2d} \\ E_z &= \frac{1}{j\omega\epsilon} \left(\frac{\partial^2}{\partial z^2} + k^2 \right) \psi = \frac{1}{j\omega\epsilon} \left(\frac{X'_{np}}{a} \right)^2 J_n\left(\frac{X'_{np}}{a}\rho\right) \cos n\phi \cos \frac{(2m+1)\pi z}{2d} \\ E_\rho &= \frac{1}{j\omega\epsilon} \frac{\partial^2 \psi}{\partial\rho\partial z} = \frac{-\pi X'_{np}(2m+1)}{2j\omega\epsilon a d} J'_n\left(\frac{X'_{np}}{a}\rho\right) \cos n\phi \sin \frac{(2m+1)\pi z}{2d} \end{aligned} \right\} TM_{npm} \quad (6-5)$$

$$\left. \begin{aligned} H_\phi &= \frac{1}{j\omega\mu\rho} \frac{\partial^2 \psi}{\partial\phi\partial z} = -\frac{1}{j\omega\mu\rho} \frac{n(2m+1)\pi}{2d} J_n\left(\frac{X_{np}}{a}\rho\right) \sin n\phi \cos \frac{(2m+1)\pi z}{2d} \\ H_z &= \frac{1}{j\omega\mu} \left(\frac{\partial^2}{\partial z^2} + k^2 \right) \psi = \frac{1}{j\omega\mu} \left(\frac{X_{np}}{a} \right)^2 J_n\left(\frac{X_{np}}{a}\rho\right) \cos n\phi \sin \frac{(2m+1)\pi z}{2d} \\ H_\rho &= \frac{1}{j\omega\mu} \frac{\partial^2 \psi}{\partial\rho\partial z} = \frac{1}{j\omega\mu} \left(\frac{X_{np}}{a} \right) \frac{(2m+1)\pi}{2d} J'_n\left(\frac{X_{np}}{a}\rho\right) \cos n\phi \cos \frac{(2m+1)\pi z}{2d} \end{aligned} \right\} TE_{npm} \quad (6-6)$$

where ρ, ϕ and z are in cylindrical coordinate system, and $k = \omega\sqrt{\mu\epsilon}$. By using these fields, electric and magnetic surface currents can be calculated. ρ', ϕ' and z' are used for the source. The

magnetic surface currents for the TM_{npm} mode are given by:

$$\left. \begin{aligned} M_{z'} &= \frac{n(2m+1)\pi}{2j\omega\epsilon ad} J_n(X'_{np}) \sin n\phi' \sin \frac{(2m+1)\pi z'}{2d} \\ M_{\phi'} &= \frac{1}{j\omega\epsilon} \left(\frac{X'_{np}}{a} \right)^2 J_n(X'_{np}) \cos n\phi' \cos \frac{(2m+1)\pi z'}{2d} \end{aligned} \right\} \text{Sides} \quad (6-7)$$

$$\left. \begin{aligned} M_{\phi'} &= \frac{X'_{np}(2m+1)\pi}{2j\omega\epsilon ad} J'_n \left(\frac{X'_{np}}{a} \rho' \right) \cos n\phi' \\ M_{\rho'} &= \frac{n(2m+1)\pi}{2j\omega\epsilon d \rho'} \left(\frac{X'_{np}}{a} \right)^2 J_n \left(\frac{X'_{np}}{a} \rho' \right) \sin n\phi' \end{aligned} \right\} \text{Top and Bottom} \quad (6-8)$$

For the TE_{npm} mode the electric surface currents are given by:

$$\left. \begin{aligned} J_{z'} &= \frac{-n(2m+1)\pi}{2j\omega\mu ad} J_n(X_{np}) \sin n\phi' \cos \frac{(2m+1)\pi z'}{2d} \\ J_{\phi'} &= \frac{-1}{j\omega\mu} \left(\frac{X'_{np}}{a} \right)^2 J_n(X_{np}) \cos n\phi' \sin \frac{(2m+1)\pi z'}{2d} \end{aligned} \right\} \text{Sides} \quad (6-9)$$

$$J_{\phi'} = J_{\rho'} = 0 \quad \text{Top and Bottom} \quad (6-10)$$

By integrating these surface currents, the electric vector potential for TM_{npm} and magnetic vector potential for TE_{npm} mode can be calculated. For the TM_{npm} mode the electric vector potential components are given by:

$$\begin{aligned} F_{\theta} &= C_1 \{ n(I_2 - I_1) + (-0.5k_p(I_3 + I_4 - I_5 - I_6)) - 2nJ_n(X'_{np})k_0 \sin \theta J_n(k_0 a \sin \theta) D_1 \\ &\quad - J_n(X'_{np})k_p^2 a [J_{n-1}(k_0 a \sin \theta) + J_{n+1}(k_0 a \sin \theta)] D_1 \} \end{aligned} \quad (6-11)$$

$$F_{\phi} = C_2 \{ n(-I_2 - I_1) - 0.5k_p(I_3 - I_4 - I_5 + I_6)$$

$$- J_n(X'_{np})k_p^2 a [J_{n-1}(k_0 a \sin \theta) - J_{n+1}(k_0 a \sin \theta)] D_1 \}$$

where

$$\begin{aligned}
k_0 &= \omega \sqrt{\mu_0 \epsilon_0} \\
k_p &= \frac{X'_{np}}{a}
\end{aligned}
\tag{6-12}$$

$$\begin{aligned}
C_1 &= \frac{(2m+1) \pi^2 j^{n-1}}{j \omega \epsilon d} \frac{1}{4 \pi r} \sin n \phi \cos (k_0 d \cos \theta) \cos \theta \\
C_2 &= \frac{(2m+1) \pi^2 j^{n-1}}{j \omega \epsilon d} \frac{1}{4 \pi r} \cos n \phi \cos (k_0 d \cos \theta)
\end{aligned}
\tag{6-13}$$

$$\begin{aligned}
D_1 &= \frac{(-1)^m}{\left(\frac{(2m+1) \pi}{2d} \right)^2 - (k_0 \cos \theta)^2} \\
I_1 &= \int_0^a J_n(k_p \rho') J_{n-1}(k_0 \rho' \sin \theta) d\rho' \\
I_2 &= \int_0^a J_n(k_p \rho') J_{n+1}(k_0 \rho' \sin \theta) d\rho' \\
I_3 &= \int_0^a J_{n-1}(k_p \rho') J_{n-1}(k_0 \rho' \sin \theta) \rho' d\rho' \\
I_4 &= \int_0^a J_{n-1}(k_p \rho') J_{n+1}(k_0 \rho' \sin \theta) \rho' d\rho' \\
I_5 &= \int_0^a J_{n+1}(k_p \rho') J_{n-1}(k_0 \rho' \sin \theta) \rho' d\rho' \\
I_6 &= \int_0^a J_{n+1}(k_p \rho') J_{n+1}(k_0 \rho' \sin \theta) \rho' d\rho'
\end{aligned}
\tag{6-14}$$

The program written for calculation of radiation patterns is given in the Appendix C.

6.4. Numerical Method

The numerical method of moment as discussed in 2.4 can be used for calculation of the radiation patterns of DRA. Because the cylindrical DRA is an axisymmetric geometry the method of

Body of Revolution can be applied. This method had been already used by Kishk et al. [22] and the numerical data obtained are found to be in good agreement with experimental results.

6.5. Simulatoin Results

Radiation patterns for some sample antennas excited in dominant mode (TM_{110}) are calculated using the analytical and numerical methods. The characteristics of these antennas are given in Table (6-1). For the numerical method a ground plane with radius of $0.3\lambda_0$ was assumed. Figs. 6.2 to 6.5 show the comparison of the radiation patterns. One can observe that as a/d decreases to 0.15 the analytical method fails in prediction of the radiation patterns behaviour. For small a/d a dip appears at $\theta=0^\circ$. In the numerical method this dip is not as high as that one for the analytical method. The experimental results show the same fact [21]. The difference near $\theta=90^\circ$ is because of the finite ground plane.

Table (6-1) Antenna dimensions for TM_{110} mode, $\epsilon_r=8.9$, $t=0.1\lambda_0$ and $g=3.0\lambda_0$

a/d	a/λ_0	d/λ_0	$a(\text{cm})$	$d(\text{cm})$
0.15	0.0990	0.6600	0.3	2.0
0.30	0.1014	0.3379	0.3	1.0
0.50	0.1068	0.2136	0.3	0.6
1.67	0.1710	0.1024	0.5	0.3

A set of antennas with dielectric constant of 4.5 was chosen to investigate the effects of the ground plane radius and a/d on the gain and radiation patterns. A smaller dielectric constant was chosen to have more accuracy in numerical calculations. The dimensions of these antennas are given in Table (6-2).

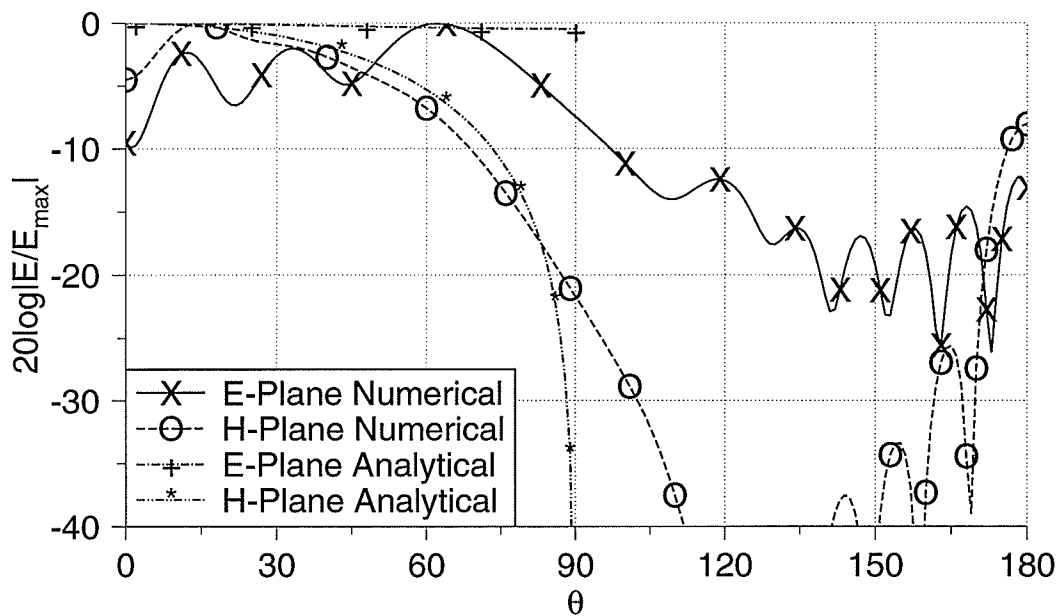


Fig. 6.2. Radiation patterns for the antenna with $a/d=1.67$, $\epsilon_r=8.9$, TM_{110} mode

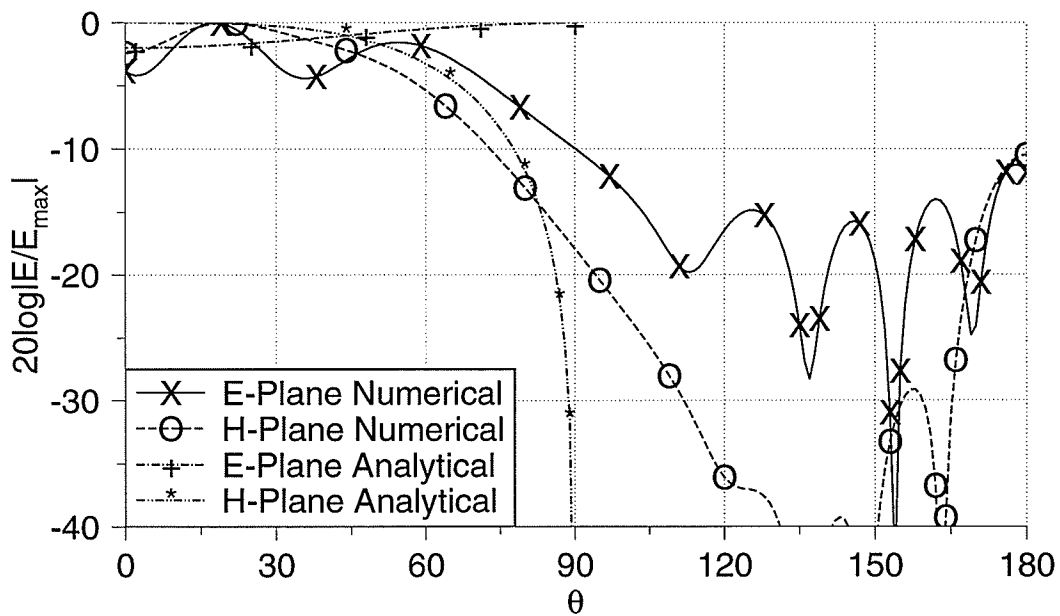


Fig. 6.3. Radiation patterns for the antenna with $a/d=0.5$, $\epsilon_r=8.9$, TM_{110} mode

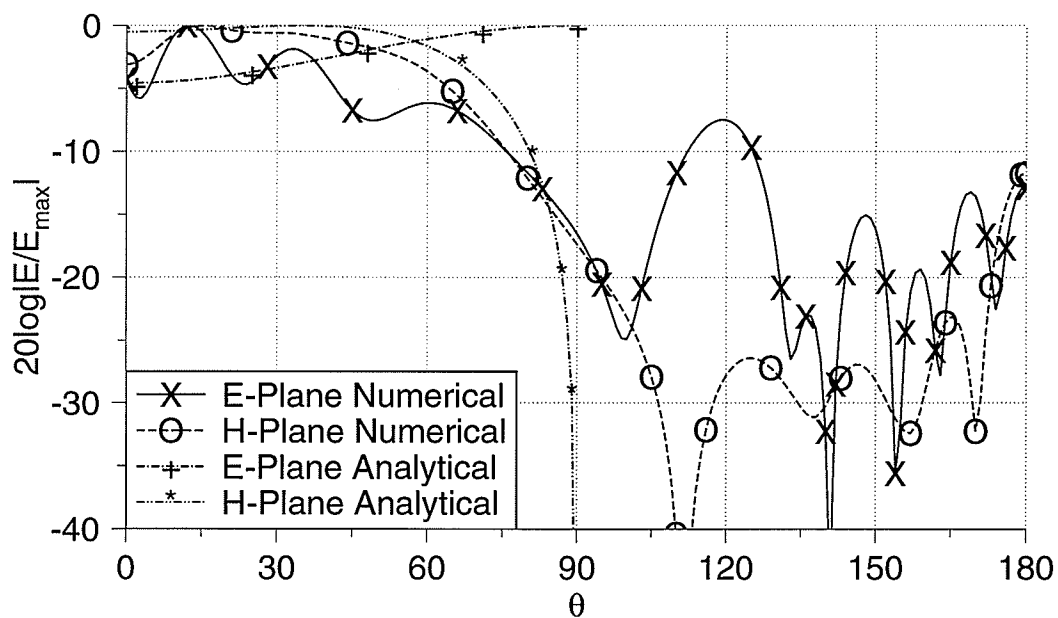


Fig. 6.4. Radiation patterns for the antenna with $a/d=0.3$, $\epsilon_r=8.9$, TM_{110} mode

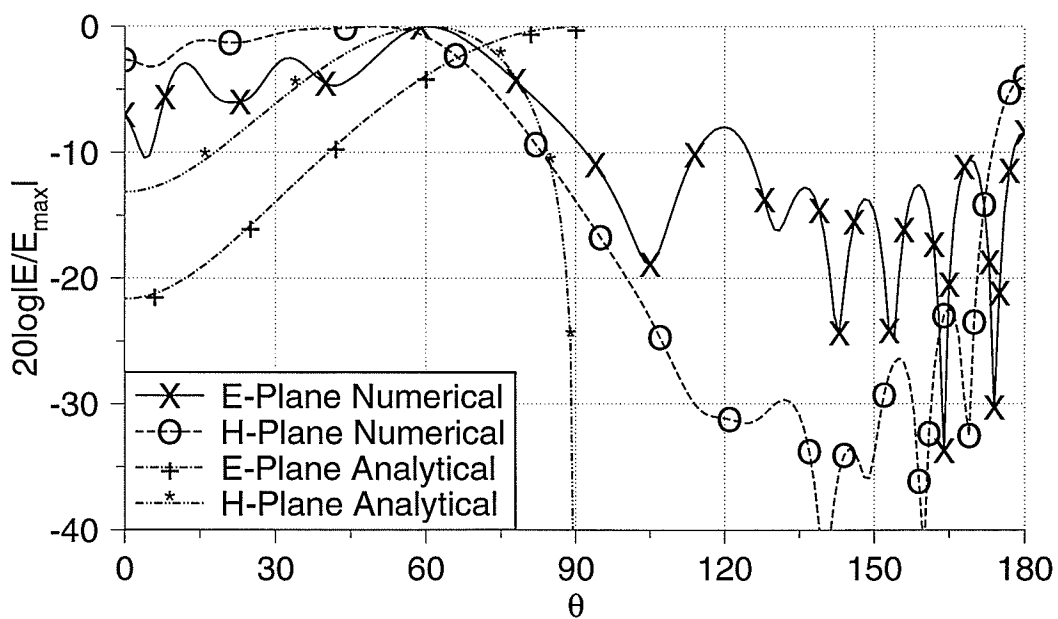


Fig. 6.5. Radiation patterns for the antenna with $a/d=0.15$, $\epsilon_r=8.9$, TM_{110} mode

Table (6-2) Antenna dimensions for TM_{110} mode, $\epsilon_r=4.5$ and $t=0.01\lambda_0$

a/d	a/λ_0	d/λ_0
0.15	0.1393	0.9283
0.30	0.1426	0.4753
0.50	0.1502	0.3003
1.67	0.2404	0.1424

The variation of the gain in terms of the ground plane radius is shown in Fig. 6.6. It shows that for $a/d=0.15$, the gain increases rapidly by increasing the ground plane radius. Note that the maximum gain happens when the ground plane radius is almost equal to the resonator height (d). For larger a/d values the gain does not vary much with the change in the ground plane radius.

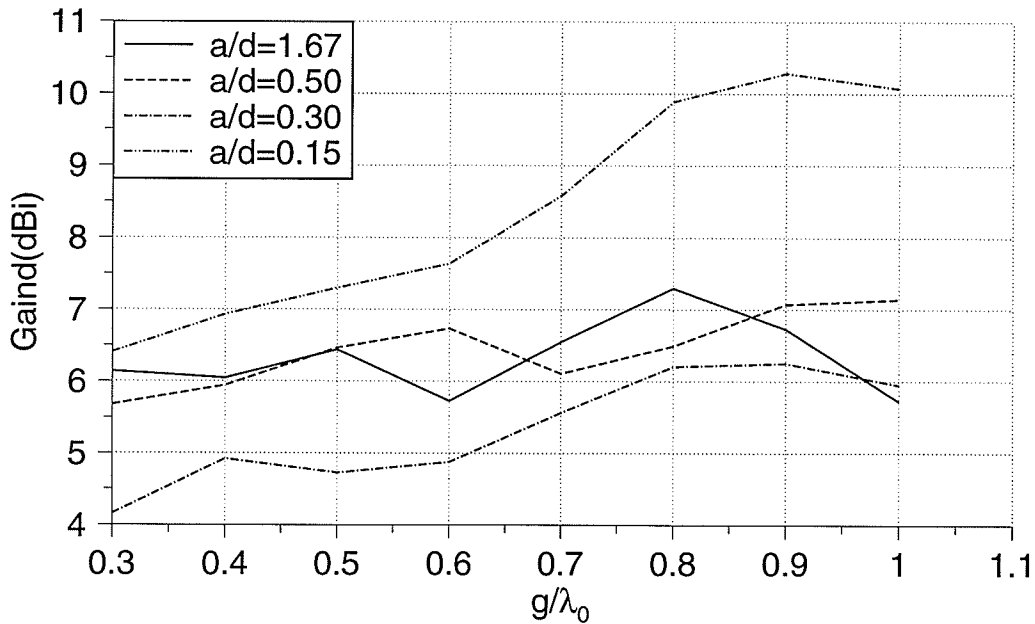


Fig. 6.6. Variation of the gain for dielectric resonator antennas

The variation of radiation patterns are investigated by measuring the backlobe level, the half power beamwidth of the E and H-plane radiation patterns and the difference between maxima of the E and H-plane patterns. Generally the backlobe level decreases by increasing the ground plane radius (Fig. 6.7). For $a/d=0.15$ the backlobe level is smaller than that of other antennas. Half power beamwidth of both E and H-plane radiation patterns, for large a/d values, decreases initially and after a while starts increasing, and then it decreases again. For $a/d=0.15$ both half power beamwidths decreases to around 25° (Figs. 6.8 and 6.9). The difference between the E and H-plane maxima is always small for $a/d=0.15$, but for larger a/d values, it increases rapidly after $g=0.8\lambda_0$ (Fig. 6.10).

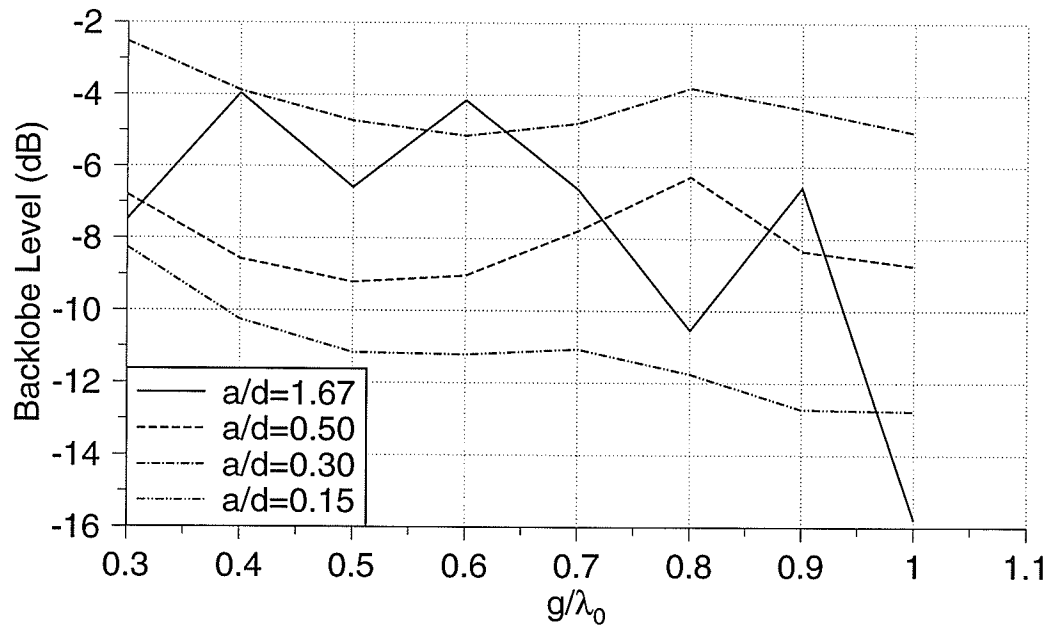


Fig. 6.7. Backlobe level variation with the ground plane radius

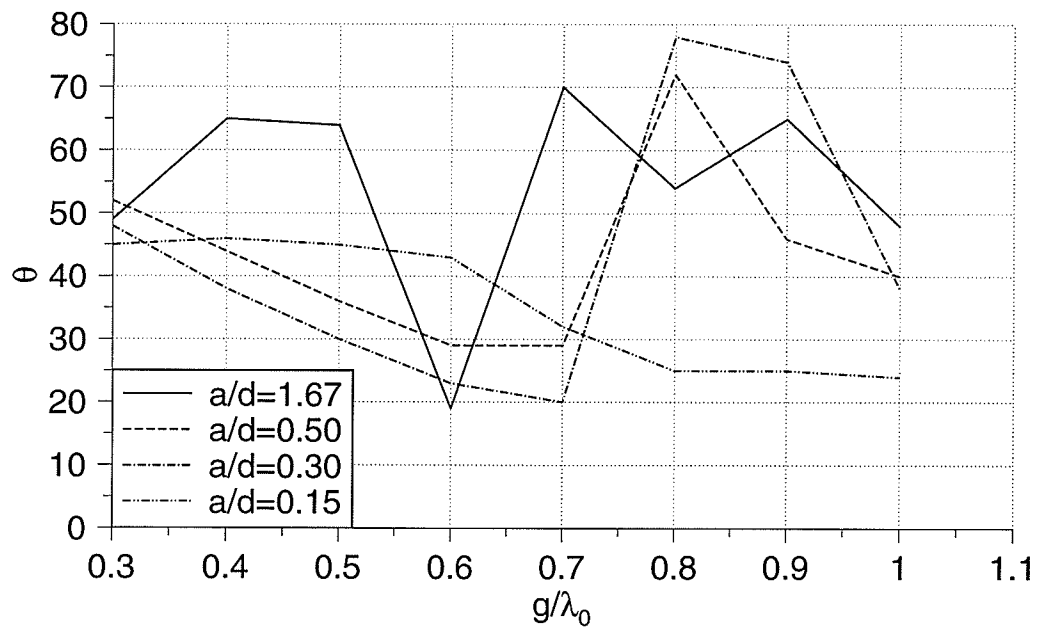


Fig. 6.8. E-plane half power beamwidth

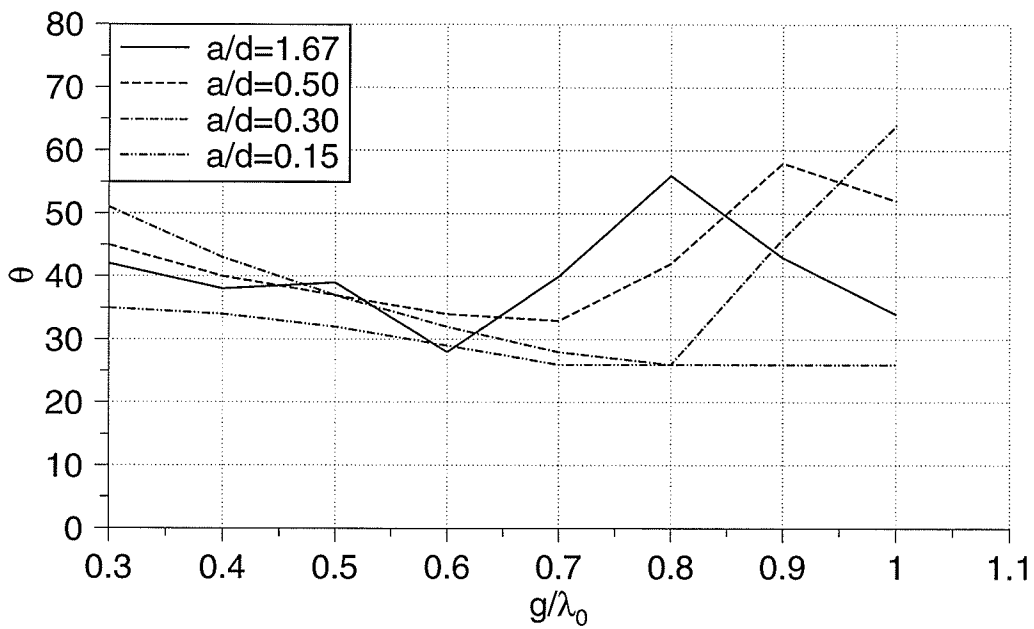


Fig. 6.9. H-plane half power beamwidth

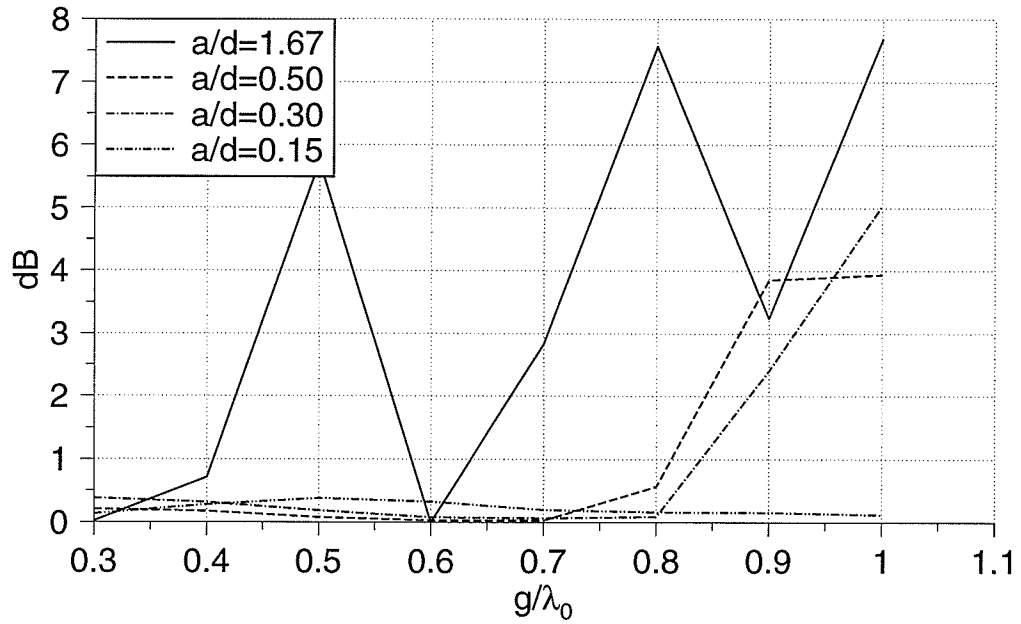


Fig. 6.10. *E* and *H*-plane patterns peak difference

The axial ratio for $a/d=1.67$ is better when the ground plane radius is small, but by increasing the ground plane radius, it improves for smaller values of a/d and degrades for its larger values. Figs. 6.11 and 6.12 show the axial ratios for two different ground plane radii. The radiation patterns for these ground plane radii and for $a/d=0.15$ and 1.67 are compared in Figs. 6.13 and 6.14.

Increasing the ground plane thickness does not seem to have a great effect on the gain, but it degrades the circular polarization. Fig. 6.15 shows the axial ratio for the sample antennas with $a/d=0.5$ and $g=0.3\lambda_0$.

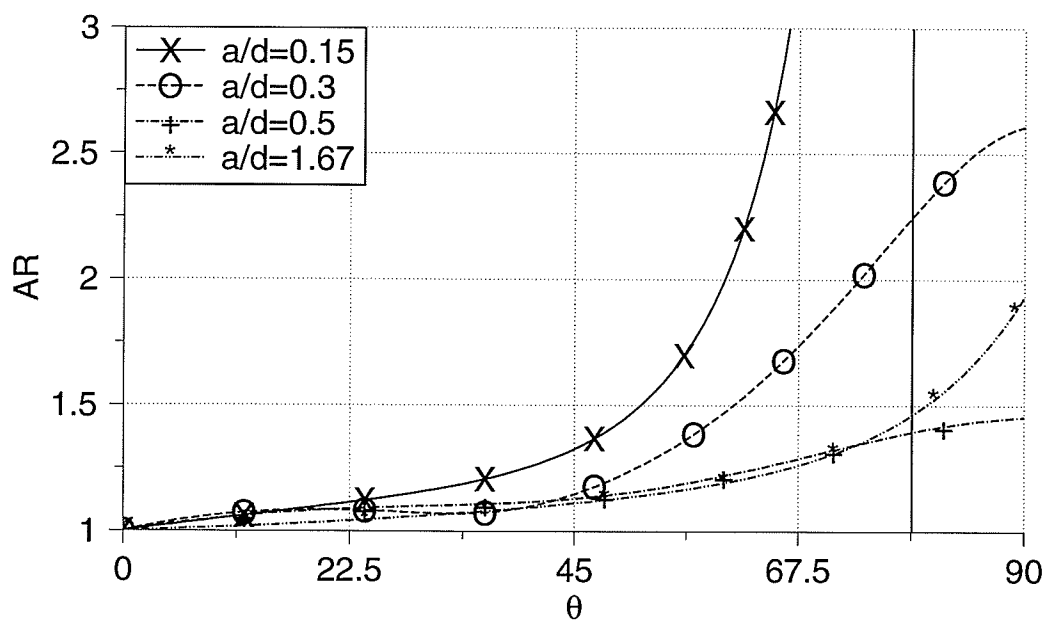


Fig. 6.11. Axial ratio for the antennas with $g=0.3\lambda_0$

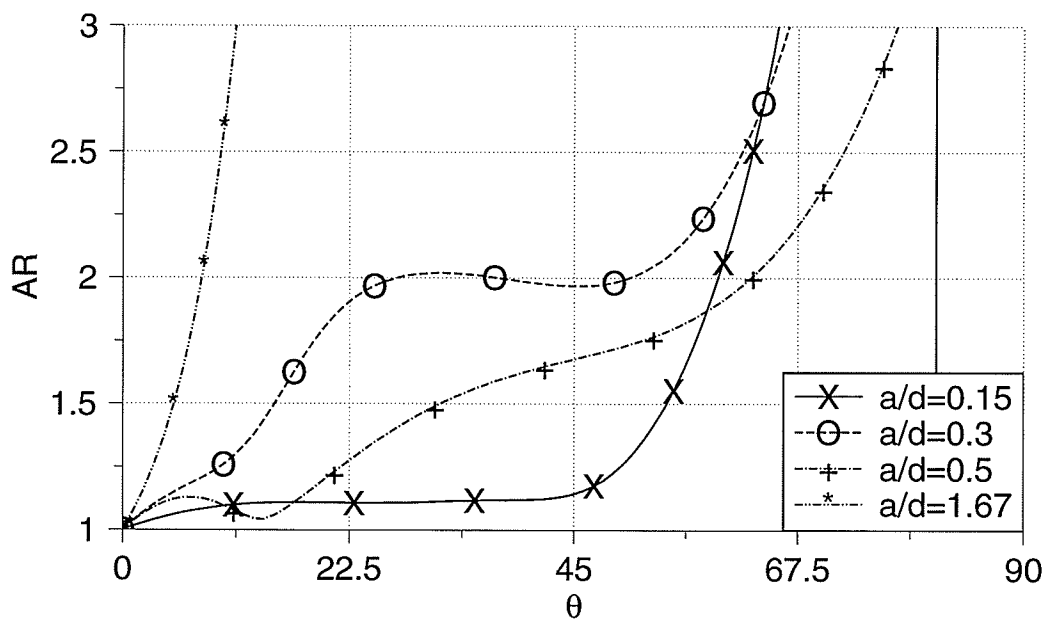


Fig. 6.12. Axial ratio for the antennas with $g=1.1\lambda_0$

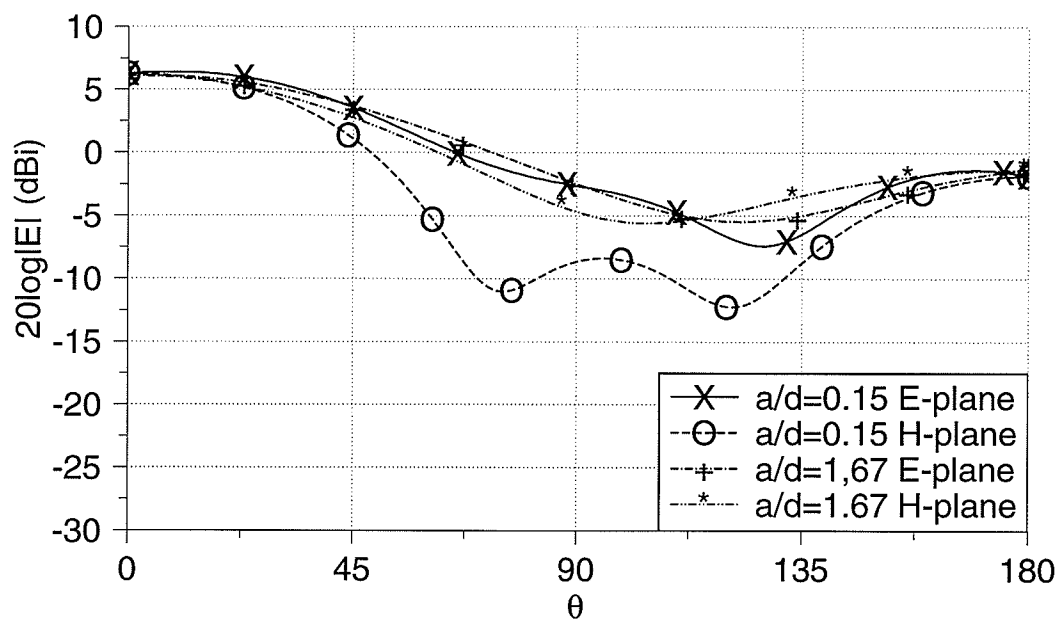


Fig. 6.13. Radiation patterns for the antennas with $g=0.3\lambda_0$

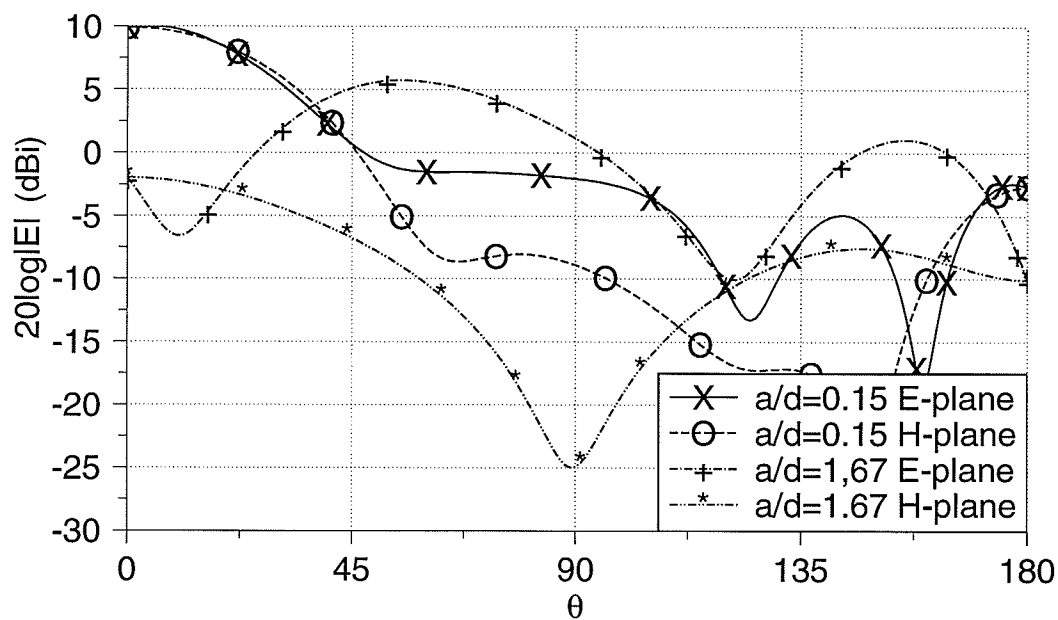


Fig. 6.14. Radiation patterns for the antennas with $g=1.1\lambda_0$

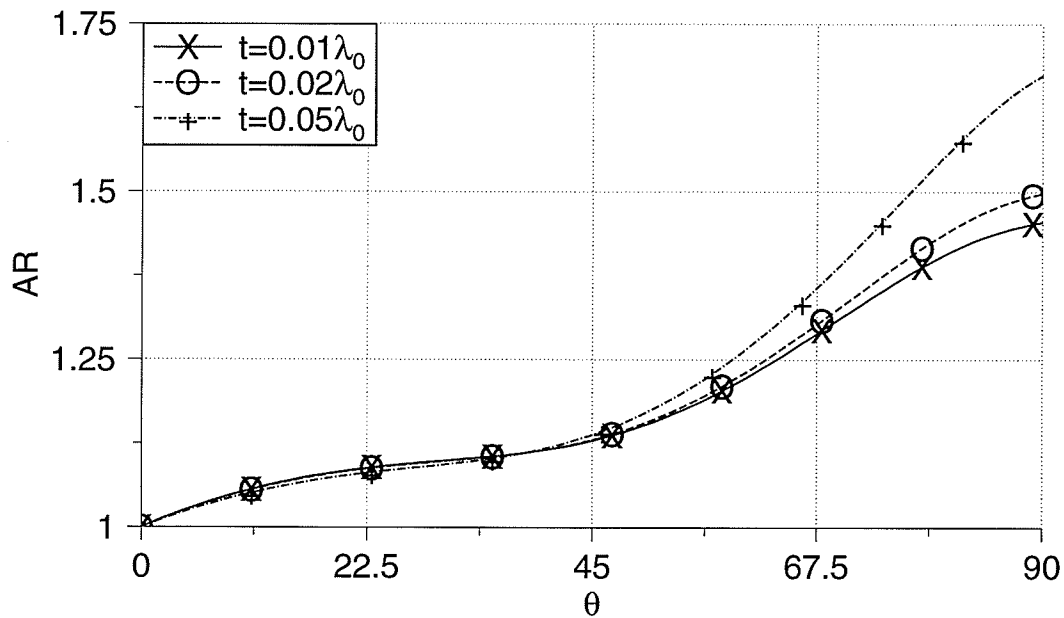


Fig. 6.15. Axial ratio for $a/d=0.5$, $g=0.3\lambda_0$ and different ground plane thicknesses

6.6. Summary

An introductory investigation of the effects of geometrical parameters of cylindrical dielectric resonator antennas was made. The effects of ground plane radius and the radius to height ratio of dielectric resonator (a/d) were studied.

By decreasing a/d , better gain, especially for smaller a/d values, can be obtained. A small a/d also offers better equality of the E and H-plane radiation patterns, smaller backlobe level and narrower beamwidth.

Increasing the ground plane radius, although increases the gain and decreases the backlobe level, degrades the E and H-plane patterns equality.

Increasing the ground plane thickness does not change the gain, but degrades the pattern symmetry.

Conclusion

7.1. Summary 120

7.2. Future Work 122

7.1. Summary

A study of the effects of various physical and electrical parameters of microstrip antennas on their radiation characteristics was carried out. A numerical method based on the method of moment was utilized. In this method surface field and currents distribution are computed accurately. By choosing a circular microstrip patch antenna, the moment method for Body of Revolution is applicable. In this method the unknown surface currents are expanded in terms of Fourier series in the azimuthal coordinate.

The first four modes were studied. Also some innovative ground plane shapes were designed. A similar work was performed for dielectric resonator antennas.

The following conclusions were drawn:

- The ground plane radius has significant effects on the gain, radiation patterns and circular polarization of microstrip antennas.

The gain can be maximized by selecting a proper size for the ground plane radius. This size depends on the excited mode and is almost independent of the substrate permittivity. The gain increases rapidly after a certain ground plane radius, which the value of it depends on the excited mode.

The radiation pattern characteristics and gain have periodic behaviour with the change in the ground plane radius.

By choosing the right excited mode, substrate permittivity and the ground plane radius, circular polarization with excellent axial ratio is achievable.

- The ground plane shape can be modified in order to control the radiation pattern.

Adding a rim to the ground plane to form an open cavity, provides an antenna with high gain and narrow beamwidth. Also adding a quarter-wavelength chock to this

rim decreases the backlobe level. Extending the ground plane in the back and adding the rim to it provides wider a beamwidth and flatter radiation patterns.

- The ground plane and substrate thicknesses can be used as control parameters, especially when the ground plane radius is limited by application requirements. It was observed that the substrate thickness does not have an important effect on the gain, but its increase degrades the circular polarization and increases the backlobe level. As a result the substrate thickness must be kept as small as possible. It was found that the sizes of the ground plane thickness which maximize the gain also give the best axial ratio and pattern symmetry.
- Dielectric resonator antennas have many features common with microstrip antennas. Thus, the same method can be applied for dielectric resonator antenna simulation. There are more parameters for dielectric resonator antennas that affect the radiation characteristics and can also be investigated. Among these parameters the ratio of the dielectric radius to its height (a/d) and the excited modes can be named. The antennas with smaller a/d show good performance and can be used for different applications.

7.2. Future Work

In this area, there are numerous subjects which need more careful investigations, some of which are listed below.

- The effects of electrical and geometrical parameters on the input impedance and frequency bandwidth should be studied as well. For frequency bandwidths concerning the antenna radiation characteristics, such as the gain and axial ratio the MBES package can be used. But, for the impedance bandwidth computation another method must be applied. Note that in MBES package the excitation is simulated by infinitesimal dipoles and no boundary condition was forced on the feed probe itself. For this purpose, other numerical methods such as Finite-Difference Time-Domain can be utilized.
- A study on the surface currents can be performed in order to find reasons for the behaviour of the gain and radiation patterns with the change in the ground plane radius. A mathematical explanation may be found for the results concluded in the present study.
- This study can be extended to dielectric resonator antennas. They have more attractive features than microstrip antennas and more parameters for controlling the radiation characteristics. The higher order modes can be considered.
- More experiments are needed to confirm the simulation results. These experiments can be designed for the higher order modes, different ground plane shapes and also for dielectric resonator antennas.

Appendix A Patch Size Calculation

```

/*****
/*  name: compa.c
/*  written by: Sima Noghanian
/*  date : June, 1995
/*  This program computes the patch radius for the TMn1 mode. It uses Newton
/*  method.
*****/
#include <stdio.h>
#include <stdlib.h>
#include <math.h>

#define PI 3.1415926524
#define ERROR 1e-7

static float er,h,knm,ae;
/* zeros of derivative of Bessel's functions */
static const float k[4]={ 1.84118,3.05424,4.20119,5.317};

void init(void);          /* Initialization routine */
float func(float x);      /* f(x) */
float dfunc(float x);     /* df(x)/dx */
float newton(float acc,float x0);

/*****

void main(void)
{
    float x;
    init();
    x=newton(ERROR,ae);
    printf("\n\tx= %10.8f,\tf(x)= %e\n",x,func(x));
}

*****/

void init(void)
{
    int n;
    printf("\n\tPlease enter the information:");
    printf("\n Epsilon Relative= ");
    scanf("%f",&er);

    /* the TMn1 mode */

```

```

printf(" n= ");
scanf("%d",&n);
printf(" Substrate height= ");
scanf("%f",&h);
knm=k[n-1];
ae=knm/(2*PI*sqrt(er));
}

/*****/

float func(float x)
{
float a,b,c,d;
a=knm/(2*PI*sqrt(er));
b=2*h/(PI*er);
c=PI/2/h;
d=1.7726;
return(a-x*sqrt(1+b/x*(log(c*x)+d)));
}

/*****/

float dfunc(float x)
{
float a,b,c,d;
a=knm/(2*PI*sqrt(er));
b=2*h/(PI*er);
c=PI/2/h;
d=1.7726;
return(-(2*x+b*(log(c*x)+d+1))/(2*x*sqrt(1+b/x*(log(c*x)+d))));
}

/*****/

float newton(float acc,float x0)
{
float xn;
xn=x0;
do
{
xn=xn-func(xn)/dfunc(xn);
} while(func(xn)>acc);
return xn;
}
/*****/

```

Appendix B Gain and Axial Ratio Calculation

```

/*****
/* name: cgain.c
/* written by: Sima Noghian
/* date: July 12, 1995
/* This program reads a *.fld file (generated by MBES package) and calculates the
/* gain. Then divides each value of magnitude of the far field by the gain and writes
/* them in a similar file named *.n.fld. It also calculates the axial ratio and writes the
/* results in the *.ar
*****/

#include <stdio.h>
#include <math.h>
#include <string.h>

#define PI 3.141592654

int readdata(FILE *fp);
float compgain(void);
void writedata(FILE *fpi, FILE *fpo);
void compar(char *output);

static float **et, **ep, **etotal;
static float **etp, **epp;
static float *ar;
static float emax=0;
static float dphi, dtheta;
static int nphi, ntheta;

static float gain;

void main(int argc, char *argv[])
{
    FILE *fpi, *fpo;
    char inputfilename[20], outputfilename[20], output[20];

    /* opening input file */
    /* reading E field from *.fld file */
    /* computing gain
       
$$G = 4 \cdot \pi \cdot |E_{max}|^2 / |E_{av}|^2$$

       
$$|E_{av}| = \text{Sigma}(|E(\theta, \phi)|^2 \cdot \sin(\theta) \cdot d\theta \cdot d\phi) / (\theta = 0 \text{ to } 180, \phi = 0 \text{ to } 360)$$

    */
    /* writing data in output file */

    /* computes the axial ratio */
    /* et=E(theta) ep=E(phi) etotal=|E|
       /* etp=Phase(E(theta)) epp=Phase(E(phi))
       /* ar=axial ratio(theta)
       /* emax=max|E|
       /* dphi=delta(phi) dtheta=delta(theta)
       /* nphi=number of points for phi
       /* ntheta=number of points for theta
    */
    /* gain */
}

```



```

if(argc<2)
{
    printf("Enter input filename[.fld]:");
    scanf("%s",&inputfilename);
}
else strcpy(inputfilename,argv[1]);
strcpy(outputfilename,inputfilename);
strcpy(output,inputfilename);
strcat(inputfilename,".fld");
fpi=fopen(inputfilename,"r");
if(fpi==NULL) perror("File opening error!");

/* reading data from *.fld file */
if(readdata(fpi))
{
    perror("File reading error");
    exit(0);
}

/* computation of gain */
if(!(gain=compgain()))
{
    perror("Divide by zero");
    exit(0);
}

/* computation of axial ratio */
compar(output);
printf("\n\tGain = %f = %fdB\n",gain,(10.*log10(gain)));
fclose(fpi);

/* opening output file and writing results */
printf("\nWriting data in output file. Please wait.\n");
strcat(outputfilename,"n.fld");
fpi=fopen(inputfilename,"r");
fpo=fopen(outputfilename,"w");
if(fpo==NULL) perror("File opening error!");
writedata(fpi,fpo);
fclose(fpi);
fclose(fpo);
}

/*****/

int readdata(FILE *fp)
{

```

```

float firstp,firstt;
int i,j;
char dummy[20],cphi[5],ctheta[8];
float temp;

/* reading the header
  MBES v2.4 (c)1992 CADCAD Technology Inc. [CADCAD#920318]
  reverse
*/
for(i=0;i<67;i++)
  j=getc(fp);

/* reading phi characteristics for example:
  5 0.00000E+00 0.90000E+02 phi
*/
fscanf(fp,"%d",&nphi);
fscanf(fp,"%e",&firstp);
fscanf(fp,"%e",&dphi);
fscanf(fp,"%s",&cphi);

/* reading theta characteristics for example:
  181 0.00000E+00 0.10000E+01 theta
*/
fscanf(fp,"%d",&ntheta);
fscanf(fp,"%e",&firstt);
fscanf(fp,"%e",&dtheta);
fscanf(fp,"%s",&ctheta);

/* checking full revolution */
if(((float)(nphi-1)*dphi)!=360)
{
  printf("\nphi must vary from 0 to 360");
  return(1);
}

if(((float)(ntheta-1)*dtheta)!=180)
{
  printf("\ntheta must vary from 0 to 180");
  return(1);
}

/* memory allocation for et,ep and etotal */
et=(float **)malloc(nphi*sizeof(float *));
etp=(float **)malloc(nphi*sizeof(float *));
ep=(float **)malloc(nphi*sizeof(float *));
epp=(float **)malloc(nphi*sizeof(float *));

```

```

etotal=(float **)malloc(nphi*sizeof(float *));

if((et==NULL) || (ep==NULL) || (etp==NULL) || (epp==NULL) || (etotal==NULL))
{
    printf("\nMemory allocation error");
    return(1);
}

for(i=0;i<nphi;i++)
{
    et[i]=(float *)malloc(ntheta*sizeof(float));
    etp[i]=(float *)malloc(ntheta*sizeof(float));
    ep[i]=(float *)malloc(ntheta*sizeof(float));
    epp[i]=(float *)malloc(ntheta*sizeof(float));
    etotal[i]=(float *)malloc(ntheta*sizeof(float));
    if((et[i]==NULL) || (ep[i]==NULL) || (etotal[i]==NULL))
    {
        printf("\nMemory allocation error");
        return(1);
    }
}
ar=(float *)malloc(ntheta*sizeof(float));
if(ar==NULL)
{
    printf("\nMemory allocation error");
    return(1);
}

/* reading the first line:
   mag(etheta)  phase(etheta)  mag(ephi)  phase(ephi)
*/
for(i=0;i<4;i++) fscanf(fp,"%s",&dummy);

/* reading et and ep */
for(i=0;i<nphi;i++)
for(j=0;j<ntheta;j++)
{
    fscanf(fp,"%e",&et[i][j]);    /* mag(etheta) */
    fscanf(fp,"%e",&etp[i][j]);   /* pahse(etheta) */
    fscanf(fp,"%e",&ep[i][j]);    /* mag(ephi) */
    fscanf(fp,"%e",&epp[i][j]);   /* phase(ephi) */

    etotal[i][j]=sqrt(pow(et[i][j],2.)+pow(ep[i][j],2.));
    if(etotal[i][j] >= emax) emax=etotal[i][j];
}

```

```

    return(0);
}

/*****

float compgain(void)
{
    float s,g,dp,dt;
    int i,j;

    /* calculation of lElav */
    s=0;
    dp=dphi*PI/180.;
    dt=dtheta*PI/180.;
    for(i=0;i<nphi-1;i++)
        for(j=0;j<ntheta-1;j++)
            s+=etotal[i][j]*etotal[i][j]*sin(PI/180.*(float)j)*dp*dt;

    /* calculation of gain */
    if(s!=0) g=4.*PI*emax*emax/s;
    else g=0.0;
    return(g);
}

*****/

void compar(char *output)
{
    FILE *fout;
    float el,er,e1,e2r,e2i,delta,g;
    int i,j;
    i=1;

    /* opening the output file */
    strcat(output,".ar");
    fout=fopen(output,"w");
    if(fout==NULL)
    {
        perror("File opening error!");
        return;
    }

    /* calculation of axial ratio */
    for(j=0;j<ntheta;j++)
    {
        e1=et[0][j];

```

```

    delta=(epp[i][j]-etp[0][j]+90)*PI/180.;
    e2r=ep[i][j]*cos(delta);
    e2i=ep[i][j]*sin(delta);
    el=sqrt(((e1-e2i)*(e1-e2i)+(e2r*e2r))*0.5);
    er=sqrt(((e1+e2i)*(e1+e2i)+(e2r*e2r))*0.5);
    ar[j]=(el+er)/(el-er);
    g=sqrt(gain)/emax;
    fprintf(fout,"%f\t%f\t%f\t%f\n",j*dtheta,et[0][j]*g,ep[i][j]*g,ar[j]);
}

/* closing the output file */
fclose(fout);
}

/*****/

void writedata(FILE *fpi,FILE *fpo)
{
    int i,j,k;
    float temp[4],g;

    g=sqrt(gain)/emax;
    for(i=0;i<209;i++)
    {
        j=getc(fpi);
        putc(j,fpo);
    }

    for(i=0;i<nphi;i++)
    for(j=0;j<ntheta;j++)
    {
        for(k=0;k<4;k++)
            fscanf(fpi,"%f",&temp[k]);
        fprintf(fpo," %7.7e %7.7e %7.7e %7.7e\n",
            (temp[0]*g),temp[1],(temp[2]*g),temp[3]);
    }
}

/*****/

```

Appendix C Dielectric Resonator Antenna Radiation Pattern Calculation

```

/*****/
/* name: dr.c */
/* written by: Sima Noghanian */
/* date: May, 1995 */
/* This program computes the far fields of a cylindrical dielectric resonator */
/* antennas for the TMnpm and TEnpm modes. */
/*****/

#include <stdio.h>
#include <math.h>
#include <string.h>
#include <ctype.h>

#define ACC 60.0
#define BIGNO 1.0e10
#define BIGNI 1.0e-10
#define PI 3.141592654
#define cv 3.e10 /* light velocity(cm/s) */
#define e0 8.841941284e-12 /* air permittivity */

/*****/

float bess(int v,float x); /* computes Bessel's function of first order */
void computeI(void); /* computes six integrals,
(21)-(26) in paper */

void init(void); /* initiation */
float computeFt(void); /* computes F_sub_Theta */
float computeFp(void); /* computes F_sub_Phi */
float computeAt(void); /* computes A_sub_Phi */
float computeAp(void); /* computes A_sub_Theta */
float findmax(float *f); /* finds the maximum of element of an array */

/*****/

/* abscissas for Gauss_Legendre integration */
const float xintegral[10]=
{-0.973906528517172,-0.865063366688985,-0.679409568299024,-0.433395394129247,
-0.148874338981631,0.148874338981631,0.433395394129247,0.679409568299024,
0.865063366688985,0.973906528517172};

/* weight factors for Gauss_Legendre integration */

```

```

const float wintegral[5]=
{0.295524224714753,0.269266719309996,0.219086362515982,
0.149451349150581,0.066671344308688};

/* Zeros of J'n(x') */
const float jpzero[3][6]=
{{3.832,1.841,3.054,4.201,5.317,6.416},
{7.016,5.331,6.706,8.015,9.282,10.520},
{10.173,8.536,9.969,11.346,12.682,13.987}};

/* Zeros of Jn(x) */
const float jzero[3][6]=
{{2.405,3.832,5.136,6.380,7.588,8.771},
{5.520,7.016,8.417,9.761,11.065,12.339},
{8.654,10.173,11.620,13.015,14.372,15.7}};

/*****/

static float k0; /* free space wave number */
static float kp; /* xnp/a */
static float a; /* diameter of cylinder */
static float d; /* height of cylinder */
static float er; /* relative permittivity */
static float phi,theta;
static float I[6]; /* six integrals 21-26 of paper */
static int n,m,p; /* mode index */
static float *ft,*fphi; /* F_sub_Theta and F_sub_Phi */
static float f; /* resonant frequency */
static float xnp;
static float jnxnp,jnk1ksa,jnm1ksa,jnp1ksa;
static float ks,sint,cos,D1,C1,C2,C3;
static int step; /* steps of theta and phi */
static char em; /* TE/TM flag */

/*****/

void main(void)
{
int i;
char *filename,*ftemp; /* output file name storage */
float maxft,maxfp; /* maximum of Ftheta and Fphi */
FILE *fp1,*fp2; /* output file pointers */
float max(float a,float b);

/* opening output file */
filename=(char *)malloc(20*sizeof(char));

```

```

ftemp=(char *)malloc(25*sizeof(char));
if(filename==NULL || ftemp==NULL)
{
    perror("Memory allocation error");
    exit(0);
}

printf("Enter your output filename: ");
scanf("%s",filename);
strcpy(ftemp,filename);
strcat(ftemp,".theta");
fp1=fopen(ftemp,"w");
strcpy(ftemp,filename);
strcat(ftemp,".phi");
fp2=fopen(ftemp,"w");
if((fp1==NULL) || (fp2==NULL))
{
    perror("Output file opening error");
    exit(0);
}

init();

/* computation of F or A */
for(i=0;i<=step;i++)
{
    sint=sin(theta);
    cost=cos(theta);
    ks=k0*sint;
    jnm1ksa=bess(n-1,ks*a);
    jnksa=bess(n,ks*a);
    jnp1ksa=bess(n+1,ks*a);
    C3=(float)(2*m+1);
    D1=pow(-1.,m)/((C3*C3*PI*PI/4./d/d)-(k0*k0*cost*cost));
    C1=cost*cos(k0*d*cost);
    C2=cos(k0*d*cost);
    C3=C3/(2.*PI*f*er*e0*d);
    if(em=='m')
    {
        computeI();
        ft[i]=C3*C1*computeFt();
        fphi[i]=C3*C2*computeFp();
    }
    else if(em=='e')
    {
        ft[i]=computeAt();
    }
}

```



```

        fphi[i]=computeAp();
    }
    theta+=PI/(float)step;
}

/* writing results */
maxft=findmax(ft);
maxfp=findmax(fphi);
theta=-90.0000;
for(i=0;i<=step;i++)
{
    fprintf(fp1,"%f\t%f\n",theta,max((20.*log10(fabs(ft[i]/maxft))),-60.));
    fprintf(fp2,"%f\t%f\n",theta,max((20.*log10(fabs(fphi[i]/maxfp))),-60.));
    theta+=180.0000/(float)step;
}
printf("\n\tMax. ftheta = %f\n\tMax. fphi = %f\n\tResonant freq =%5.2e\n",
        ,maxft,maxfp,f);
}

/***** subroutine init *****/
/* This subroutine initiates some variables such as a and d and epsilon relative. */
/*****/

void init(void)
{

    printf("\nPlease enter these information: ");
    printf("\n\t\t a(cm) = ");
    scanf("%f",&a);
    printf("\n\t\t d(cm) = ");
    scanf("%f", &d);
    printf("\n\t\t Epsilon relative = ");
    scanf("%f",&er);
    printf("\n\t\t TE or TM (e/m) : ");
    scanf("%s",&em);
    printf("\n\t\t n = ");
    scanf("%d",&n);
    printf("\n\t\t p = ");
    scanf("%d",&p);
    printf("\n\t\t m = ");
    scanf("%d",&m);
    printf("\n\t\t step = ");
    scanf("%d",&step);

    theta=-PI/2.;
    if((em==tolower(em))=='e') xnp=jzero[p-1][n];

```

```

else if(em=='m') xnp=jpzero[p-1][n];
else {perror("Not correct mode!"); exit(0);}

ft=(float *)malloc((step+1)*sizeof(float));
if(ft==NULL) { perror("Memory allocation error"); exit(0); }

fphi=(float *)malloc((step+1)*sizeof(float));
if(fphi==NULL) { perror("Memory allocation error"); exit(0); }

f=4.774648293e9/a*
    sqrt((xnp*xnp+pow((double)((float)(2*m+1)*PI*a/d/2.),2.))/er);
k0=2*PI*f/cv;
kp=xnp/a;
jnxnp=bess(n,xnp);
}

/***** subroutine computeI *****/
/* This subroutine computes 6 integrals (from 0 to a): */
/* I1=integral of (Jn(kpx)Jn-1(k0asin(theta)))dx */
/* I1=integral of (Jn(kpx)Jn+1(k0asin(theta)))dx */
/* I1=integral of (Jn-1(kpx)Jn-1(k0asin(theta)))xdx */
/* I1=integral of (Jn-1(kpx)Jn+1(k0asin(theta)))xdx */
/* I1=integral of (Jn+1(kpx)Jn-1(k0asin(theta)))xdx */
/* I1=integral of (Jn+1(kpx)Jn+1(k0asin(theta)))xdx */
/* It uses integration subroutine to compute integrals and also JnJm to */
/* compute product of Jn(kpa)Jm(k0asin(theta)) */
/* It uses Gauss quadrature method to compute integrals and maps Gauss */
/* points. */
/*****/

void computeI(void)
{
    float jnjm[6][10];
    float xs[10];
    int i;

    float integration(float f[]);
    float JnJm(int v,int w,float x);

    for(i=0;i<10;i++)
    {
        xs[i]=0.5*a*(1+xintegral[i]);
        jnjm[0][i]=JnJm(n,n-1,xs[i]);
        jnjm[1][i]=JnJm(n,n+1,xs[i]);
        jnjm[2][i]=JnJm(n-1,n-1,xs[i])*xs[i];
        jnjm[3][i]=JnJm(n-1,n+1,xs[i])*xs[i];
    }
}

```

```

    jnjm[4][i]=JnJm(n+1,n-1,xs[i])*xs[i];
    jnjm[5][i]=JnJm(n+1,n+1,xs[i])*xs[i];
}

I[0]=integration(jnjm[0]);
I[1]=integration(jnjm[1]);
I[2]=integration(jnjm[2]);
I[3]=integration(jnjm[3]);
I[4]=integration(jnjm[4]);
I[5]=integration(jnjm[5]);
}

/***** computeFt subroutine *****/
/* This routine computes Ftheta */
/*****

float computeFt(void)
{
    float ft;

    ft=(float)n*(I[1]-I[0]) - (0.5*kp*kp*(I[2]+I[3]-I[4]-I[5])) +
        D1*jnxnp*( (-2.*(float)n*k0*sint*jnksa) - (kp*kp*a*(jnm1ksa+jnp1ksa)) );
    return(ft);
}

/***** computeFp subroutine *****/
/* This routine computes Fphi */
/*****

float computeFp(void)
{
    float fphi;

    fphi=(float)n*(-I[1]-I[0]) - (0.5*kp*kp*(I[2]-I[3]-I[4]+I[5])) -
        D1*jnxnp*kp*kp*a*(jnm1ksa-jnp1ksa);
    return(fphi);
}

/***** computeAt subroutine *****/
/* This routine computes Atheta */
/*****

float computeAt(void)
{
    float At;

```

```

At=C2*(-kp*kp*k0*a*cost*cost*(jnm1ksa+jnp1ksa)+
    pow((float)(2*(m+1)*PI/d),2.)*n/2.*sint*jnksa );
return(At);
}

/***** computeAp subroutine *****/
/* This routine computes Aphi */
/*****/

float computeAp(void)
{
    float Aphi;

    Aphi=C1*(jnm1ksa-jnp1ksa);
    return(Aphi);
}

/***** findmax subroutine *****/
/* This routine find maximum of absolute of an array */
/*****/

float findmax(float *f)
{
    float maxf=0.;
    int i;

    for(i=0;i<step;i++)
        if(fabs(f[i])>maxf) maxf=fabs(f[i]);
    return(maxf);
}

/*****/

float max(float a,float b)
{
    if(a>b) return(a);
    else return(b);
}

/***** JnJm subroutine *****/
/* This routine computes production of Jn(kpa)Jm(k0asin(theta)) */
/* It uses bess to compute Bessel's functions */
/*****/

float JnJm(int v,int w,float x)
{

```

```

    return( bess(v,x*kp) * bess(w,x*ks) );
}

/***** integration subroutine *****/
/* This subroutine uses Gauss integration method to integrate from f from */
/* a to b and returns the value of integral. */
/*****

float integration(float f[])
{
    int j;                /* loop counter */
    float s;              /* integral result */

    s=0.;

    for(j=0;j<5;j++)
        s += wintegral[j]*(f[j]+f[9-j]);
    return(s *= 0.5*a);    /* scale and return the answer */
}

/***** bess subroutine *****/
/* This subroutine computes Bessel's function of first order. */
/*****

float bess(int v,float x)
{
    float bessj0(float x);    /* computes J0(x) */
    float bessj1(float x);    /* computes J1(x) */
    float bessjn(int v,float x); /* computes Jn(x) with recurrence relation */

    switch(v)
    {
        case 0: return(bessj0(x));
        case 1: return(bessj1(x));
        case -1: return(-bessj1(x));
        default: return(bessjn(v,x));
    }
}

/***** bessj0 subroutine *****/
/* This subroutine computes J0(x) */
/*****

float bessj0(float x)
{
    float ax,z;

```

```

double xx,y,ans1,ans2,ans;

if((ax=fabs(x)) < 8.)
{
    y=x*x;
    ans1=57568490574.+y*(-13362590354.0+y*(651619640.7+
        y*(-11214424.18+y*(77392.33017+y*(-184.9052456)))));
    ans2=57568490411.0+y*(1029532985.0+y*(9494680.718+
        y*(59272.64853+y*(267.8532712+y*1.0))));
    ans=ans1/ans2;
}

else
{
    z=8.0/ax;
    y=z*z;
    xx=ax-0.785398164;
    ans1=1.0+y*(-0.1098628627e-2+y*(0.2734510407e-4
        +y*(-0.2073370639e-5+y*0.2093887211e-6)));
    ans2=-0.1562499995e-1+y*(0.1430488765e-3
        +y*(-0.6911147651e-5+y*(0.7621095161e-6
        -y*0.934935152e-7)));
    ans=sqrt(0.636619772/ax)*(cos(xx)*ans1-z*sin(xx)*ans2);
}
return ans;
}

/***** bessj1 subroutine *****/
/* This subroutine computes J1(x) */
/*****

float bessj1(float x)
{
    float ax,z;
    double xx,y,ans1,ans2,ans;

    if((ax=fabs(x)) < 8.)
    {
        y=x*x;
        ans1=x*(72362614232.0+y*(-7895059235.0+y*(242396853.1
            +y*(-2972611.439+y*(15704.48260+y*(-30.16036606)))));
        ans2=144725228442.0+y*(2300535178.0+y*(18583304.74+
            y*(99447.43394+y*(376.9991397+y*1.0))));
        ans=ans1/ans2;
    }

```

```

else
{
    z=8.0/ax;
    y=z*z;
    xx=ax-2.356194491;
    ans1=1.0+y*(0.183105e-2+y*(-0.3516396496e-4
        +y*(0.2457520174e-5+y*(-0.240337019e-6))));
    ans2=0.04687499995+y*(-0.2002690873e-3
        +y*(0.8449199096e-5+y*(-0.88228987e-6
            -y*0.105787412e-7)));
    ans=sqrt(0.636619772/ax)*(cos(xx)*ans1-z*sin(xx)*ans2);
    if(x<0.0) ans= -ans;
}
return ans;
}

/***** bessjn subroutine *****/
/* This subroutine computes Jn(x). */
/*****

float bessjn(int v,float x)
{
    int j,jsum,m;
    float ax,bj,bjm,bjp,sum,tox,ans;
    float bessj0(float x);
    float bessj1(float x);

    ax=fabs(x);
    if(ax == 0.0) return 0.0;
    else
        if( ax > (float)v )
        {
            tox=2.0/ax;
            bjm=bessj0(ax);
            bj=bessj1(ax);
            for(j=1;j<v;j++)
            {
                bjp=j*tox*bj-bjm;
                bjm=bj;
                bj=bjp;
            }
            ans=bj;
        }
        else
        {
            tox=2.0/ax;

```

```

m=2*((v+(int)sqrt(ACC+v))/2);
jsum=0;
bjp=ans=sum=0.0;
bj=1.0;
for(j=m;j>0;j--)
{
    bjm=j*tox*bj-bjp;
    bjp=bj;
    bj=bjm;
    if(fabs(bj) > BIGNO)
    {
        bj *= BIGNI;
        bjp *= BIGNI;
        ans *= BIGNI;
        sum *= BIGNI;
    }
    if(jsum) sum += bj;
    jsum =!jsum;
    if(j==v) ans=bjp;
}
sum=2.0*sum-bj;
ans /= sum;
}
return x<0.0 && v%2 == 1 ? -ans : ans;
}

/***** end of code *****/

```


References

- [1] G.A. Deschamps, "Microstrip microwave antennas," *presented at the 3rd USAF Symposium on Antennas*, 1953.
- [2] J. Q. Howell, "Microstrip antennas," *IEEE Trans. AP-S Int. Symp. Digest*, pp. 177-180, 1972.
- [3] R. E. Munson, "Conformal microstrip antennas and microstrip phased arrays," *IEEE Trans. Antennas Propag.*, vol. AP-22, pp. 74-78, 1974.
- [4] I. J. Bahl and P. Bhartia, *Microstrip Antennas*, Dedham, Massachusetts: Artech House, 1982.
- [5] J. Hung, "The finite ground plane effect on the microstrip antenna radiation patterns," *IEEE Trans. Antennas Propag.*, vol. AP-31, No. 4, pp. 946-952, 1983.
- [6] S. Barroso De Assis Fonseca and A. J. Giarola, "Microstrip disk antenna, part II: the problem of surface wave radiation by dielectric truncation," *IEEE Trans. Antennas Propag.*, vol. AP-32, No. 6, pp. 568-573, 1984.
- [7] A. A. Kishk and L. Shafai, "The effect of various parameters of circular microstrip antennas on their radiation efficiency and the mode excitation," *IEEE Trans. Antennas Propag.*, vol. AP-34, No. 8, pp. 969-976, 1986.
- [8] A. K. Bhattacharyya, "Effects of finite ground plane on the radiation characteristics of a circular patch antenna," *IEEE Trans. Antennas Propag.*, vol. AP-38, No. 2, pp. 152-159, 1990.
- [9] A. K. Bhattacharyya, "Effects of ground plane and dielectric truncation on the efficiency of a printed structure," *IEEE Trans. Antennas Propag.*, vol. AP-39, No. 3, pp. 303-308, 1991.
- [10] A. K. Bhattacharyya, "Effects of ground plane truncation on the impedance of a patch antenna," *IEE Proceedings-H*, vol. 138, No. 6, pp. 560-564, 1991.
- [11] P. Vaudon, A. Reinex and B. Jecko, "Asymptotic method in prediction of E plane radiation

- pattern of rectangular microstrip patch antennas on finite ground," *Electronics letters*, vol. 26, No. 13, pp. 956-957, 1990.
- [12] P. Vaudon, T. Aubreton, P. Dufrane and B. Jecko, "Influence of the ground plane structure on the radiation pattern of microstrip antennas," *Annals of Telecommunication*, vol. 48, No. 5-6, pp. 319-329, 1993.
 - [13] A. A. Kishk, "Different integral equations for numerical solution of problems involving conducting or dielectric objects and their combination," *Ph.D. Dissertation*, University of Manitoba, 1986.
 - [14] R. E. Collin, *Antennas and radiowave propagation*, McGraw-Hill, 1987.
 - [15] K. Antoskiewicz and L. Shafai, "Impedance characteristics of circular microstrip patches," *IEEE Trans. Antennas Propag.*, vol. AP-38, No. 6, pp. 942-946, 1990.
 - [16] I. J. Bahl and P. Bhartia, "Comparison of radiation characteristics of microstrip patch antennas," *IEEE Trans. AP-S Int. Symp. Digest*, vol. 1, pp. 15-19, 1981.
 - [17] W. L. Stutzman, *Polarization in electromagnetic systems*, Boston, London: Artech House, 1993.
 - [18] S. Noghianian, "Effects of finite ground plane parameters on microstrip antenna performance," *Technical Report*, University of Manitoba, 1995
 - [19] R. K. Mongia and P. Bhartia, "Dielectric resonator antennas-A review and general design relation for resonant frequency and bandwidth," *International Journal of Microwave and Millimetre-Wave Computer-Aided Engineering*, vol. 4., No. 3, pp. 230-247, 1994.
 - [20] A. A. Kishk, G. Zhou, and A. W. Gilsson, "Analysis of dielectric resonator antennas with emphasis on hemispherical structures," *IEEE Antennas and Propag.*, vol. 36, No. 2, pp. 20-31, 1994.

- [21] S. A. Long, M. W. McAllister, and L. C. Shen, "The resonant cylindrical dielectric cavity antenna," *IEEE Trans. on Ant. and Propag.*, vol. AP-31, No. 3, pp. 406-412, 1983.
- [22] A. A. Kishk, A. A. Hesham, and B. C. Ahn, "Radiation characteristics of cylindrical dielectric resonator antennas with new applications," *IEEE Antenna and Propag. Society Newsletter*, pp. 7-15, Feb. 1989.